Corso di dottorato di ricerca in:

"scienze biomediche e biotecnologiche"

Ciclo (es. 33°)

Titolo della tesi

"Biophysics of protein conformational dynamics by NMR spectroscopy"

Dottorando
Yamanappa Hunashal

Supervisore
Prof. Gennaro Esposito

Anno 2020-2021

INDEX

ABSTRACT

The effect of extrinsic paramagnetic probes on NMR relaxation rates for surface mapping of proteins and other biopolymers is a widely investigated and powerful NMR technique. Here we describe a new application of those probes. It relies on the setting of the relaxation delay to generate magnetization equilibrium and off-equilibrium conditions, in order to tailor the extent of steady state signal recovery with and without the water-soluble nitroxide Tempol. With this approach it is possible to identify signals whose relaxation is affected by exchange processes and, from the relative assignments, to map the protein residues involved in association or conformational interconversion processes on a micro-to-millisecond time scale. This finding is confirmed by the comparison with the results obtained from relaxation dispersion measurements. This simple and convenient method allows preliminary inspection to highlight regions where structural or chemical exchange events are operative, in order to focus on quantitative subsequent determinations by transverse relaxation dispersion experiments or analogous NMR relaxation studies, and/or to gain insights into the predictions of calculations. This presented approach can be advantageously applied to the characterization of the interface in protein-protein and protein-nanoparticles interactions and to study oligomerization of proteins.

ABBREVIATIONS

2D	Two-dimensional
3D	Three-dimensional
Å	Ångström = 0.1 nm
β2m	β2-microglobulin (beta2-microglobulin)
$\Delta\delta$	Chemical shift difference
τ_c	Rotational correlation time
A_N	Normalized attenuation
A_N [*eq*]	Normalized attenuation calculated in equilibrium condition
A_N [*off-eq*]	Normalized attenuation calculated in off-equilibrium condition
AuNPs	Gold nanoparticles
CHARMM	(Chemistry at HARward Macromolecular Mechanics) a widely used force field for Molecular Dynamics simulations
CPMG	Carr-Purcell-Meiboom-Gill
CSP	Chemical Shift Perturbation
D76N β2m	β2m mutant with Asp in position 76 is replaced by Asn
DOSY	Diffusion Ordered SpectroscopY
DRA	Dialysis-Related amyloidosis
DSTEBPP	Double STimulated Echo BiPolar Pulse
ESR	Electron Spin Resonance
GBSA	Generalized Born Surface Area
HEWL	Henn Egg White Lysozyme
HSQC	Heteronuclear Single Quantum Correlation
NMR	Nuclear Magnetic Resonance
NOE	Nuclear Overhauser Effect
OBC	Onufriev-Bashford-Case
PDB	Protein Data Bank
ppm	parts per million $(1/10^6)$
R_1	Longitudinal relaxation rate
R_2	Transverse relaxation rate
$R_{1\rho}$	Rotating-frame relaxation rate

RI	Relative intensity
RI_{av}	Average relative intensity
R_{ex}	Exchange relaxation rate
TOCSY	TOtal Correlated SpectroscopY
WATERGATE	Water suppression by gradient tailored excitation
WT	Wild-type

Amino acids abbreviations

Amino acid	**Three letter code**	**one letter code**
Alanine	Ala	A
Arginine	Arg	R
Asparagine	Asn	N
Aspartic acid	Asp	D
Cysteine	Cys	C
Glutamine	Gln	Q
Glutamic acid	Glu	E
glycine	Gly	G
Histidine	His	H
Isoleucine	Ile	I
Leucine	Leu	L
Lysine	Lys	K
Methionine	Met	M
Phenylalanine	Phe	F
Proline	Pro	P
Serine	Ser	S
Threonine	Thr	T
Tryptophan	Trp	W
Tyrosine	Tyr	Y
Valine	Val	V

1. INTRODUCTION

1.1 Protein folding / misfolding

Protein folding is the complex mechanism that is responsible for the formation of the native three-dimensional structure of proteins, leading to the biologically active conformation. In living systems, protein folding is a physical process by which a polypeptide chain arranges from the transient structure adopted while biosynthesis occurs in to a functional and characteristic three-dimensional structure. Protein folding is a spontaneous process which is mainly guided by van der Waals forces[1], intramolecular hydrogen bond formation[2] and hydrophobic interactions[3].

The model of the folding funnel reported in Figure 1.1 has been developed from both experimental observations and theoretical calculations based on simplified mechanical models. To describe kinetic and thermodynamic features of protein folding, the folding funnel model is illustrated in terms of an energy landscape. The broad top area of the folding funnel suggests that a considerable number of conformations are present in the denatured state, opposite to the native state of the protein represented by the narrow bottom of the funnel.

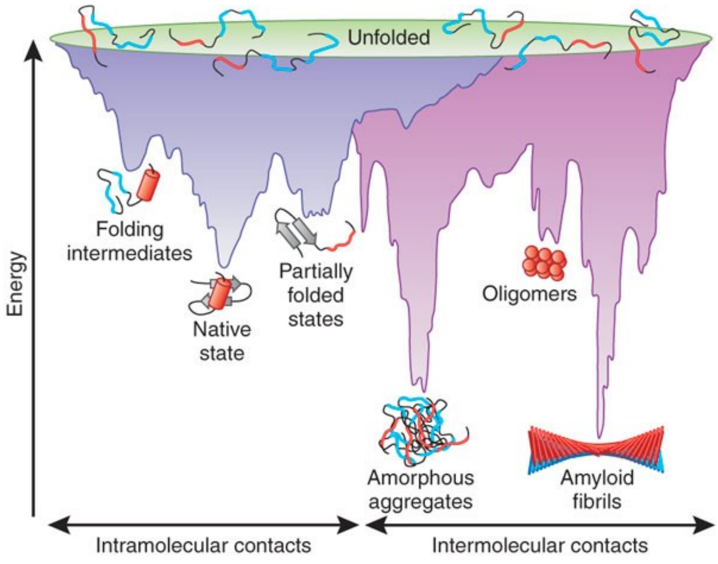

Figure 1.1: Energy landscape representation of protein folding and aggregation[4]. The folding funnel is highlighted in two different colors, i.e. purple to highlight the intramolecular contacts that are required to achieve the native state, and pink for intermolecular contacts that produce amyloid fibrils or amorphous aggregates. Both intramolecular and intermolecular parts of the energy surface overlap.

The space between the bottom and the top of the folding funnel illustrates the enthalpy, solvent entropy and polypeptide chain enthalpy energy contribution to each polypeptide chain conformation.

As the protein starts to fold towards lower energy state, more ordered intermediates start to populate lower parts of the folding funnel, which are less hydrated than the flexible unfolded proteins. Depending on the minimum energy parts of the funnel, the protein is conveyed to the formation of local conformational structure. The depth and number of local kinetic traps on the folding funnel landscape illustrates the degree of frustration in the polypeptide according to statistical mechanics[5].

1.2 Amyloidosis

A protein is considered to be misfolded if it does not acquire its native local state. As such, misfolding typically involves only partially the protein structure and may even imply very limited regions of the protein. Misfolding occurs because the native folding state is locally destabilized by external factors or mutations in the protein sequence. Once formed, the misfolded protein may engage into a cross-β structure that entails ordered supramolecular arrangement of β-sheets growing into elongated filaments named fibrils. These fibrillar β-sheet assemblies are insoluble, very stable and resistant to proteolysis. The fibrillar assembly structure is stabilized by the formation of hydrogen bonds between β-strands. These strands are perpendicular to the fibril axis whereas the inter strand hydrogen bonds are parallel to the fibril axis. The misfolding of proteins can favour further misfolding of different proteins into fibrillar oligomers or aggregates. Whatever the mechanism of monomer recruitment, an increased level of protein fibrillar oligomers triggers further elongation leading to insoluble filaments that precipitate and accumulate, most often extracellularly, to form amyloid deposits. Amyloid deposition can become pathologic and typically impairs organ functions when very large amounts accumulate. Most often it is the very presence of amyloid aggregates that causes cell death and degenerative disorders due to dissociation from the amyloid deposits of soluble fibrils that are believed to affect the correct intercellular trafficking. Amyloid aggregates cause many devastating neurodegenerative diseases such as Parkinson’s disease, Huntington’s disease, Alzheimer’s disease, type II diabetes, bovine spongiform encephalopathy, familial amyloid cardiomyopathy and Creutzfeldt-Jakob disease. The corresponding amyloidosis concern a single organ or type of tissue. There are also less specific amyloidosis that affect the whole organism and are therefore defined systemic amyloidosis as described below.

AL Amyloidosis: AL amyloidosis or light-chain amyloidosis is resulting from a bone marrow disorder. The bone marrow, present in the middle of the bones, produces cell, including plasma cells, for supply to the blood tissue. These plasma cells which produce antibodies called immunoglobulins for combating external antigens. In antibody light-chain amyloidosis, aberrant plasma cells express an excess of mutant antibody light chain which builds up in the bloodstream instead of being cleared and eventually deposit into amyloid in organs and tissues. The main affected organs and districts are kidneys, heart, nerves and gastrointestinal tract.

AA Amyloidosis: AA amyloidosis happens as a response to any other illness, which includes a chronic infection or chronic inflammatory disease. Liver produces a protein known as serum amyloid A protein (SAA) in excessive levels because of a chronic infection or a chronic inflammatory disease. A small part of the SAA protein known as AA protein is excised from SAA protein and forms amyloid deposits in various organs and tissues when inflammation takes place for a long period. A chronic infection increases AA amyloid deposits in all tissues, the main affected organ being kidneys, but also spleen, liver, digestive tract, heart, thyroid can be involved.

Hereditary Amyloidosis: Hereditary amyloidosis is one form of systemic amyloidosis illness which is due to inheriting a gene mutation. An amyloidogenic protein is generated after genetic mutation that destabilize the native folding. The misfolded protein can cluster into fibrillar filaments and deposit in the body’s organs and tissues. There are two fundamental kinds of hereditary amyloidosis diseases: ATTR and Non-TTR. ATTR means A for amyloid and TTR is transthyretin protein. So ATTR represents different types of genetic mutations in TTR gene that can be inherited. Transthyretin that naturally occurs as a tetramer becomes unstable because of the mutation and undergoes amyloidogenic misfold. TTR is mainly produced in the liver. Depending on the type of mutation, amyloid fibrils can damage organs and nerves. The Non-TTR amyloidosis has different inherited gene mutations that can affect health and cause major symptoms. Non-TTR amyloidosis involves proteins such as Fibrinogen Aa, Cystatin C, Apo lipoprotein AII, Apo lipoprotein AI, Lysozyme and Gelsolin.

1.2.1 Mechanisms of amyloid assembly

The mechanism of amyloid fiber formations can be divided in two phases, (i) Nucleation Phase and (ii) Elongation Phase. In many cases the starting of the nucleation phase implies a conformational exchange between an amyloidogenic intermediate state and the non-amyloidogenic native state. The interconversion between these states form structurally flexible oligomers which include conformationally altered monomers. Oligomerization is favored because partially or totally misfolded intermediates have larger hydrophobic surface than native state. Higher order oligomers that become structurally rigid can result from an associative equilibrium between structurally flexible oligomers or between structurally flexible oligomer and native monomeric state protein. The higher order oligomers form toxic protofibrils with supramolecular cross-β structure and these protofibrils grow into elongated fibers due to hydrogen bonding and hydrophobic interaction. Another way of elongation is the recruitment of a soluble monomeric unit, still in native state conformation, to the preassembled nucleus. This recruitment mechanism entails the conformational conversion of the new recruited monomer. Thioflavin T (ThT) fluorescence is the commonly used method to follow the progress of amyloid formation. The dye in fact attaches to cross- β aggregates[6].

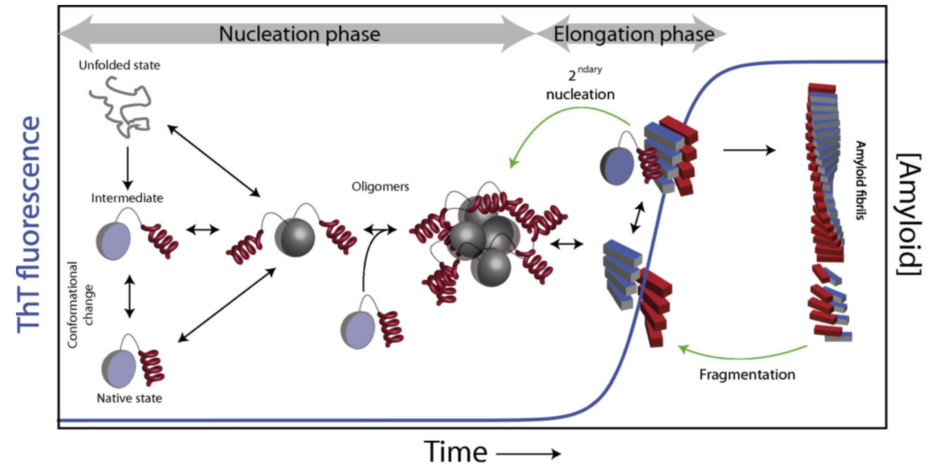

Figure 1.2: The schematic representation of possible routes of amyloid formation[7].

1.2.2 β2-Microglobulin

β2microglobulin (β2m) is the light chain of class I major histocompatibility complex (MHC-I) and one of the most studies amyloid protein. Human β2m, a 99-residues single polypeptide chain whose complete amino acid chain was first reported in 1973[8], has molecular weight 11.815 kDa. β2m is a protein normally present on the surface of every nucleated cell in the human body[9] is associated to dialysis related amyloidosis (DRA) which affects the patients who undergo long term hemodialysis when renal failure impairs the protein clearance[10].

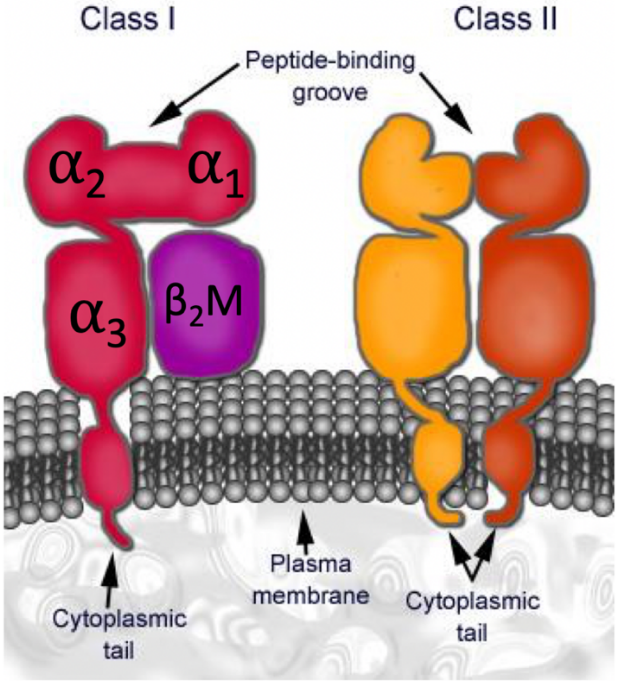

Figure 1.3: Schematic representation of MHC. This figure is from Medscape page (https://emedicine.medscape.com/article/2086864-overview)

β2m lies beside the α_3 domain and below α_1 domain (in turn next to the α_2 domain) of MHC-I heavy chain, on the cell surface. Because of continuous regeneration of membrane proteins, β2m dissociates from the cell surface. β2m is then transported to the kidneys through which it is normally cleared. Plasma concentrations of β2m vary from 1-2 mg/L in healthy individuals[11]. If the kidneys' function is defective, β2m can not be removed from the plasma and a dialysis apparatus becomes necessary. The latter is less efficient to filter the protein from plasma. Because of reduced filtration efficiency, the plasma concentration rises to approximately 50 -

70 mg per liter[11]. The circulating hematic concentration increases and the protein forms amyloid fibers that eventually deposit onto bones and joints.

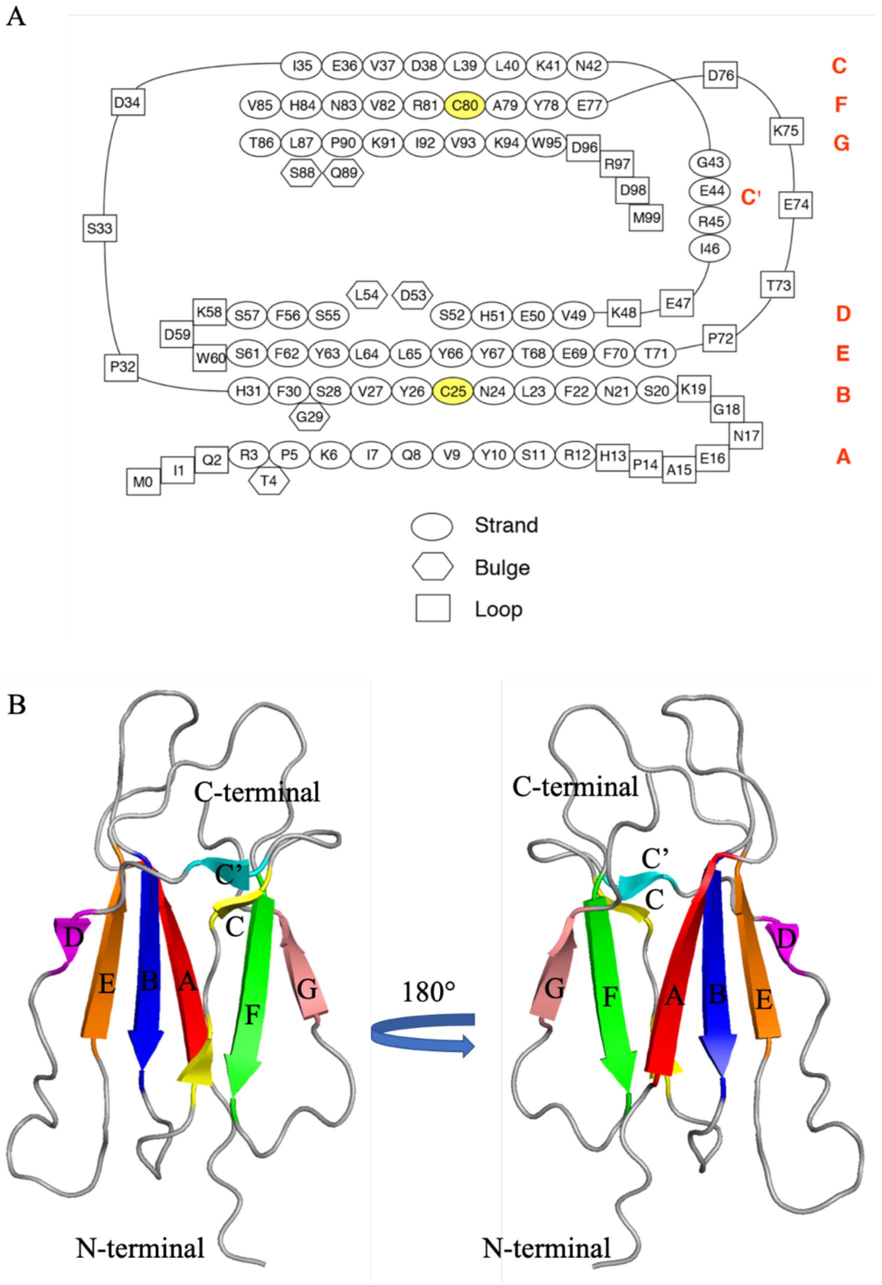

Figure 1.4: In the upper part, schematic representation of amino acid sequence and secondary structure as determined by solution NMR spectroscopy of human β2m (A). The yellow colored residues are Cys25 and Cys80 forms the disulfide bond. Each β-strand name reported on the right side with red capital letters. In the lower part, cartoon representation of the solution NMR structure of human β2m (B). For better view each strand are colored differently strand-A in red, strand-B in blue, strand-C in yellow, strand-C' in cyan, strand-D in magenta, strand-E in orange, strand-F in green, strand-G in salmon, and loops are in grey.

β2m secondary structure has seven anti-parallel β- strands that form two β- sheets. The β-strand named as stand A, B, C, D, E, F and G with an additional inter-sheet short strand C’. In the tertiary structure of β2m, one β- sheet composed of strands A, B, D, and E whereas the second one includes stand C, F, and G. The overall structure is stabilized by a single disulfide bond linking the two sheets between Cys25 and Cys80, which belong to strand B and strand F respectively (Figure 1.4)[12,13]

The crystal structure of the complex, i.e. β2m bound to MHC -I, was solved in 1991[14]. The first crystal structure of the isolated monomeric human β2m and the solution structure of the monomeric human β2m were solved in the same year 2002 by different groups[13,15]. From the structural comparison of the solution and complex crystal (Figure 1.5) there are structural changes observed at strands A, D, E and loop DE considered keys for amyloid transition[13]. The latter was proposed to start at the N-terminal end, with the rupture of the pairing of strand A to B which influences polymerization at strand D through intermolecular pairing leading to formation of fibrils[13]. In 2008, the study on one of the β2m variant, W60G β2m, led to the conclusion that the continuity of strand D is not the reason for the β2m to aggregate into amyloid fibrils[16] as previously proposed[15].

Other researchers had earlier pointed out that at neutral pH the native β2m monomer does not form amyloid fibrils that instead form under acidic condition[17]. The β2m monomer has the peptidyl-prolyl bond between His31-Pro32 that adopts *cis* conformation in the BC loop. The increase in the concentration of nonnative monomeric β2m, in which the histidyl-prolyl bond between His31-Pro32 has *trans* geometry, was proposed to be the main reason for the amyloid formation[18,19], and this statement has been long misleading interpretations and theories, in spite of contrary evidence[20]. Only recently, however, even one of the main supporters of the Pro32-dependent mechanism proposed that the species with His31-Pro32 *trans* configuration may only be a bystander of the transition to the fibrillogenic species[21].

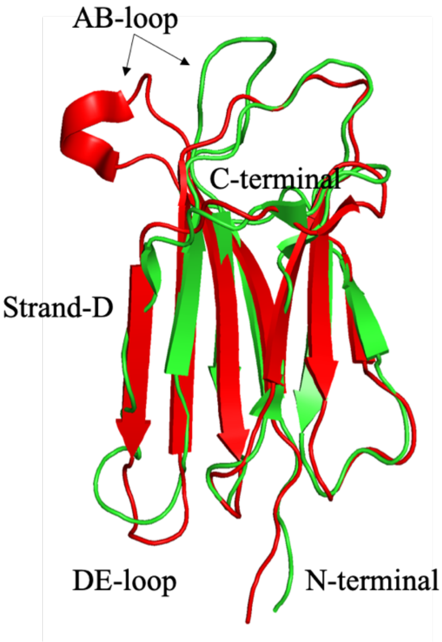

Figure 1.5: Cartoon overlay of solution structure of β2m (PDB entry 1JNJ) in green, and isolated protein crystal structure (PDB entry 1LDS) in red.

There is lot of NMR work that has been done on β2m alone and in the presence of ligands. Conformational dynamics of β2m is monitored after addition of Cu^{2+} ions and titration show that three histidines, His13, His31 and His51, are involved in binding[13,22]. Heteronuclear ^{15}N $\{^1H\}$ NOE showed that in oxidized state β2m has reduced flexibility compared to the results from the reduced form in acid-denatured state at pH 2.5[23]. Conformational properties of β2m were analyzed by using high pressure NMR as well as salt dependent chemical shift perturbation[24]. The high-pressure NMR data showed the increase in the signal intensity at strands C, D and E under high pressure condition. At 5 MPa pressure (~50atm) the transverse relaxation rate (R_2) are too large to be determined in the region 60-70, but in the higher pressure condition the same region showed selective decrease in the relaxation rate. It was concluded that the large R_2 values were determined by the occurrence of a slow ($\tau \approx$ ms) conformational fluctuations in the fragment 60-70. At higher pressure the difference in the population of the structures is increased leading to increase in the signal intensity.

1.2.3 D76N β2-Microglobulin

D76N β2m is a naturally occurring mutant of β2m in which aspartate is replaced by an asparagine at the position 76. It was found in a French family whose members had dysfunction of bowel, postural dizziness, sicca syndrome and chronic diarrhea[24]. Medical tests revealed that the circulating concentrations of β_2-microglobulin was normal in contrast to dialysis related amyloidosis patients. D76N β2m aggregates *in vitro* at physiological conditions (at 37°C, physiological pH and ionic strength) even without seeding and at low concentrations, in contrast with β2m that remains monomeric for several months in the same conditions[18].

The reduced stability and the increased amyloidogenic propensity of D76N β2m can not be explained on the basis of the crystal structure. Because of mutation the NH group of the Asn76 shows a hydrogen bond with Tyr78 that, in turn, establishes a H-bond with Thr73 (Figure 1.6). Due to loss of negative charge of Asp76, the theoretical isoelectric point shifts from 6.05 to 6.40[25].

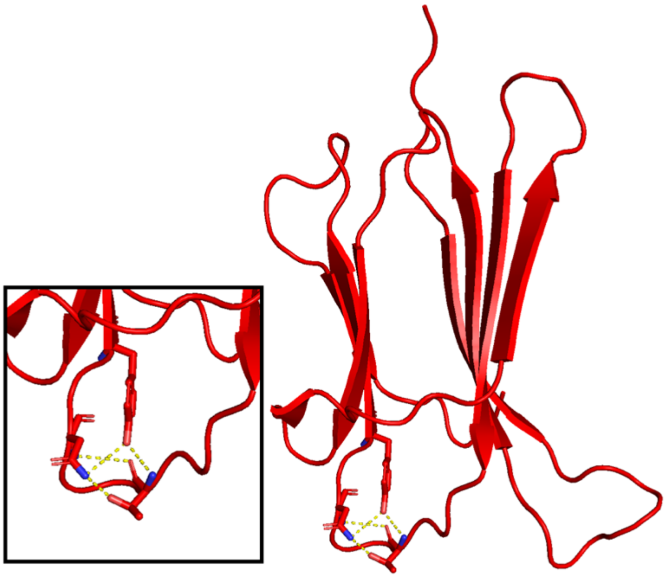

Figure 1.6: Crystal structure of the D76N β2m (PDB ID: 4fxl). Hydrogen bonding between Asn76, Tyr78, and Thr73 are shown by the yellow dashes. Contrary to previous figure representation, the protein is depicted upside down, i.e. with N-terminus upwards

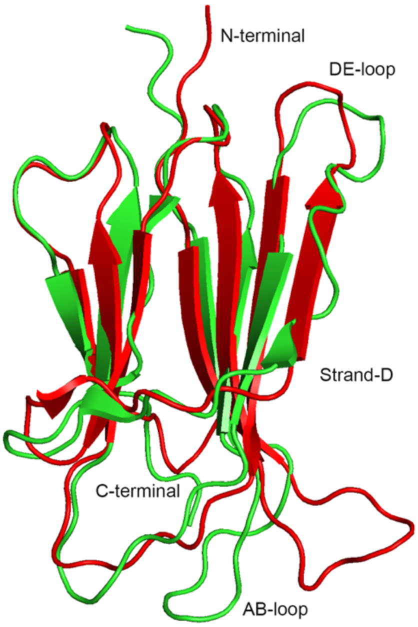

Figure 1.7: Cartoon overlay of Crystal structure of the D76N β2m (PDB ID: 4fxl) in red and solution structure of β2m (PDB entry 1JNJ) in green. The same orientation as Figure 1.6 is shown.

There is no significant difference in the solution NMR structure of the wild-type β2m and D76N β2m protein, despite the mutant is less stable when compared with wild-type β2m. The denaturation free energy values for the wild-type and D76N β2m are in fact 5.7±0.4 kcal/mol and 3.00±0.15 kcal/mol, respectively[26]. Molecular dynamic simulations show some interesting results on D76N β2m intermediate I_T, i.e. the solvent exposure of hydrophobic residues is increased and the solvation free energy is higher than wild-type β2m I_T intermediate because of the increased tendency to form β-sheet in the disordered D-strand[27]. Besides the recent report about the possible bystander role of I_T[21], simulations devoid of experimental verification should always be considered with caution. This is also the case with the more recent proposal by Loureiro and coworker[28]. Those authors published molecular dynamics simulations on folding of D76N β2m and reached the conclusion that there are two intermediate states, named I_1 and I_2, with aggregation tendency. In the intermediate state I_1, the C – terminal is unstructured, but in I_2 both N- and C- terminals are unstructured which makes I_2 more aggregation prone compared to the other intermediate. This work builds on previous results by Camilloni et al[29] but does not provide convincing proofs. Since the detachment of the N-terminal stretch is the salient difference between I_2 and I_1, one would expect a discussion on the correlation between N-terminal stretch detachment and increased aggregation propensity. Instead the authors only show histograms of the dimerization hot-spots that invariably map region DE as most relevant dimerization spot, with Trp60 being the most sampled contact whichever the considered intermediate dimer, i.e. either from I_2 or I_1. However, an experimental verification exists and is contrary to the two-tail theory proposed by Louriero et al.. In fact, the heteronuclear NOE measurements reported by Mangione et al.[26] clearly show that there is no differential backbone mobility between wild-type and D76N β2m at both C-terminal and N-terminal regions, even upon increasing temperature from 25ºC to 37ºC, the differential backbone mobility being elsewhere. If the larger aggregation propensity of D76N β2m were dependent on the occurrence of a partially unfolded conformer with an additional detachment at the N-terminus, a difference in backbone mobility should have been observed at the N-terminal region on comparing the wild-type and the mutant. Hence the two-tail theory remains speculative.

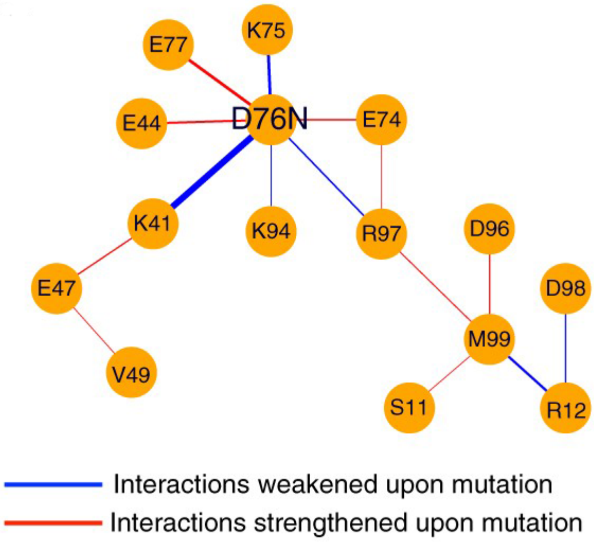

Figure 1.8: Graphical representation of interactions between amino acids that are strengthened (red) or weakened (blue) upon mutation, according to Le Marchand et al.[30].

Later, in 2018, Le Marchand and co-workers[30] stated that there is an intermediate state (defined excited state) in D76N β2m which qualitatively matches with I_2. Due to loss of β- structure at the both N – and C – terminus this excited state forms a highly dynamic conformation which exposes more aggregation prone regions. The residues in the EF loop and at the end of strand A show more conformational dynamics in the mutant compared to wild type β2m[30]. In addition to these differences from replica-averaged metadynamics, the analysis of the interaction differences provided the grounds of the thermodynamic destabilization of D76N β2m with respect to the wild-type protein in terms of weakened electrostatic interactions at residue 76 as depicted in Figure 1.8. According to Le Marchand and colleagues, the most relevant effect concerns the weakening of the interaction with R97, although the most relevant difference derives from the loss of the salt bridge between D76 and K41. While the interaction difference effects are relevant, as pointed out earlier[26], again the molecular framework that traces the easier transition of the mutant species from folded to partially unfolded and more aggregation-prone conformation is in contrast with the experimental evidence obtained from heteronuclear NOE data[26]. In particular those data had shown that the backbone mobility increment observed with temperature for both wild-type and D76N β2m does not concern the N-terminal region in either species. Rather the weaker connection between residue 76 and K41 in the mutant protein spreads all over the underlying region with mobility increases that occur close to the ends of strands A, B, E and F and C-terminal. In fact, only in D76N β2m C-terminal increases its mobility with temperature. These experimental results suggest that contrary to the mechanism described by MD simulations, the N-terminal intervention in the conformational transition towards more aggregation prone conformers is not a prerogative of D76N β2m. Instead the new event that characterizes the partial unfolding of D76N β2m with respect to the wild-type sequence is the C-terminal mobility change. Both species undergo a transition that involves the detachment of strand A from the β -sandwich motif (that, of course, entails the displacement of the whole N-terminal fragment from the native conformation as earlier pointed out[31]), but the very energy key of the transition that differentiates the mutant is the C-terminal involvement (residues 94 and 97) that trigger the exposure of W95, a residue that is essential for ensuring the folding of the entire molecule[16].

1.3 β2-Microglobulin and variant D76N interaction with Nanoparticle

A systematic investigation was carried out over the last years on the interaction of amyloidogenic protein models and citrate-coated gold nanoparticles (AuNPs)[32–35]. The interaction between β2m and citrate-coated AuNPs, with diameters of 5 and 7.5 nm, was modeled at multiple levels and the results were in excellent agreement with the experimental NMR determinations to explain in terms of electrostatic interaction the origin of the observed protein signal perturbations[32–34]. Citrate capped AuNP showed interaction with β2m residues of the N-terminal, strand B, BC loop, DE loop in good agreement with simulation results[32]. The studies were conducted on wild-type β2m and the naturally occurring amyloidogenic mutant D76N β2m. Contrary to the expectations based on previously reported results for β2m at acidic pH[36], the protein solutions with AuNPs were stable for several months and no evidence of increased aggregation or partial unfolding was observed. A concentration-dependent attenuation of the NMR signals was observed for β2m that, because of a uneven distribution, was indicative of a preferential interface of fast exchange with AuNPs[32]. The most amyloidogenic variant of β2m, i.e. D76N β2m, was then studied with the same NP system, using NMR, thioflavin T (ThT) fluorescence and transmission electron microscopy (TEM)[34]. Significantly, the presence of citrate-stabilized AuNPs did not enhance the onset of D76N β2m fibrils, as expected from previous observations[36], but rather inhibited fibrillogenesis[34] by interfering with the early aggregation steps of the protein that are crucial for the protofibril nucleus formation.

In addition to citrate coating, other types of stabilizing decorations were tested[35,37] that provided quite general guidelines for the specific coating properties that must be implemented for stabilizing amyloidogenic proteins in NP colloidal suspensions. Among the possible ligands, thiols are the ones that produce the more stable organic monolayer grafted on gold NPs. We studied, in particular the behavior of three different alkanethiolate-coated AuNP (AT-AuNP) systems when incubated with β2m, considered as a paradigmatic amyloidogenic protein, due to its clinical relevance in dialysis-related amyloidosis (DRA)[35,37].

1.4 Hen Egg White Lysozyme

Lysozyme is a ubiquitous enzyme which hydrolyze the β-1,4 glycosidic linkages present between the N-acetylglucosamine and N-acetylmuramic acid on the peptidoglycan cell wall of certain microorganisms[38]. Hen Egg White Lysozyme (HEWL) is one of the best characterized and most studies globular proteins and within the lysozyme classification HEWL belongs to c-type[39].

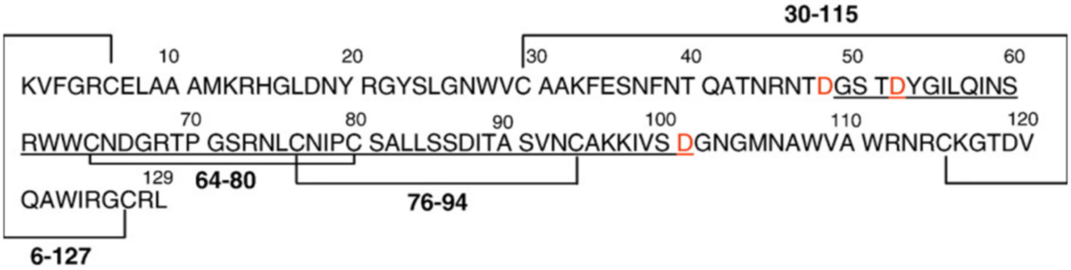

Figure 1.9: Primary structure of HEWL[40] and the connecting lines show disulfide bonds.

HEWL is a single chain small globular protein (14.3 kDa) comprising 129 amino acid residues. There are four disulfide bonds stabilizing the native conformation between Cys 6 and Cys 127, between Cys 30 and Cys 115, between Cys 64 and Cys 80 and between Cys 76 and Cys 94 (Figure 1.9). HEWL has been used as a model system[41–45] after its structure was solved by X-ray diffraction at 2 Å resolution to understand the underlying principles of protein dynamics, function, folding and structure from both theoretical and experimental viewpoint. As a matter of fact, HEWL was the first enzyme whose structure was solved by X-ray diffraction[46].

The crystallographic structure as well as the solution structure solved by NMR of hen egg white lysozyme has two structural domains, α-domain and β-domain. The α-domain (residues 1 to 35 and 85 to 129) consists of a short 3_{10}-helix and four α-helices. This domain has hydrophobic box which means core of hydrophobic side-chains closely packed together. From homonuclear NMR studies, the structure of the HEWL α-domain is well defined in an ensemble of structures since the mean Cα RMSD is 1.2±0.2 Å for the α-domain with respect to the average structures[47]. The β-domain (residues 36 to 84) consists of a 3_{10}-helix, a long loop, and triple-stranded antiparallel β-sheet. In the β-domain of the protein there is no hydrophobic box as in the α-domain. Instead, the β-domain presents a tertiary fold defined by a number of small hydrophobic clusters and hydrogen bonds, accompanied by a long-exposed loop region. The absence of a hydrophobic core in β-domain is confirmed by homonuclear NOEs. In the homonuclear (^{1}H) NOE, a few long range NOEs were identified in the HEWL β-domain, only 68 long range NOEs, i.e. i, i+5 or grater were used for structure determination[47]. The relative orientations of different regions of β-domain are not well defined in the initial NMR structures and the mean Cα RMSD with respect to the average structures is 2.2±0.4 Å for the β-domain[47]. Schwalbe et al. 2001, recalculated the structure by including a relatively small number of dipolar couplings i.e. 209 out of 2011 total experimental restrains, to examine the effect of dipolar couplings on the structure. These additional restrains reduced the Q factors, improved stereochemical quality and reduced the X-ray structure RMSD value[48]. The refinement of HEWL structure after excluding 12 residues from the mobile region (Arg 45, Thr 47, Asp 48, Arg 68, Thr 69, Gly 71, Ser 72, Cys 115, Thr 118, Cys 127, Arg 128, and Leu 129) shows backbone RMSD values of 1.32±0.08Å from the X-ray structure and 0.43±0.10Å from the average NMR structure [48]. In the NMR structure of HEWL, secondary structures regions are identified according to the conditions defined by Kabsch and Sander in 1983[49]. By comparing with X-ray structure with all members of the NMR structure family, three long α-helices are always present, i.e. A helix: Cys 6-His 15; B helix: Leu 25-Ser 36; C helix: Thr 89-Ser 100[47] shown in Figure 1.10.

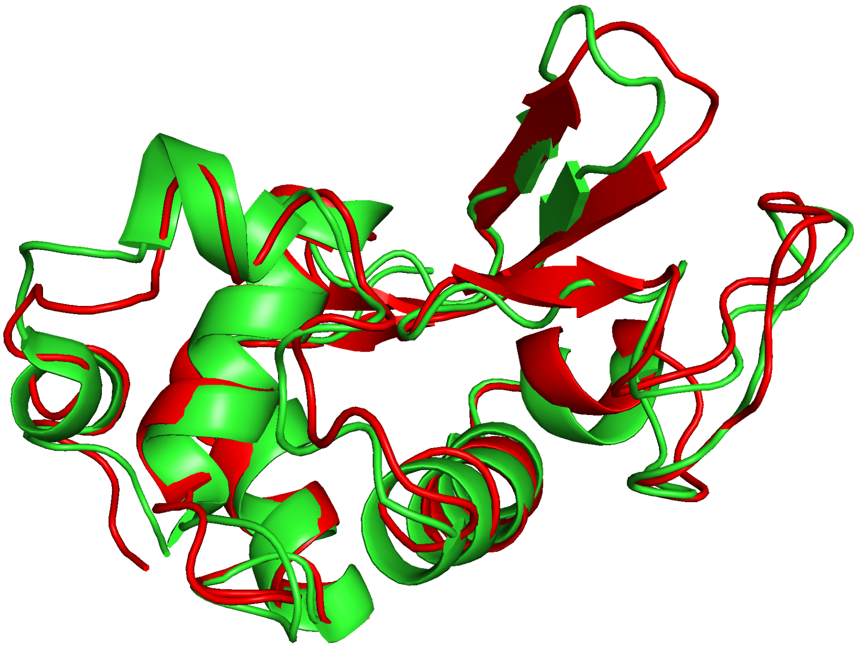

Figure 1.10: Cartoon overlay of solution structure (PDB ID: 1E8L, in green) and crystal structure (PDB ID: 5LYZ, in red) of Hen Egg White Lysozyme.

^{15}N relaxation measurements, at 4 mM protein concentration and pH 3.8 at 35 ^{O}C, show that most of the main chain amide groups undergo small amplitude motions on a fast timescale with order parameter > 0.8. Overall, 19 residues which are located in turn and loop regions, in the first strand of the main β sheet and the C-terminus, showed increased main-chain motion[44]. For example, the residues 68 to 72 in the long loop and residues from 61 to 78, experience substantial fluctuations. The region contains bulky hydrophobic residues (Trp 62, Trp 63, Leu 75, and Ile 78), two proline residues (Pro 70 and Pro 79) and the side chains of several residues that may form different hydrogen bonds (Asn 65, Asn 73, and Asn 77) or salt bridges (Asp 66, Arg 61, Arg 68, and Arg 73). These factors are likely to contribute to the mobility of this loop[44]. Hen Egg White Lysozyme is well known to form amyloid fibrils. Especially under denaturing conditions in detergent, organic solvent, acid pH with high temperature or chemical denaturant[50,51]. The association or aggregation of HEWL has been studied theoretically by molecular dynamic (MD) simulations[52], Brownian Dynamics (BD) simulation[53] showing that HEWL can be absorbed on to the positively charged surface. Monte Carlo simulation[54], magnetic relaxation dispersion[55], NMR diffusion measurements[56], and light and neutron scattering[57,58] were also used. Elna Ermakova did Brownian dynamic simulations on HEWL to study the first stage of dimerization reaction within the framework of encounter complexes by using three initial structures (PDB ID: 1lys, 5lyz, and 1lza)[59]. Complex formation process takes place in two stages: in the first stage, an encounter complex forms when two molecules diffuse towards each other; in the second stage, the encounter complex transforms into a bound complex. Two main groups of complexes are identified after analysis of the simulation results based on the most energetically favorable criterion, namely Type I and Type II[59]. Typical Type I and Type II complexes are shown in Figure 1.11.

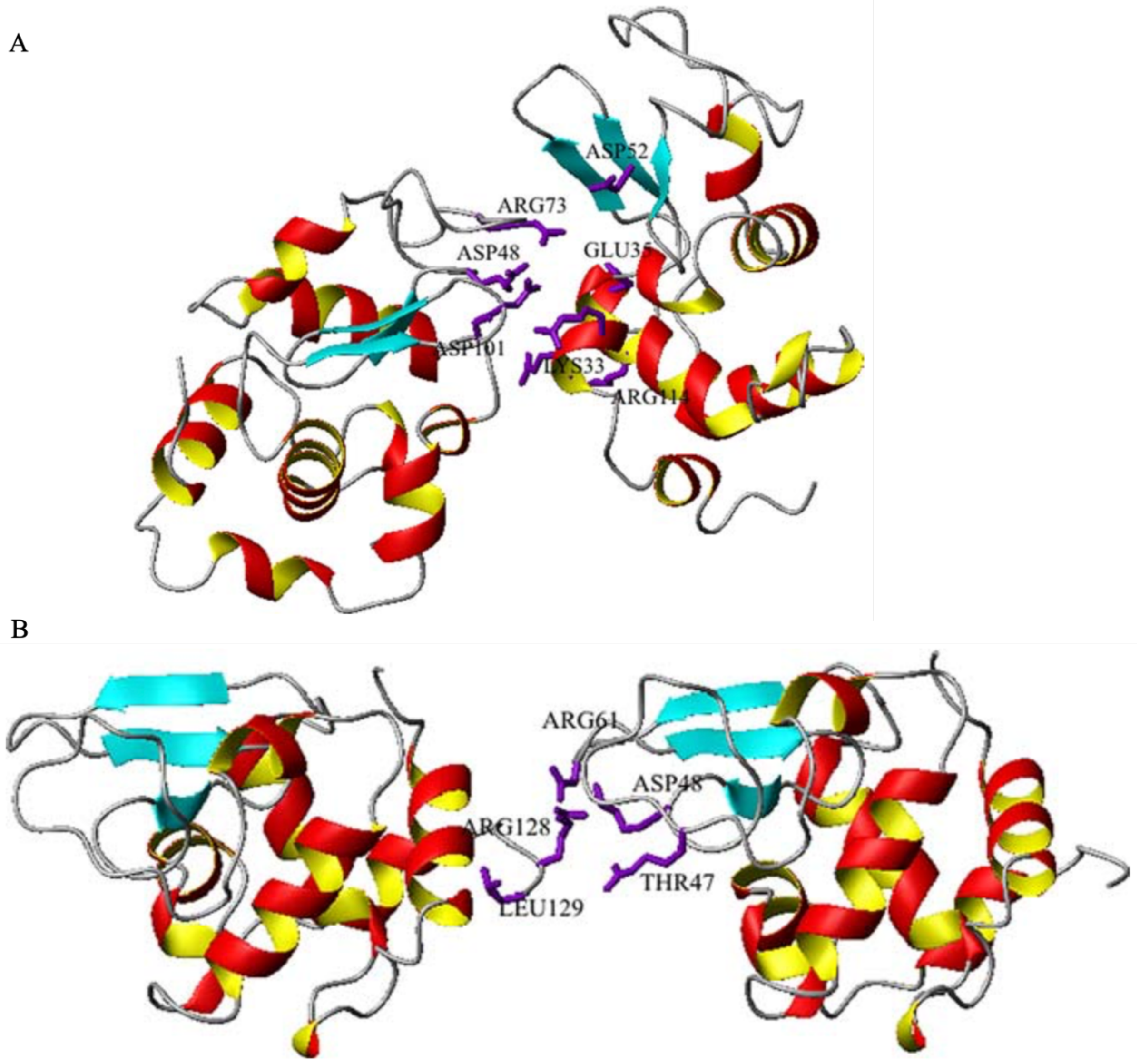

Figure 1.11: The structures of Type I encounter complex (A) and Type II encounter complex (B) of HEWL. The contacting amino-acid residues are drawn explicitly[59].

Type I complexes are formed by interaction between negatively charged carboxylate oxygens of Glu35 and Asp52 and positively charged amino or guanidine groups of Lys 33, Arg 112, and Arg 114 from the first molecule and positively charged guanidine of Arg 61 and Arg 73 and negatively charged oxygens of Asp101 and Asp48 from the second lysozyme molecule. Stabilization of these complexes is additionally supported by salt bridges formed between Arg 73–Glu 35, Asp 52–Arg 61, Asp 52–Arg 73, Arg 112– Asp 48, and Asp 101–Arg 114. The formation of contacts between the residues Lys 33–Asp 48, Arg 112–Glu 35, Glu 35–Arg 73, and Arg 73– Asp 101 provides main contribution to the stability of type I complexes[59].

Type II complexes are formed by head to head or head to tail interaction depending on the orientation of second protein molecule. For three initial structures of encounter complex, an "epitope" was found involving residues. Arg 128, Leu 129, Arg 125, Lys 13, Asp 119. Additional stabilization of the complexes is provided by salt bridges formed between positively charged nitrogens and negatively charged oxygens namely between Arg128-Asp48, Arg128-Asp101[59].

1.5 Protein dynamics by NMR spectroscopy

Among the structural biology techniques currently employed, Nuclear Magnetic Resonance (NMR) spectroscopy and X-ray crystallography, in particular, have revealed the details, at atomic resolution, of a really remarkable amount of processes. Many biological processes take place through short-lived intermediate states that represent small-population states compared to overall population of the state ensemble of a molecular system at equilibrium. Because of the limited population and life time, intermediate states are often difficult to detect by conventional spectroscopic techniques, such as UV, fluorescence, CD, FTIR. These intermediate states may include monomeric species such as conformational intermediates along with functional, folding or unfolding pathways, as well as macromolecular assemblies occurring in aggregation processes. The intermediates typically represent local minima on the free-energy landscape of a macromolecule above the global minimum[60,61]. Structure determination by NMR is traditionally based on the dihedral angle restraints from J couplings and the interproton distance restraints from nuclear Overhauser effects (NOEs)[62]. The accuracy of a structure determined by NMR can be further increased by addition of long-range orientational restraints derived from residual dipolar couplings (RDCs)[63] that require, however, heteronuclear labeling to measure proton-heteronucleus couplings. Paramagnetic relaxation enhancement (PRE) have been more recently exploited to get long range distance restraints i.e.

up to ~35 Å under favorable circumstances, and to gain information about state populations[64–67]. The traditional approach based on proton NMR and restraints thereof is no longer applicable when the dimensions of macromolecule (protein, oligonucleotide, oligosaccharide) overcome specific limits because the proton chemical shift dispersion is no longer sufficient to achieve enough resolution. Heteronuclear labeling, especially ^{13}C and ^{15}N, provide the additional frequency scales that enable to increase the chemical shift dispersion space. Unfortunately, this enhanced space can be exploited only within a very limited range of molecular size to extract proton based restraints. As the molecular weight increases, the network of proton dipolar interaction increases too, both in terms of interaction number and induced line broadening. For instance, above certain dimensions (for proteins 35-40 kDa), the dipolar broadening induced by the hydrogen nuclei impairs also the heteronuclear detection and therefore it becomes advantageous to partially deuterate the macromolecule to observe reasonably sharp proton-detected heteronuclear correlations in 2D or 3D spectra exploiting the residual protons. Properly resolved spectra can still be obtained without extensive deuteration using the TROSY technique[68], but in most instances the traditional approach of gaining structural restraints from proton-proton scalar coupling and NOE becomes simply no longer viable to extract a sufficient number of internuclear distances for restrained modeling. Structures however can still be obtained exploiting the heteronuclear chemical shifts that, in spite of a more limited effect due to conformation, are characteristically affected by the local secondary structure. This secondary structure effects are much more interpretable and reproducible than the corresponding proton chemical shifts. As a matter of fact, the overall structure of a protein can be determined through restrained molecular dynamics calculations based on heteronuclear chemical shift restraints that constrain local secondary structure, while a proper force-field and a sufficiently wide database enable discriminating with an energy score among the possible tertiary arrangements that are generated by molecular dynamics.

Biomolecules in a living organisms, especially proteins, are molecular machines which perform biological functions as well as controls of several key events. Specific biological functions of proteins depend on dynamic processes in which the proteins are involved. Although conventional NMR methods for structure determination of biomolecules provide a characterization related to the major state, additional information related to poorly populated states can be obtained. To characterize biomolecular dynamical processes such as protein folding, enzyme catalysis, intermolecular interaction, molecular recognition, structural fluctuations in the side chain and backbone, rotational and translational diffusion, slow and fast internal motion, conformational rearrangements, loop and domain motions etc. on timescale ranging from picoseconds to hours/days, a number of NMR methods have been developed as illustrated in Figure 1.12.

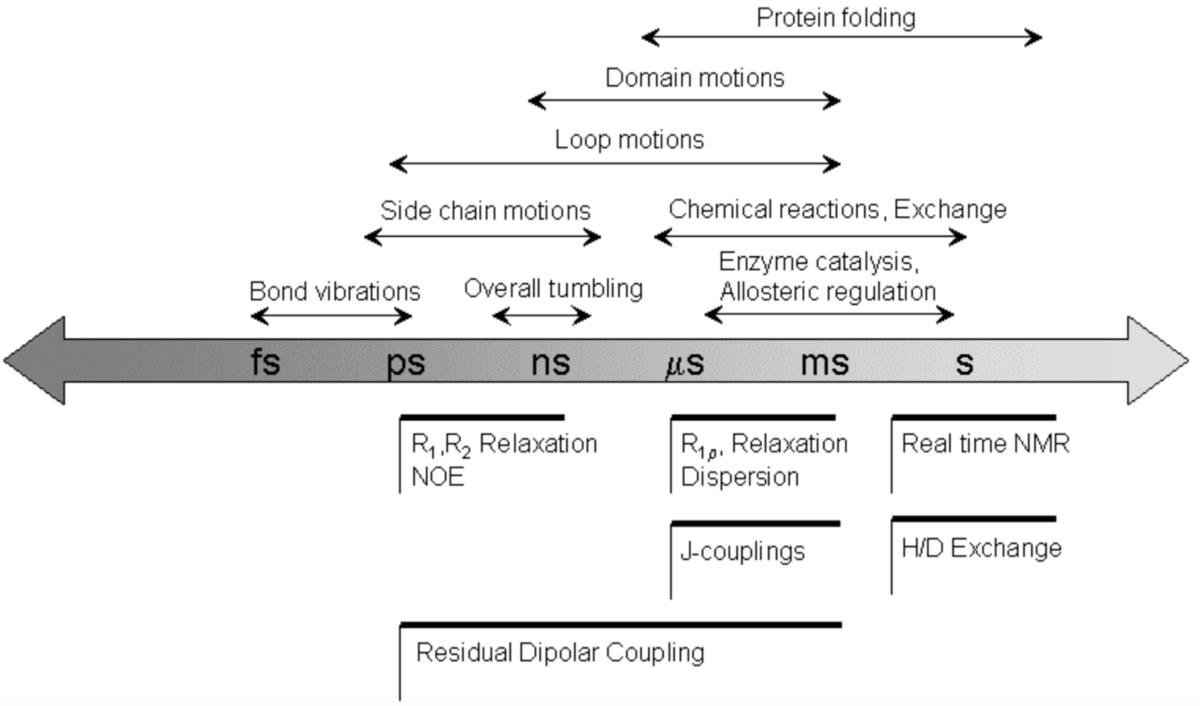

Figure 1.12: NMR methods used to detect and quantify molecular fluctuations or motion on various timescales in proteins

Molecular motion, and in particular rotation, is the principal source of change in NMR relaxation rates. The rotational correlation time (τ_c), which can be considered as the average time taken by the molecule to rotate by one radian, is easily defined for a molecule with spherical symmetry by the Stoke's formula in terms of hydrodynamic radius and absolute temperature. There are many mechanisms of nuclear relaxation that are affected by molecular motions (i) direct interaction or coupling between nearby magnetic nuclei, called dipole-dipole relaxation (DD), (ii) scalar (*J*) coupling between one nucleus to an another fast-relaxing one (typically quadrupolar), named scalar coupling relaxation (SC), (iii) changes of chemical shift because of electron shielding fluctuations, called chemical shift anisotropy (CSA), (iv) electric field gradient and quadrupolar nuclei interaction that cause quadrupolar relaxation (QR).

Fast local motions (ps-ns) in proteins can be studied by NMR relaxation methods[69–72]. Often, ^{15}N nuclei are used to monitor backbone motions, measuring longitudinal (T_1) and transverse (T_2) relaxation times and ^{15}N –^{1}H heteronuclear NOE. The model free formalism framework is well established for the analysis of these measurements[69,71,73], although similar and surely less biased information can be obtained also by spectral density mapping[74–76]. It is quite challenging to monitor dynamic processes taking place in very large molecules. Methyl groups, in this case, have favorable spectral properties and methyl ^{1}H, ^{2}H and ^{13}C nuclei are good probes to measure the dynamic processes[77,78]. These experiments explain the rapid motions occurring in the most representative states of a molecule. However, on the fast time scales and also on the slow ones, i.e. with timescales up to ~250–500 μs, differential relaxation methods based on the paramagnetic relaxation enhancement are capable to describe minor states which are dynamically exchanging with a major states.

Additional NMR methodologies have been developed and proposed to monitor intermediate and slow time scale dynamics. The Relaxation Dispersion method, using either rotating frame relaxation ($R_{1\rho}$) or Carr–Purcell-Meiboom–Gill (CPMG) transverse relaxation (R_2) measurements allows to characterize intermediate i.e. ~0.05–0.1 ms, to slow, i.e. up to10 ms, time scale windows[79–83]. Resonance line shapes analysis can also be used to characterize the intermediate exchange dynamics[84]. The residual dipolar coupling, RDC, determinations can also give information on the μs timescale dynamics[85]. Other techniques such as hydrogen exchange[86,87], saturation transfer[88,89], and heteronuclear zz-exchange spectroscopy[90–92] are used to characterize slower time scale (ms-s) exchange processes. Exchange processes that are even slower (>s) can be monitored by real time NMR. By this approach sequentially acquired NMR data are used to monitor changes[93].

Electron spin resonance (ESR) or electron paramagnetic resonance (EPR) spectroscopy is a powerful method to study materials with unpaired electrons. EPR spectroscopy is analogous to NMR spectroscopy with the difference that in EPR electron spins are excited instead of nuclear spins. EPR applications are also used in protein studies, in particular for the characterization of ligand binding, protein dynamics and molecular orientations. Generally, proteins are not paramagnetic therefore it is required to chemically functionalize the protein with a suitable paramagnetic moiety that becomes an intrinsic probe or to use extrinsic probes which are called spin labels. These probes are typically stable organic radicals, derivatives of piperidine-N-oxyl named also nitroxides, which are soluble in water and expected to sample the protein surface more or less non-specifically. The same class of compounds can also work as intrinsic probes when covalently bound to protein side chains through proper linking groups.

Finally, it is worth mentioning molecular dynamics (MD) simulations that have become a significant tool in examining subtleties of protein dynamics and structure, especially when based on experimental restraints. MD simulations may give information on processes which occur on the nanosecond and sub nanosecond time scale that are best monitored by NMR spectroscopy.

1.5.1 Paramagnetic Relaxation Enhancement

Unpaired electrons have powerful effect on nuclear spin magnetization and these paramagnetic effects are used to extract information about low populated states or to measure long distance structural restraints. There are three NMR experimental observables, namely the very PREs, i.e. the relaxation rate enhancement that can be measured in the presence of paramagnetic intrinsic or extrinsic labeling, the residual dipolar couplings (RDCs) and the pseudocontact shifts (PCSs), which provide long range structural data in systems affected by paramagnetic perturbations. Any paramagnetic perturbation can generate PREs but only the paramagnetic systems which have an anisotropic magnetic susceptibility generate RDCs and PCSs.

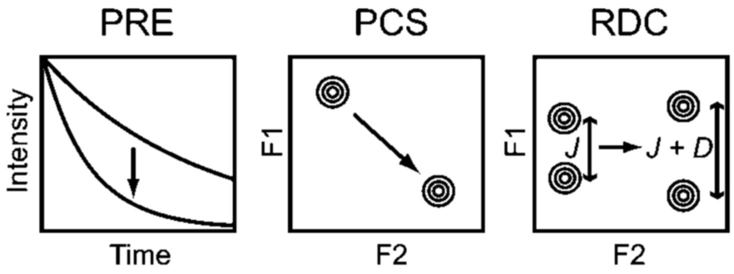

Unpaired electrons:	PRE	PCS	RDC
Isotropic	Yes	No	No
Anisotropic	Yes	Yes	Yes

Figure 1.13[64]**:** Major Long-range observables in Paramagnetic NMR.

PRE is due to the dipolar coupling between an unpaired electron and a nuclear spin that affects the NMR signal intensity and width because of changes in longitudinal and transverse relaxation rates. PRE is proportional to r^{-6}, the distance between the nucleus and the paramagnetic center. Therefore, PRE is distance dependent much like internuclear dipole-dipole interaction that gives rise to NOE. However, PRE can provide distance information up to ~35 Å–when the paramagnetic center is due to some metal ions with multiple unpaired electrons i.e. Gd^{3+} or Mn^{2+} and ~20 Å-for chemically-bound nitroxide tags (intrinsic probes). At short distance, PRE effects are extremely intense and can even lead to bleaching of the NMR signal. If there is an exchange between two unequally populated states and the relaxation enhancement concerns also or exclusively the low-populated state, there will be a contribution of minor (possibly invisible) state in the PRE profile of the major (visible) state. Under these conditions, PRE becomes a powerful technique for characterizing low-populated states[94–98].

The transverse (Γ_2) and longitudinal relaxations (Γ_1) PRE rates arising from dipole-dipole interactions are described by Solomon-Bloembergen (SB) equations[99,100] and expressed in simplified equations[64].

$$\Gamma_2 = \frac{1}{15}\left(\frac{\mu_0}{4\pi}\right)^2 \gamma_I^2 g^2 \mu_B^2 S(S+1)\{4J_{SB}(0) + 3J_{SB}(\omega_I)\} \tag{1}$$

$$\Gamma_1 = \frac{2}{5}\left(\frac{\mu_0}{4\pi}\right)^2 \gamma_I^2 g^2 \mu_B^2 S(S+1)J_{SB}(\omega_I) \tag{2}$$

where γ_I is the proton gyromagnetic ratio (~2·675 × 108 rad s^{-1} T^{-1}), g is the electron *g*-factor (~2·0), $\omega_I/2\pi$ the Larmor frequency of the proton (e.g. 500MHz in a 11.7 T magnetic field), $J_{SB}(\omega)$ is the generalized spectral density function for the reduced correlation function, given by

$$J_{SB}(\omega) = r^{-6}\frac{\tau_c}{1+(\omega\tau_c)^2} \tag{3}$$

where r is the distance between the nucleus and the paramagnetic center, the overall correlation time,τ_c, is defined as $(\tau_r^{-1} + \tau_s^{-1})^{-1}$, where τ_s is the effective electron relaxation time and τ_r is the rotational correlation time of the macromolecule. Values of τ_s is depend on the nature of the paramagnetic probe. Nitroxide paramagnetic probes generally exhibit larger $\tau_s$values[101] i.e. ~10^{-6}, thus in this case of $\tau_c \approx \tau_r$ and paramagnetic metal ions with anisotropic magnetic susceptibility exhibit very small values i.e. for anisotropic lanthanides[67] ~10^{-13}, thus in this case $\tau_c \approx \tau_s$. Paramagnetic metal ions with isotropic magnetic susceptibility exhibit intermediate τ_s values on the same order as τ_r[102–104] i.e. τ_s~ 10^{-8} for Gd^{3+}, τ_s~ 10^{-9} for Mn^{2+}, which introduces difficulties in the simplification of the expression for τ_c.

A paramagnetic probe can also cause relaxation enhancement through Curie spin relaxation arise from the interaction between the nucleus and the time-averaged magnetization of the electrons. The transverse (Γ_2) rate due to Curie-spin relaxation is given by,[105]

$$\Gamma_{2,Curie} = \frac{1}{5}\left(\frac{\mu_0}{4\pi}\right)^2 \frac{(\omega_I^2 g^4 \mu_B^4 S^2(S+1)^2)}{(3k_B T)^2 r^6}\left\{4\tau_r + \frac{\tau_r}{1+(\omega_I\tau_r)^2} - 4\tau_c - \frac{\tau_c}{1+(\omega_I\tau_c)^2}\right\} \qquad (4)$$

In the case of nitroxide spin radicals where $\tau_c \approx \tau_r$ due to relatively long τ_s, Curie-spin relaxation is negligible and the transverse (Γ_2) rate is therefore independent of the magnetic field and in these case τ_r (i.e. molecular weight) is directly proportional to the dipole-dipole transverse (Γ_2) rate. The transverse (Γ_2) rate in the macromolecules is dominated by Curie spin relaxation for the paramagnetic metal ion (very short τ_s) with an anisotropic magnetic susceptibility i.e. Fe^{3+}, Dy^{3+}. For an isotropic paramagnetic metal ion, i.e. Mn^{2+} and Gd^{3+}, the contribution of Curie-spin relaxation is minor and is almost negligible for medium sized (<40 kDa) macromolecules. For example, Curie-spin relaxation contributed 2% of the transverse (Γ_2) rate in the 20 kDa complex of DNA-EDTA-Mn^{2+} and SRY at a ^{1}H-frequency of 800 MHz and 308 K temperature[106]. For very large macromolecule (> 100 kDa), the contribution of Curie-spin relaxation to the transverse (Γ_2) rate is more than 20% at 800MHz[64].

Thus, for measurement of PREs, it is very advantageous to use a paramagnetic probe with an isotropic magnetic susceptibility because of less contribution of Curie-spin relaxation to the transverse (Γ_2) rate compared with anisotropic magnetic susceptibility

The chemical compounds used for paramagnetic perturbation studies in NMR spectroscopy are divided into two categories: (1) stable nitroxide radicals, >N-O•, and (2) metal chelators, such as DTPA, metal binding peptides and EDTA. These two categories of paramagnetic systems can be covalently attached to nucleic acids and proteins and used to study the intermolecular and intramolecular PREs (Figure 1.14A and B)[64]. Small paramagnetic compounds dissolved in a macromolecular solution and therefore used as extrinsic probes give unique information of the macromolecular surface. Random collisions between the paramagnetic co-solute and the macromolecule provide PREs at the accessible locations of the macromolecule to an extent depending on the depth of the observed nuclei with respect to the surface (Figure 1.14C)[64].

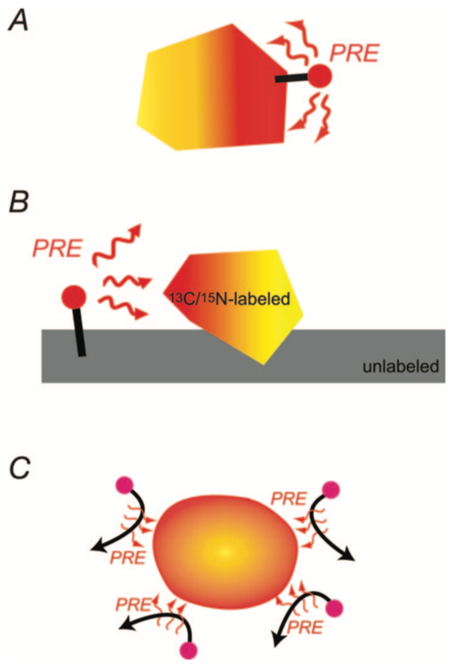

Figure 1.14: Three types of PRE[64]: (A) intramolecular PREs are arising from the center with an unpaired electron within the same molecule; (B) intermolecular PREs are arising from the site with an unpaired electron located on the interaction partner; (C) PREs are arising due to random collisions between a paramagnetic co-solute molecules and macromolecule.

In particular, Tempol and DTPA co-solutes are appropriate probes for solvent accessibility studies because they are neutral, although this neutrality tends to favour interactions with the hydrophobic surfaces of the target macromolecule. Especially with the piperidine-N-oxyl derivatives. Such as Tempo, Tempol, Tempone, etc., the stabilization of the nitroxide is achieved by per-methylation of the nitrogen vicinal carbons that, with charge neutrality, favours hydrophobic interactions. However, the polarity of the nitroxide group as well as of the piperidine system substituents balances somehow that hydrophobicity. Correlation time and diffusion rates of co-solute molecules with the macromolecules add difficulties in the analysis of PREs data. Since the co-solute collisional regime with the macromolecule reminds solvent-solute interactions, the extrinsic paramagnetic perturbation brought about by nitroxides or DTPA derivatives is sometime referred to as solvent paramagnetic labeling, or solvent labeling. Another important application concerns the evaluation of the PRE effects on the solvent when a paramagnetic species is added in solution. Different theoretical methods have been proposed[64,101] to calculate PRE affecting the solvent resonance, including outer sphere model and inner sphere model. If the solvent PRE originates from a paramagnetic probe center which behaves like a diffusing solvent molecule, it is assumed to occur according to the outer sphere model[107]. If the solvent PRE arises from a static or long-lived interaction between the solvent and paramagnetic center, typically when a complex is formed and the solvent becomes a ligand, it is assumed to occur according to the inner sphere model[99,108].

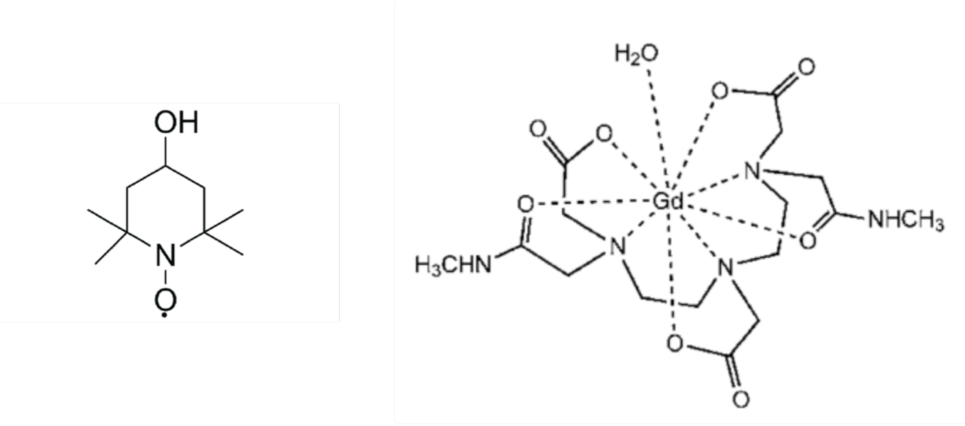

Tempol

Gd(III)-DTPA-BMA

Figure 1.15: Structure of Tempol and DTPA

Generally, PRE is measured by the subtraction of the relaxation rates between a diamagnetic and a paramagnetic condition, namely from the relaxation rate difference in the presence and absence of the paramagnetic perturbation. This subtraction eliminates all common relaxation processes in both diamagnetic and paramagnetic conditions and gives the paramagnetic relaxation contribution. PRE can be measured either by longitudinal relaxation rate (R_1) or transverse relaxation rate (R_2), although the measurement of transverse relaxation rate is more significant and has more advantages over longitudinal relaxation.

The measurement of PRE Γ_2 is given by,[64]

$$\Gamma_2 = R_{2,para} - R_{2,dia} \tag{5}$$

An alternative method is comparing the NMR peak intensities from experiments in a sample with (I_{para}) and without (I_{dia}) paramagnetic probe. The I_{para}/ I_{dia} ratio can be used to gain additional information to the structure calculation of macromolecules which provides exposed and buried residues to the solvent[109,110].

Soluble spin labels have been used by many research groups as a general approach to map protein surfaces and to study protein folding and dynamics[111–113]. Molinari et al. studied the structure Bovine Pancreatic Trypsin Inhibitor (BPTI) from the paramagnetic perturbation of

NMR HSQC spectra and proposed a new protocol for the data acquisition scheme and the related analytical treatment[114]. Those authors used autoscaled attenuations to assess exposed or hindered molecular locations with respect to the average attenuation observed in the presence of a non-specific paramagnetic probe by calculating normalized attenuation (A_N) values lying above or below the unity that represents the average attenuation in the A_N space, according to:

$$A_N^i = \left(2 - \frac{v_p^i}{v_d^i}\right) \tag{6}$$

where the i superscript refers to the cross peak number, related to a molecular positions, $v_{p,d}^i$ are the autoscaled paramagnetic (p subscript) and diamagnetic (d subscript) volumes of the peaks, defined as

$$v_{p,d}^i = \frac{V_{p,d}^i}{\left(\frac{1}{n}\right)\sum_{i=1}^{n} V_{p.d}^i} \tag{7}$$

where n is the total number of measured peaks, $V_{p,d}^i$ are the cross peak volumes measured in the presence (V_p) and absence (V_d) of the extrinsic paramagnetic probe. It is readily appreciated from the above equations that the normalization factor is the mean volume value over n locations of the assigned cross peak volumes or, in general, signal intensity values. By definition, the individual autoscaled volume mean value is unitary,

$$\frac{1}{n}\sum_{i=1}^{n} v_{p,d}^i = 1 \tag{8}$$

It can be seen that the function A_N^i can represent the variation of the autoscaled volume/intensity ratio of each single residue signal. This ratio can range between 0 and 1 under magnetization equilibrium conditions but can also be > 1 under non-equilibrium conditions. To avoid negative values, the front constant was set as 2. This means that autoscaled attenuations larger than the average will correspond to A_N^i larger than 1 (up to a maximum of 2 when $v_p^i = 0$), whereas attenuation smaller than the average will correspond to $A_N^i < 1$. By definition attenuations equal to the average will give $A_N^i = 1$.

The function A_N^i can also be explained using eqs. (8b,c), i.e. the normalized deviation of the paramagnetic-to-diamagnetic volume (or intensity) ratio with respect to the corresponding average ratio, using the same average ratio as normalization constant:

$$A_N^i = \left\{1 - \frac{V_p^i/V_d^i - \langle V_p\rangle/\langle V_d\rangle}{\langle V_p\rangle/\langle V_d\rangle}\right\} \qquad \text{(8b)}$$

where

$$\langle V_{p,d}\rangle = \frac{1}{n}\sum_{i=1}^{n} V_{p,d}^i \qquad \text{(8c).}$$

Again, to avoid negative values, the complement to unity of that normalized deviation is used. The same equations can be written using signal intensities (heights) instead of volumes.

1.5.2 Relaxation Dispersion

Relaxation dispersion NMR experiment gives micro to millisecond exchange information which is very interesting in the field of biochemistry because many functionally dynamic processes occur in this time scale i.e. interdomain motions, conformational changes in proteins during enzymatic catalysis[115,116], and ligand binding to a protein[117]. In this experiment, we are quantifying an intensity variation of the NMR data. The chemical exchange between a major ground state and minor excited states during a repeated spin-echo building block or spin-lock of the NMR pulse sequence results in differences in the peak intensities. This peak intensity varies with applied field frequency. Thus, one can retrace and study the chemical exchange process by quantifying the peak intensities.

If the molecule is undergoing exchange between two states,

$$\begin{gathered} k_{AB} \\ A \rightleftharpoons B \\ k_{BA} \end{gathered}$$

Then the number of peaks observed will depend on the exchange rate constant ($k_{ex} = k_{AB} + k_{BA}$) and difference in the chemical shifts ($\Delta\omega$) between two states. If the change in chemical shift difference is larger than k_{ex}, the system is in the so-called slow exchange where we see two distinct peaks for the resonance and if k_{ex} is instead much larger than chemical shift difference, the system gives a single peak which is the population-weighted mean chemical shift called fat exchange. In a relaxation dispersion experiment, the NMR signal intensities vary as a function of applied field in the presence of chemical exchange during fixed delay of the pulse sequence (Figure 1.16). When the amplitude of the applied field is weak, low signal intensities are observed (red in Fig 1.16, large effective R_2) and by increasing the applied field strength the signal intensity will also increase (i.e. blue in Fig 1.16, low effective R_2). In the absence of the chemical exchange, the signal intensities do not vary with amplitude of applied field and a flat profile obtained.

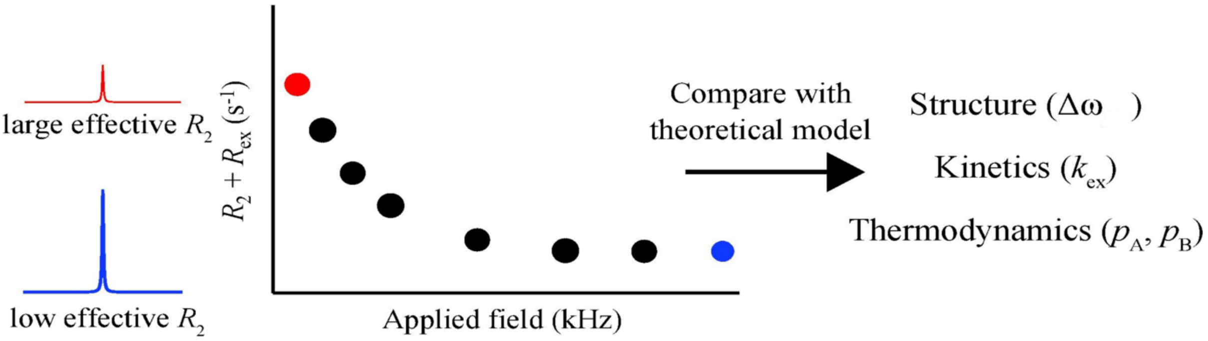

Figure 1.16: Schematic representation of relaxation dispersion profile[118].

There are two distinct relaxation dispersion NMR experiments have been developed (1) CPMG (R_2) relaxation dispersion and (2) $R_{1\rho}$ relaxation dispersion. In the CPMG relaxation dispersion, the effective transverse relaxation rate (R_2^{eff}) is measured as a function of applied field or CPMG field ($\nu_{CPMG}\,[Hz]$). This CPMG train is composed of repetitions of 180^0 pulses and pairs of the delays between 180^0 pulses is given by,

$$\nu_{CPMG} = \frac{1}{2\tau_{CP}} \tag{9}$$

The effective transverse relaxation rate (R_2^{eff}) for the two-state exchange is given by[119]

$$R_2^{eff} = \frac{1}{2}\left(R_{2,A}^0 + R_{2,B}^0 + k_{ex} - [2\nu_{CPMG}]cosh^{-1}[D_+ cosh(\eta_+) - D_- cos(\eta_-)]\right) \tag{10}$$

where,

$$D_\pm = \frac{1}{2}\left[\pm 1 + \frac{\psi + 2\Delta\omega^2}{\sqrt{\psi^2 + \zeta^2}}\right] \tag{11}$$

$$\eta_{\pm} = \tau_{CP}\sqrt{\frac{1}{2}\left(\pm\psi + \sqrt{\psi^2 + \zeta^2}\right)} \qquad (12)$$

$$\psi = \left(R^0_{2,A} - R^0_{2,B} - p_A k_{ex} + p_B k_{ex}\right)^2 - \Delta\omega^2 + 4 p_A p_B k_{ex}^2 \qquad (13)$$

$$\zeta = 2\Delta\omega\left(R^0_{2,A} - R^0_{2,B} - p_A k_{ex} + p_B k_{ex}\right) \qquad (14)$$

and, $R^0_{2,A}$ and $R^0_{2,B}$ are the R_2 of the state A and B in the absence of chemical exchange respectively, p_A and p_B are the population state of ground state A and excited state B respectively.

A simplified equation for R_2^{eff} for fast exchange regime is given by[120]

$$R_2^{eff} = p_A R^0_{2A} + p_B R^0_{2B} + \left(\frac{p_A p_B \Delta\omega^2}{k_{ex}}\right)\left(1 - \frac{4\nu_{CPMG}}{k_{ex}} tanh\left[\frac{k_{ex}}{4\nu_{CPMG}}\right]\right) \qquad (15)$$

If the population of ground state A is greater than excited state B, the expression for can be simplified to[121]

$$R_2^{eff} = R_2^0 + \frac{p_A p_B \Delta\omega^2 k_{ex}}{k_{ex}^2 + \left(p_A^2 \Delta\omega^4 + 48[2\nu_{CPMG}]^4\right)^{1/2}} \qquad (16)$$

where R_2^0 is equal to $p_A R^0_{2A} + p_B R^0_{2B}$ in fast exchange and $R^0_{2,A}$ in the slow exchange regime.

In the rotating frame relaxation dispersion, the effective rotating frame relaxation rate ($R_{1\rho}^{eff}$) is the sum of the intrinsic relaxation rate ($R^0_{1\rho}$) and the contribution from chemical exchange ($R_{ex,1\rho}$), which is attenuated by the spin-lock field.

$$R_{1\rho}^{eff} = R^0_{1\rho} + R_{ex,1\rho} \qquad (17)$$

A coherence decays at the $R_{1\rho}^{eff}$ in the presence of spin-lock field, which is a function of spin-lock offset and the applied spin-lock power.

The effective transverse relaxation rate ($R_{1\rho}^{eff}$) for the two-state exchange is given by[120,122,123]

$$R_{1\rho}^{eff} = R_{1\rho}^{0} + \frac{p_A p_B \Delta\omega^2 k_{ex}}{k_{ex}^2 + \omega_e^2} sin^2\theta \tag{18}$$

where $R_{1\rho}^{0}$ is the intrinsic relaxation rate or $R_{1\rho}$ in the absence of exchange (i.e. $\omega_e = \infty$) and the angle between the static B_0 filed and the spin-lock B_1 field is given by,

$$\theta = \tan^{-1}\frac{\omega_1}{\delta\omega} \tag{19}$$

where $\delta\omega$ is the offset frequency and ω_1 is the strength of spin-lock field. The strength of effective spin-lock field is given by,

$$\omega_e = \sqrt{\omega_1^2 + \delta\omega^2} \tag{20}$$

If the population of ground state A is greater than excited state B and on resonance with respect to spin-lock field ($\delta\omega=0$), $R_{1\rho}^{eff}$ is expressed as[124]

$$R_{1\rho}^{eff} = R_{1\rho}^{0} + \frac{p_A p_B \Delta\omega^2 k_{ex}}{k_{ex}^2 + p_A^2\Delta\omega^2 + \omega_1^2} \tag{21}$$

As long as the population of excited state is very small, for off resonance spin-lock field, $R_{1\rho}^{eff}$ is expressed as[125]

$$R_{1\rho}^{eff} = R_{1\rho}^{0} + \frac{p_A p_B \Delta\omega^2 k_{ex}}{k_{ex}^2 + \omega_{e,A}^2\omega_{e,B}^2/\omega_{e,ave}^2} \tag{22}$$

where $\omega_{e,A}$ and $\omega_{e,B}$ are the effective spin-lock field for the chemical shift of state A and B respectively and $\omega_{e,ave}$ is the effective spin-lock field of population averaged chemical shifts of A and B

An advantage of $R_{1\rho}$ relaxation dispersion experiments over R_2 relaxation dispersion experiments is that $R_{1\rho}$ experiments can give faster exchange process information than R_2 experiments. R_2 experiments can be used to study the exchange on a time scale ~0.5ms-5ms where as $R_{1\rho}$ experiments are used to measure the exchange process as fast as k_{ex} < 40000 s^{-1} or τ_{ex} >0.025ms[126–128].

The sample requirement for the relaxation dispersion NMR experiment is same as conventional 3D NMR experiments. The sample concentration should be ~ 1mM with high purity monodisperse solution to get good signal to noise ratio. Relaxation dispersion data basically obtained from 2D NMR experiments but many data points i.e. 15-20 are required including repeated measurements to get proffer fitting to yield full profile and for error estimation. To make data collection easy the pulse program is written in pseudo-3D and the third dimension is relaxation dispersion specific parameter (ν_{CPMG}). For the RNA and proteins, the NMR sample should be stable for couple of weeks at room temperature and it should not undergo degradation for the duration of the experiment and the measurement temperature. The isotopic enrichment is highly recommended[118].

2. AIM OF THE THESIS

This PhD thesis deals with the conformational dynamics of proteins by NMR spectroscopy. Proteins perform most of the involved biological processes needed to sustain life. Protein functions typically involve motions[129–131] with conformational dynamics which are playing significant role in allosteric regulation, enzyme catalysis and molecular recognition. NMR spectroscopy is a very important tool to quantify biomolecular dynamics over a wide range of timescale. The most commonly used NMR experiments for characterizing biomolecular dynamics in the μs–ms time-window include $R_{1\rho}$[132] and Carr–Purcell–Meiboom–Gill (CPMG)[120] relaxation dispersion techniques. These experiments required ~1 mM concentration, homogeneous, isotopic labelled protein sample, sample should be stable for more than week, one should have programming knowledge to fit an equation to find out unknown values, and experiment should be collected at different magnetic field for the accuracy. Achieving these conditions i.e. concentration, homogeneous, and stability can be very difficult for amyloidogenic proteins[118]. At ~1 mM concentration there will be contribution of two exchange processes (chemical and conformational) and it is difficult to distinguish between them. Moreover, concentrations of ~1 mM are rarely possible with amyloidogenic proteins. To overcome these problems, the PhD project presents here an alternative qualitative NMR method to analyze exchange processes occurring in proteins by using paramagnetic probe. The method can be considered a new application of extrinsic spin labels in protein NMR. To reach this aim we used Tempol as paramagnetic probe with amyloidogenic proteins i.e. β2m, β2m mutant D76N and HEWL.

3. RESULTS AND DISCUSSION

3.1 Exploring exchange processes in proteins by paramagnetic perturbation of NMR spectra

3.1.1 Interaction model assessment

As detailed in Materials and Methods, we collected the HSQC NMR spectra of β2m in the presence and absence of Tempol with different relaxation delays. By considering the data obtained with extreme delay values, namely 0.5 s and 4 s at 298 K, and 0.5 s and 5 s at 310 K, we explored the NMR magnetization equilibrium and off-equilibrium regimes of steady state observation. Extrinsic paramagnetic probes such as Tempol can be employed to map the accessible surface of proteins[111,112,114,133–136]. In fact, when specific interactions between the probe and the protein are absent and only very weak adducts occur, a statistical collisional model[137] can be adopted to account for the contribution to the protein signal attenuation. This attenuation, arising from the unpaired electron of the nitroxide, is modulated, in principle, by the translational diffusion of the interacting species, thereby identifying directly the exposed surface. Not only signal attenuation due to changes in transverse relaxation rates, but also increase of longitudinal relaxation rates ensue under these conditions[137]. Most importantly, the translational-diffusion-modulated contribution to the relaxation operates for all the solution molecules other than those instantaneously involved in the labile adduct with the paramagnetic probe, just like a relaxation contribution extending to the outer space of the radical interaction sphere. Thus outer-sphere relaxation affects any species in solution, independently of the particular interaction extent with the radical probe. In practice, outer-sphere relaxation is measurable only on solvents or in conditions of sufficient concentration of the probed solute. This is no longer the case when the lifetime of the radical adducts approaches the limits of diffusion-controlled exchange (~10^{-8} s). A statistical collision model can be safely adopted to interpret nitroxide-induced relaxation enhancements of a particular target molecule, if the relative paramagnetic perturbation propagates with the ratio of the statistical collision probability[134]. The effects can be measured in conditions of excess of radical with respect to the target species concentration and have therefore been referred to as solvent perturbation by soluble spin labels[133]. The validity of the collisional model assumptions can be verified[114,133]. For the system addressed here, the extent and linearity of the chemical shift differences, measured in preliminary ^{15}N-^{1}H HSQC spectra up to a Tempol/protein concentration ratio of

~120, i.e. well beyond the value that was considered for the study, shows that there is no specific interaction between the protein and the paramagnetic probe (Figure 3.1A). This is confirmed also by the invariance of the nitroxide line width, estimated from ESR spectra in the absence and presence of β2m (Figure 3.1B). Analogous conclusions had been established also for HEWL[133].

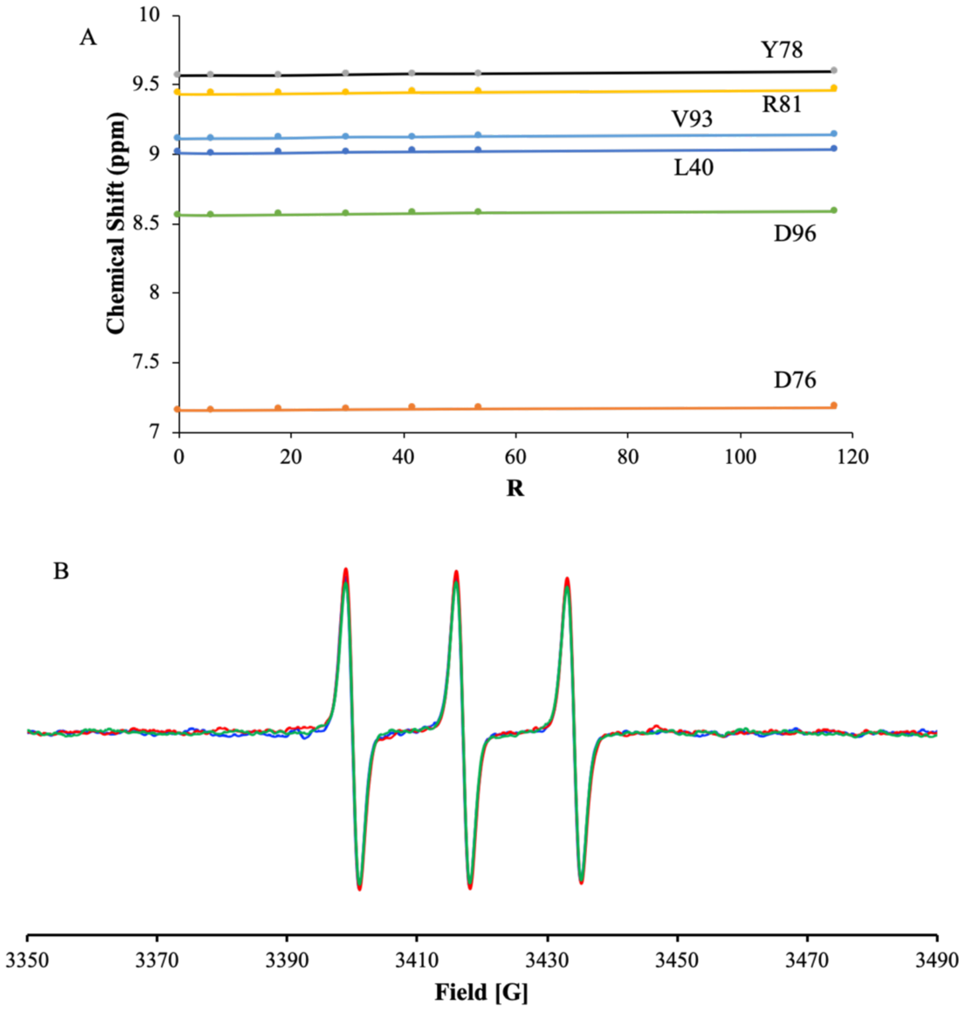

Figure 3.1: (A) Amide hydrogen chemical shifts of a selected group of β2m residues measured as a function of the Tempol/ protein concentration ratio (R). (B) Overlay of ESR spectra of Tempol (blue) and Tempol: β2m, 1:1 (red) and Tempol: β2m, 1:5 (green).

Under the selected concentration conditions, corresponding always to a Tempol:protein ratio of 5, the relative intensity, *RI,* value of a β2m amide cross-peak changes depending on whether on-equilibrium signal (long relaxation delay) or off-equilibrium signal (short relaxation delay) is acquired. More precisely, by collecting equilibrium signal we recovered relative peak intensities below unity, as expected from a general paramagnetic attenuation affecting all positions and in particular the accessible surface locations. Average relative intensity, RI_{av}, values (± standard deviations) of 0.955±0.146 at 298 K and 0.942±0.102 at 310 K were obtained in fact. On the other hand, under off-equilibrium conditions, larger RI_{av} values were measured (above unity) for concentrated samples i.e. 1.079±0.148 at 298 K and 1.181±0.138 at 310 K (Figure 3.2)

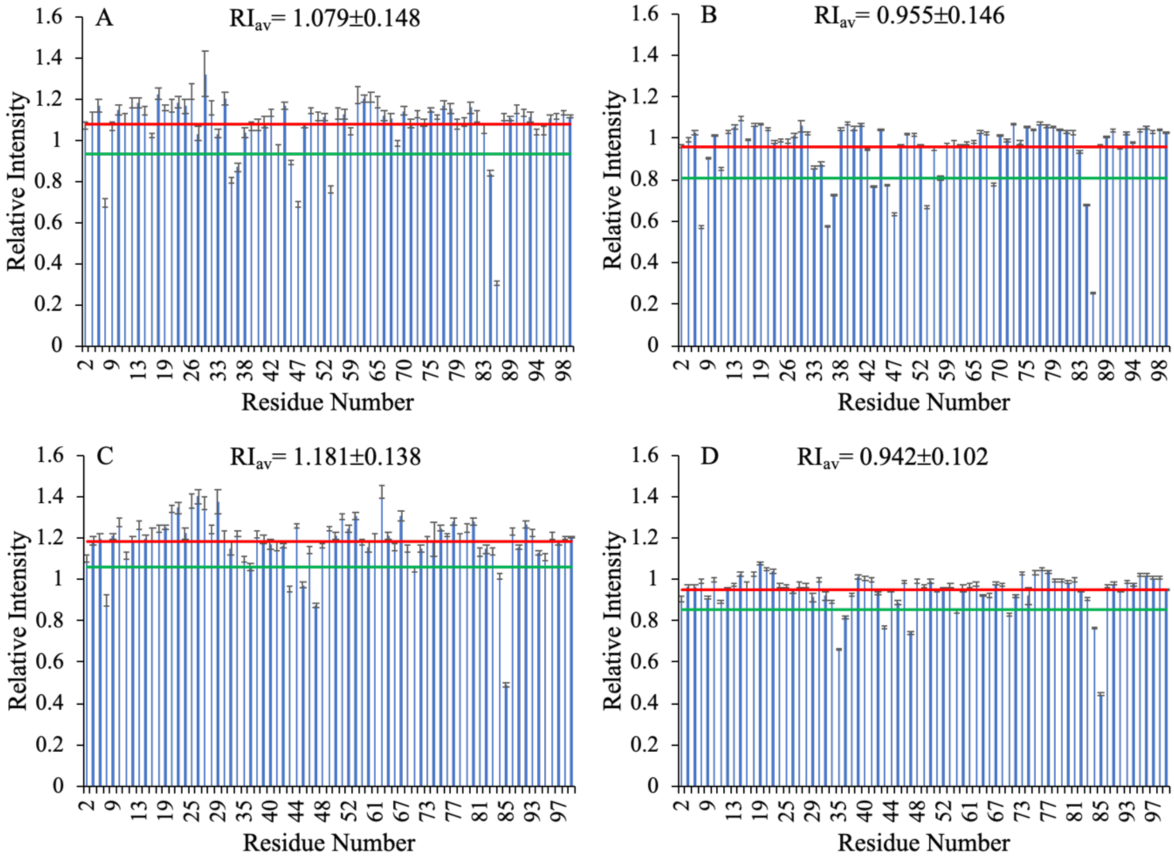

Figure 3.2: Relative intensity of individual backbone NH signals from HSQC spectra measured for 320 µM β2m samples, with and without 1.6 mM Tempol, at different temperatures and relaxation delays (D1): (A) D1= 0.5 s at 298 K; (B) D1= 4 s at 298 K; (C) D1=0.5 s at 310 K; (D) D1=5 s at 310 K. The red and green lines represent the average relative intensity and the displacement by one standard deviation, respectively.

featuring the well-known effect of relaxation agents, such as chromium acetyl-acetonate, that accelerate the signal recovery by shortening T_1, thereby enabling fast recycling rates. Instead, for a diluted β2m sample (50 µM), the equilibrium and off-equlibrium RI_{av} values were nearly coincident, 0.968±0.029 and 0.967±0.025, respectively (Figure 3.3), because the lower concentration of the nitroxide (250 µM) and the consequent reduction of its mole fraction entail a decrease of the statistical collision probability[134].

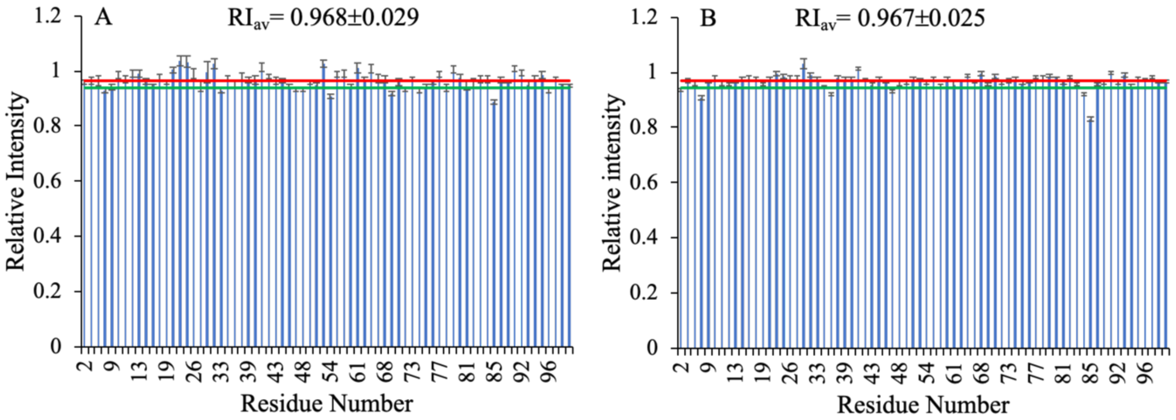

Figure 3.3: Relative intensity of individual backbone NH signals from HSQC spectra measured for 50 µM β2m samples, with and without 250 µM Tempol, at 298 K and different relaxation delays (D1): (A) D1= 0.5 s; (B) D1= 4 s. The red and green lines represent the average relative intensity and the displacement by one standard deviation, respectively.

3.1.2 Equilibrium attenuation

Analysis of the paramagnetic attenuation of the protein spectra is most profitably conducted by calculating normalized attenuation values, A_N (Eq.23), that highlight immediately any effect above or below the average perturbation[114]. Figure 3.4 shows the overlay of the ^{15}N-^{1}H HSQC A_N values from the data collected with 0.5 or 4 s relaxation delay, at 298 K, and with 0.5 or 5 s relaxation delay, at 310 K. The residue amide cross-peaks that, within the experimental error, are attenuated above the average under equilibrium conditions (A_N [eq] > 1), i.e. in spectra recorded with relaxation delay of 4 or 5 s, are listed in Table 3.1 and highlighted in the cartoon presentations of Figure 3.5. Those locations represent the amide groups that are exposed on the surface the protein presents to the sampling Tempol probe[111,133], consistently with the A_N definition[114].

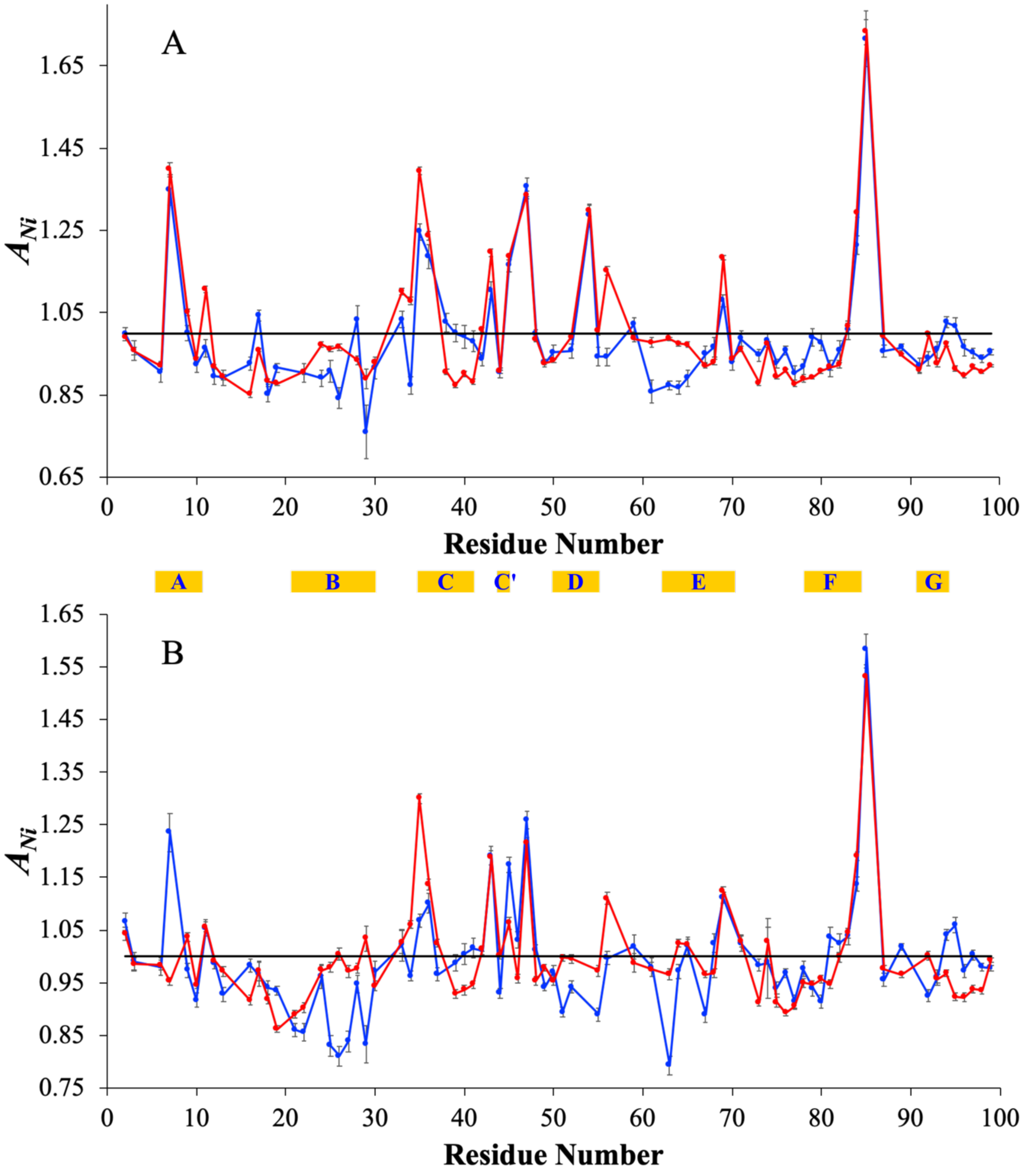

Figure 3.4: Overlay of the A_N values obtained from ^{1}H-^{15}N HSQC spectra of 320 µM β2m in presence of 1.6 mM Tempol, at 298 K with relaxation delay of 0.5 s (blue) or 4 s (red) (A), and at 310 K with relaxation delay of 0.5 s (blue) or 5 s (red) (B).

Table 3.1: Tempol perturbation on the NMR spectrum of 320 μM β2m at different temperatures. Equilibrium attenuations above average[a].

A_N **[*eq*] > 1 ≡ accessible surface**		
Structure region	*298 K*	*310 K*
N-term, strand A	I7, **V9**, **S11**	Q2, **V9, S11**
loop AB		
strand B		G29
Loop BC	**S33, D34**	**S33, D34**
strand C	**I35, E36,**	**I35, E36**, V37
turn CC', strand C', loop C'D	**N42, G43, R45, E47**	**N42, G43, R45, E47**
strand D	L54, **F56**	**F56**
Loop DE		
Strand E	**E69**	L64, L65, **E69**
Loop EF		T71
Strand F	**N83, H84**	**N83, H84**
Loop FG	**V85**	**V85**
strand G, C-term		

[a]The residues whose backbone NH signals are attenuated above the average attenuation in equilibrium conditions (A_N [*eq*] > 1), define exposed positions of the protein, if no specific interaction occurs with the spin label. The positions that appear at both temperatures are reported in bold. Here and elsewhere the assessments concerning any A_N value, e.g. A_N [*off-eq*] > 1, are based on the experimental errors calculated as detailed in the text.

Precisely, at 298 K, the exposed locations map to residues of strand A, loop BC, strand C, turn CC', loop C'D, disordered end of strand D, loop EF, end of strand F and start of loop FG. At 310 K, exposed locations with A_N [*eq*] > 1 are substantially found at the same positions, except for the additional involvement of N-terminal, strand B, strand E and the slight extension of loop EF accessibility. For all these additional entries, rather marginal increments above the average are observed. The overall pattern at 310 K (Figure 3.4B), however, displays a sharp reduction of accessibility extent in strand A and, in terms of absolute A_N [*eq*] values, also in CD loop and EF loop regions. The effect could be attributed to local dynamics increase that reduces the paramagnetic relaxation enhancement, or/and to a variation of the association pattern of the protein with temperature. A 100 ns molecular dynamics simulation to assess the β2m surface

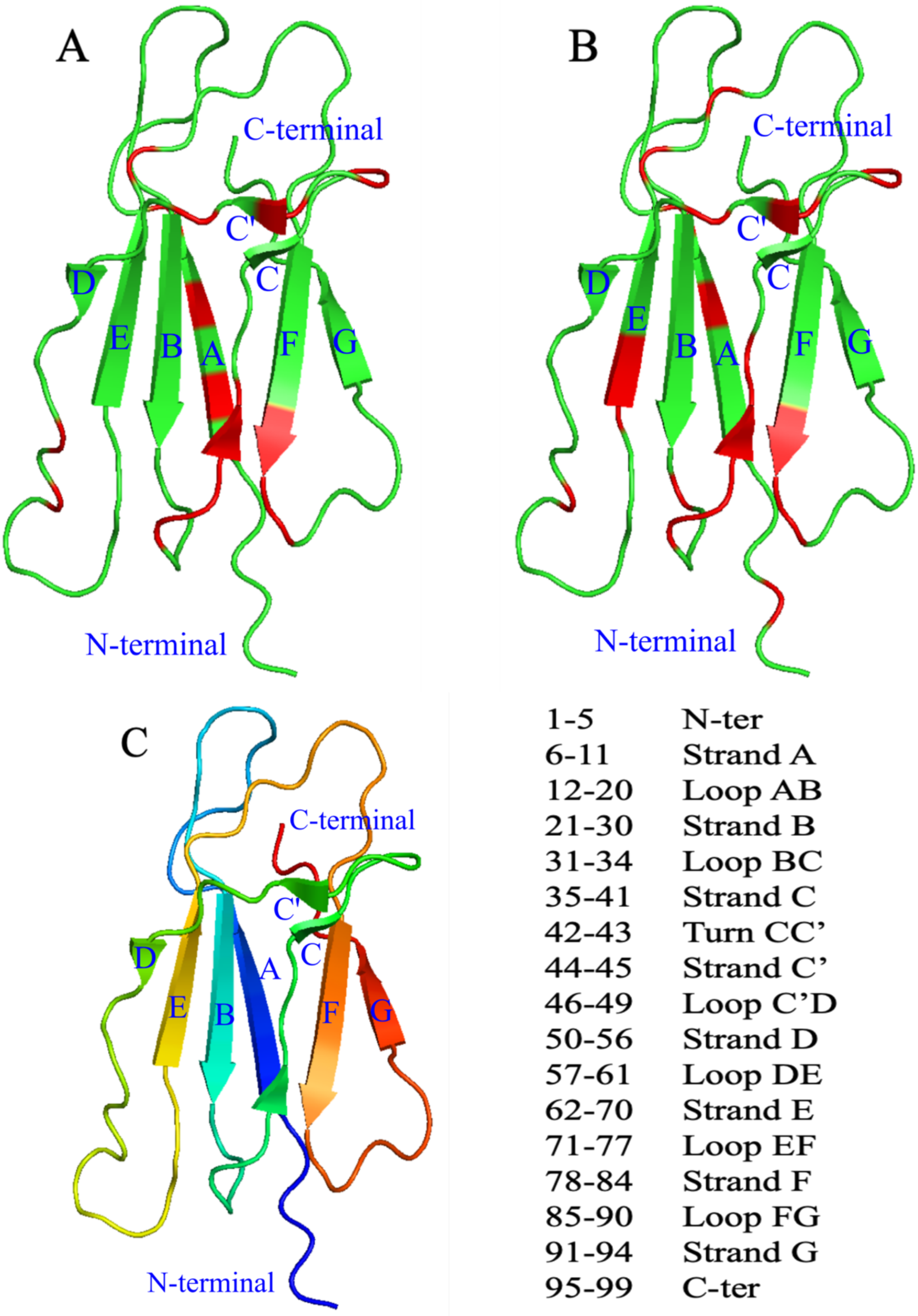

1-5	N-ter
6-11	Strand A
12-20	Loop AB
21-30	Strand B
31-34	Loop BC
35-41	Strand C
42-43	Turn CC’
44-45	Strand C’
46-49	Loop C’D
50-56	Strand D
57-61	Loop DE
62-70	Strand E
71-77	Loop EF
78-84	Strand F
85-90	Loop FG
91-94	Strand G
95-99	C-ter

Figure 3.5: Location of the exposed backbone amides of β2m (in red) whose NMR signals are attenuated above the average value ($A_N\,[eq] > 1$) by Tempol spin label at 298 K (A) and 310 K (B). The data refer to experiments acquired under magnetization equilibrium conditions on a 320 μM protein sample. Here and elsewhere the reproduced structure is the NMR solution structure of β2m[13] (PDB code 1JNJ). (C) Secondary structure elements of β2m according to the crystallographic naming scheme (PDB code 3HLA) and corresponding locations in the solution tertiary structure. Structures were drawn with Pymol (Schrödinger, Inc.).

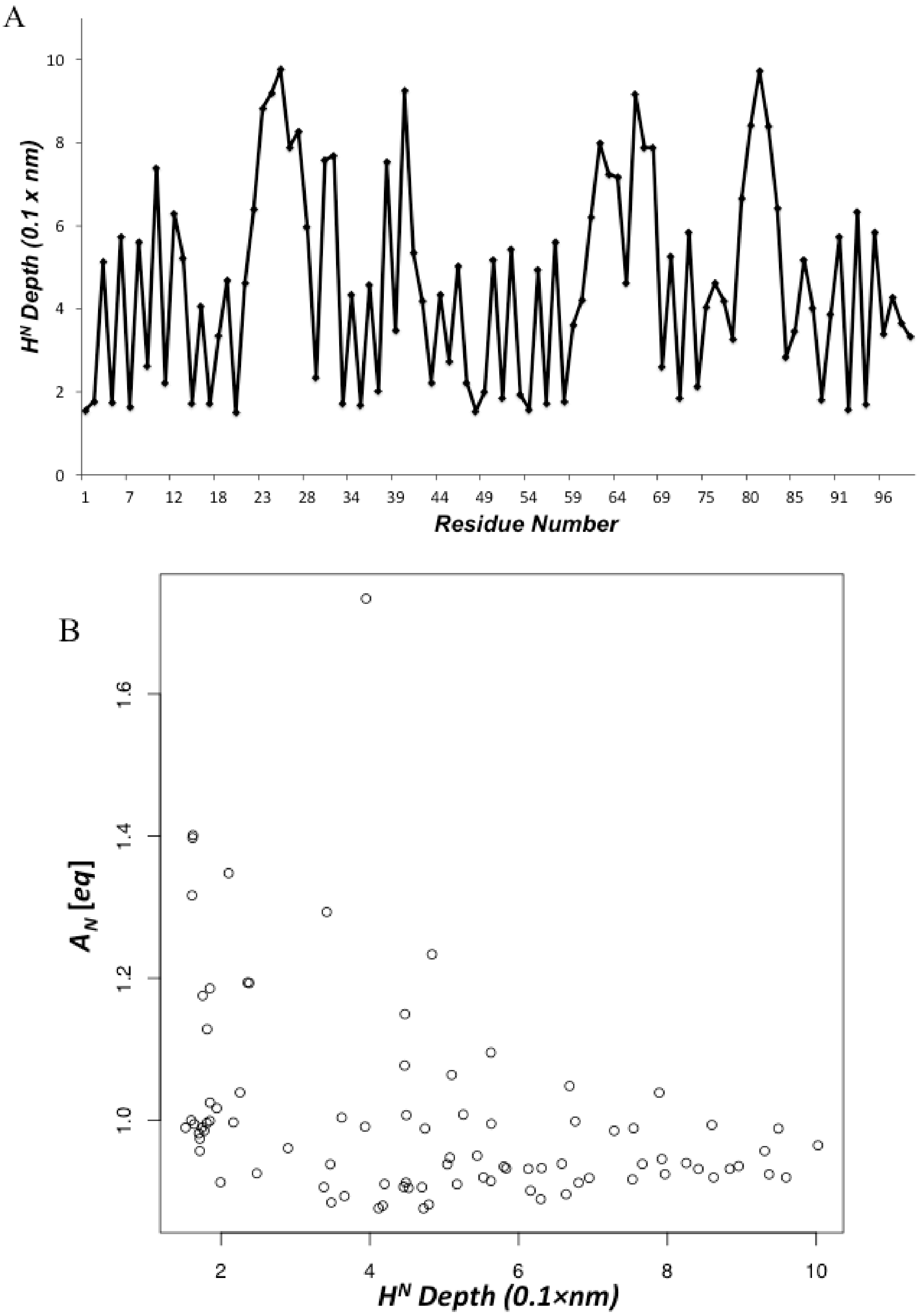

Figure 3.6: (A) Average depth from surface of β2m amide hydrogens throughout 100 ns MD simulation. (B) Experimental A_N [*eq*] values against computed average depth of β2m amide hydrogens. The correlation has a *p* value of 4.5×10^{-4} and is therefore statistically meaningful.

accessibility with Tempol provided a coarse qualitative correlation between the experimentally derived $A_N\,[eq]$ values (Figure 3.4) and the average depth of the backbone amide hydrogens from the structure surface. Despite the fine structure loss of the computed accessibility, that correlation remains, however, statistically meaningful (p value 4.5×10^{-4}). The relative illustrations are reported in Figure 3.6.

This confirms that the translational-diffusion-modulated processes leading to the changes in relaxation rates that are reported by the A_N values can not be accounted only in terms of adduct geometry and distances[138–142]. While stressing again the qualitative significance of any A_N-based inference on the surface accessibility[111,112,114,133–136], molecular dynamics does not add additional insights into the interpretation and therefore will not be further considered.

3.1.3 Off-equilibrium attenuation

The normalized attenuation pattern obtained for off-equilibrium conditions (0.5 s relaxation delay) does not properly mirror the results observed in equilibrium conditions (Figure 3.4). The strongest attenuations, featuring the most exposed NHs on the protein surface, are essentially confirmed also in the data from fast-recycling acquisitions (with exceptions such as F56 that can be explained). Deviations, however, are seen mostly for those amides with $A_N\,[eq] \leq 1$, i.e. NHs displaying normalized attenuations equal or below the average at equilibrium. In particular, two types of deviations can be distinguished, namely $A_N\,[\mathit{off\text{-}eq}] > A_N\,[eq]$, (Type I) and $A_N\,[\mathit{off\text{-}eq}] < A_N\,[eq]$ (TypeII), as specified below.

Type I: amide sites with increased normalized attenuation in off-equilibrium acquisitions compared to equilibrium ones ($A_N\,[\mathit{off\text{-}eq}] > A_N\,[eq]$). This behavior arises typically, but not exclusively, from those locations that exhibit $A_N\,[eq]$ values below the average due to specifically hindered accessibility of the backbone NH of a superficial residue or to genuinely internal position of the amide group residue, i.e. structural burial. When short relaxation delays are employed, it is reasonable that the slowly recovering signals of those amide resonances that are inherently scarcely affected by the paramagnetic probe, result relatively less intense than the fast-recovering exposed amides. Therefore, the relative weight of the corresponding intensities with respect to the overall signal will be reduced, leading to the increase of the normalized attenuation. The pattern $A_N\,[\mathit{off\text{-}eq}] > A_N\,[eq]$ highlights features of the protein structure enabling one to assess hampered accessibility, i.e. a complementary information with respect to the accessibility outline obtained from A_N [*eq*] data. At 298 K, besides a few isolated positions in B strand, DE loop and FG loop, this pattern is detected for the AB loop central segment, most of the C strand, strand E end, most of loop EF, part of the following strand F and the whole C-terminal fragment (Figure 3.4A, Table 3.2). Apart from local increments of accessibility (loop DE, strand E, loop EF, strand F), fairly similar results are observed also for the data collected at 310 K, with two important differences at strand A and loop C'D that show accessibility restriction (Figure 3.4B, Table 3.2).

Table 3.2: Tempol perturbation on the NMR spectrum of 320 μM β2m at different temperatures. Off-equilibrium attenuations with Type I deviations[a].

A_N [*off-eq*] > A_N [*eq*] ≡ hindered accessibility		
Structure region	*298 K*	*310 K*
N-term, strand A		I7
loop AB	**E16**, N17, **K19**	**E16, K19**
strand B	S28	F30
Loop BC		
strand C	D38, **L39, L40, K41**	**L39, L40, K41**
turn CC', strand C', loop C'D		R45, I46, E47, K48
strand D		
Loop DE	D59	
Strand E	Y67, **T68**	**T68**
Loop EF	T71, **T73, K75, D76**, E77	**T73, K75, D76**
Strand F	**Y78**, A79, C80, V82	**Y78,** R81
Loop FG	**Q89**	V85, **Q89**
strand G, C-term	**K94, W95, D96, R97, D98**, M99	**K94, W95, D96, R97, D98**

[a] The residues whose backbone NH signals are more attenuated than the corresponding equilibrium attenuations (A_N [*off-eq*] > A_N [*eq*]), identify positions of the protein with hindered accessibility. The positions that appear at both temperatures are reported in bold.

These are the same regions that appear to reduce their exposure with temperature when considering the A_N [*eq*] values above unity (Table 3.1, Figure 3.5). Reaching concurrently the same conclusion as inferred from Type I deviation of A_N [*off-eq*] by considering the A_N [*eq*] values at different temperatures adds further confidence to the interpretation of the pattern A_N [*off-eq*] > A_N [*eq*]. The occurrence of this Type I off-equilibrium deviations of normalized attenuations demonstrates additional structural diagnostic capabilities of the paramagnetic perturbation from water-soluble nitroxides[114,133]. For instance, the accessibility limits of the central segment of loop AB, unexpected at first glance for an apical loop of the molecule, reflects the inward folded orientation adopted in solution by AB loop (that nearly lays down onto the apex of loop EF)[13], other than the outward protruding geometry the same AB loop adopts in the crystallographic structures of wild type β2m and the vast majority of the mutants[143,144];

Type II: amide sites with decreased normalized attenuation in off-equilibrium acquisitions compared to equilibrium acquisitions (A_N [*off-eq*] < A_N [*eq*]). The amide signals exhibiting Type II deviation of normalized attenuations have no restriction in their A_N [*eq*] value which can span the whole range above and below the average attenuation, under either equilibrium and off-equilibrium conditions. When the attenuation of a signal acquired with short relaxation delay is lower than the corresponding counterpart obtained in equilibrium conditions, an enhancement of the relative weight of that signal with respect to the overall sampled intensity must have occurred because of accelerated magnetization recovery. Hence the comparison between normalized attenuations measured under off-equilibrium and equilibrium conditions is capable of identifying amide locations whose signals undergo a particularly efficient recovery. It is clear that this efficient recovery is contributed by the nitroxide through the outer sphere paramagnetic longitudinal relaxation rate enhancement, R_{1p}. The latter is defined by the analytical expressions reported by Hubbard for the diffusional interaction model[137], along with the corresponding transverse analogous, R_{2p}. Under a statistical collision regime, nitroxides can enhance relaxation of other solution components only by diffusion-rate-modulated dipolar interactions because their electronic relaxation rates are about two orders of magnitude slower than the relevant diffusion processes in systems amenable to high resolution NMR analysis[138]. An efficient recovery observed in fast recycling acquisitions at some distinct protein amide locations is thus the highlighted effect of the R_{1p} contribution acting onto increased local coherence loss, i.e. accelerated transverse relaxation. As previously pointed out, in fact, R_{1p} and R_{2p} contributions can be regarded as outer sphere relaxation that act everywhere on the protein nuclei. Specific amide transverse relaxation rates that prove faster than elsewhere suggest the occurrence of contributions other than the ordinary dipolar and chemical shift anisotropy mechanisms (the latter being relevant only for ^{15}N relaxation). Therefore, the pattern A_N [*off-eq*] < A_N [*eq*], i.e. diminished attenuation of the off-equilibrium auto-scaled intensities – which seems paradoxical at first glance for a parameter expected to report paramagnetic perturbation – identifies amide sites whose transverse relaxation rates are likely to include exchange contributions from local processes of structural interconversion, or intermolecular interactions, typically occurring over a μs-to-ms time scale. This time scale entails a secular contribution to the transverse relaxation, i.e. a further spreading of the Larmor frequencies of the transverse coherences that increases their probability of transition induced by the diffusion-modulated local field of the nitroxide unpaired electron. The ensuing transitions determine the paramagnetic contribution to both longitudinal and transverse relaxation, i.e. R_{1p} and R_{2p}. The mechanism of enhanced recovery of off-equilibrium magnetization in the presence of a nitroxide is reproduced by the experiment reported in Figure 3.7.

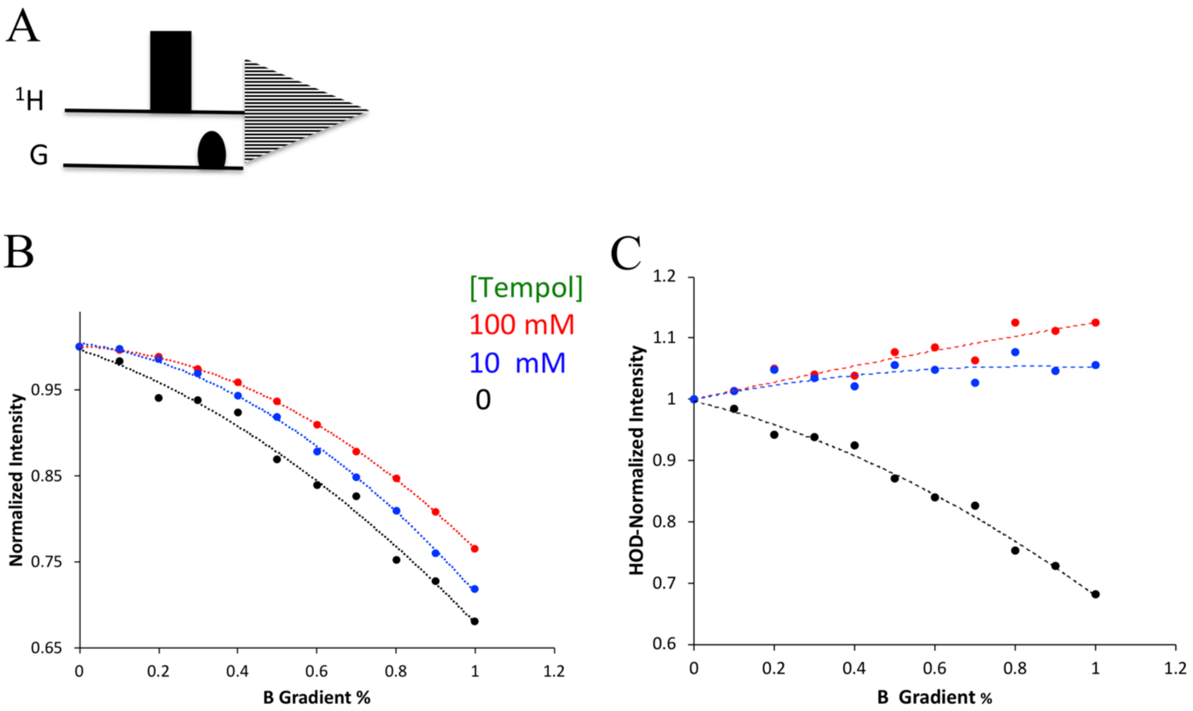

Figure 3.7: (A) NMR experiment carried out on HOD, in the absence and presence of Tempol, to highlight the enhanced recovery of the off-equilibrium magnetization. Below the ^{1}H pulse line, the G line indicates the magnetic gradient pulse timing. (B) HOD signal intensity as a function of the B (magnetic field induction) gradient strength obtained with the sequence sketched in panel A, in the absence (black) and in the presence of 10 mM (blue) or 100 mM (red) Tempol. Each series of values was normalized to the respective value obtained at zero B gradient. (C) Same as in panel B, but with double normalization for the data acquired in presence of Tempol, namely with an additional initial scaling with respect to the corresponding intensities sampled in the absence of Tempol, prior to applying the zero-gradient-value normalization within each series.

The detectability of slow-to-intermediate exchange by non-equilibrium paramagnetic perturbation is related to the dimensions of the protein. The paramagnetic attenuation pattern is expected to decrease, in fact, when the distance from the surface increases and the effects of the outer sphere relaxation tend to diminish. An increase of absolute concentration of the paramagnetic probe can partially restore favorable conditions, but when the distance from the accessible surface becomes larger than some 2.5 nm or so[145], reasonable concentrations of paramagnetic probe may become ineffective. For globular proteins this scenario would arise when the molecular diameter becomes larger than 5 nm, a condition that no longer corresponds to the typically small proteins suited for NMR study. The Type II off-equilibrium deviations observed at 298 K and readily identified in Figure 3.4A, are listed in Table 3.3 and visualized in the cartoon of Figure 3A.

Table 3.3: Tempol perturbation on the NMR spectrum of 320 μM β2m at different temperatures. Off-equilibrium attenuations with Type II deviations[a].

A_N [*off-eq*] < A_N [*eq*] ≡ μs-to-ms exchange		
Structure region	*298 K*	*310 K*
N-term, strand A	**V9**, S11	**V9**, Y10
loop AB	G18	H13
strand B	N24, **C25, Y26, G29**	N21, F22, **C25, Y26**, V27, S28, **G29**
Loop BC	S33, **D34**	**D34**
strand C	**I35, E36**	**I35, E36**, V37
turn CC’, strand C’, loop C’D	G43, R45	E44, V49
strand D	**S52, S55, F56**	**H51, S52, S55, F56**
Loop DE	S61	
Strand E	**Y63, L64**, L65, E69	**Y63, L64**, Y67
Loop EF		
Strand F	**H84**	C80, **H84**
Loop FG	**L87**	**L87**
strand G, C-term	**I92**	**I92**, M99

[a]The residues whose backbone NH signals are less attenuated than the corresponding equilibrium attenuations (A_N[*off-eq*] < A_N[*eq*]), identify positions of the protein with exchange contributions to transverse relaxation. The positions that appear at both temperatures are reported in bold.

The corresponding locations are NHs of A strand and adjacent AB loop, B strand core and end, BC loop, strand C start, turn CC’ and C’ strand, disordered strand D, end of DE loop, initial fragment and end strand E, loop FG and strand G. It is worth noting that these locations, except the core of B strand and the DE loop extremity with the adjacent E strand start, correspond to backbone amides that are exposed or become accessible to the paramagnetic probe with temperature, as verified from the A_N [*eq*]-based list of Table 3.1 and the related picture of Figure 3.5. The Type II off-equilibrium deviations observed at 298 K are reported in Table 3.3 and visualized in the cartoon of Figure 3.8A. By increasing the temperature to 310 K, the distribution of the amide signals displaying decreased A_N [*off-eq*] values with respect to the equilibrium counterparts does not change substantially. Also, the close correspondence between the subset with that A_N [*off-eq*] pattern and the exposed locations tracked by Tempol is confirmed at 310 K (Table 3.1, Figure 3.5).

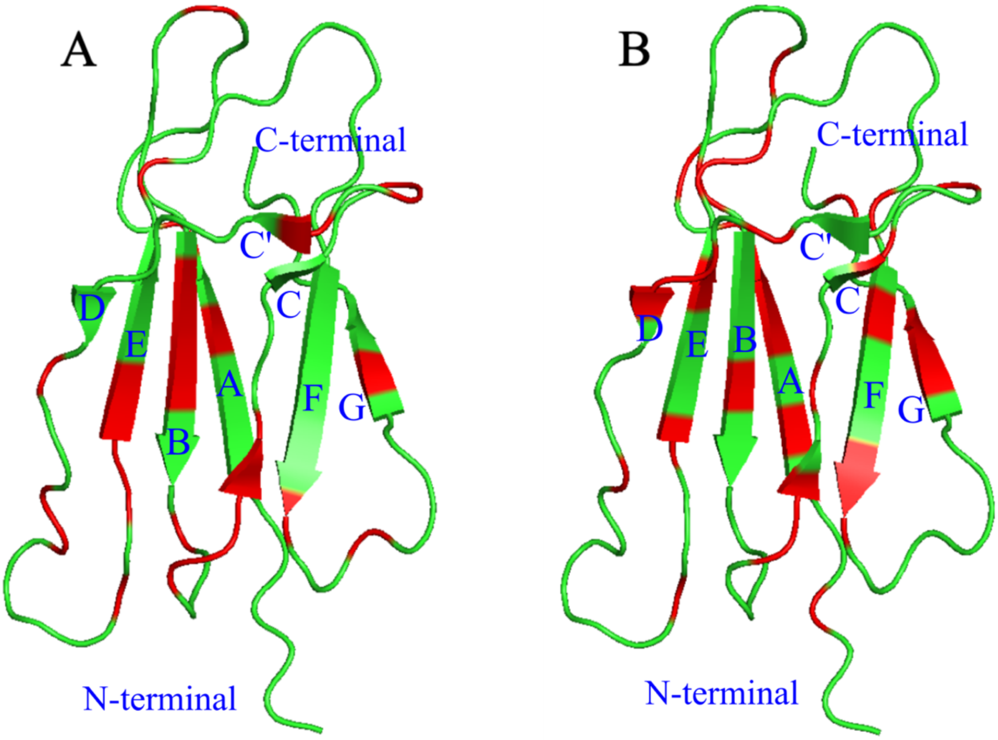

Figure 3.8: (A) Red highlighting indicates the positions of the backbone amides of β2m whose NMR signals exhibit Type II off-equilibrium deviation of normalized attenuations (A_N [*off-eq*] < A_N [*eq*]) at 298 K due to Tempol spin label (Table 3.3). (B) Red highlighting shows the location of the backbone amides of β2m exhibiting a conformational exchange contribution to ^{15}N transverse relaxation, as assessed by relaxation dispersion experiments carried out at 298 K (Table 3.4).

Besides extensions and contractions of the individual segments with decreased A_N [*off-eq*] compared to the results at lower temperature, the newly appearing Type II deviations at 310 K map to B strand, subsequent AB loop and C'D loop. The details are given again in Table 3.3 and the corresponding illustration in Figure 3.9A.

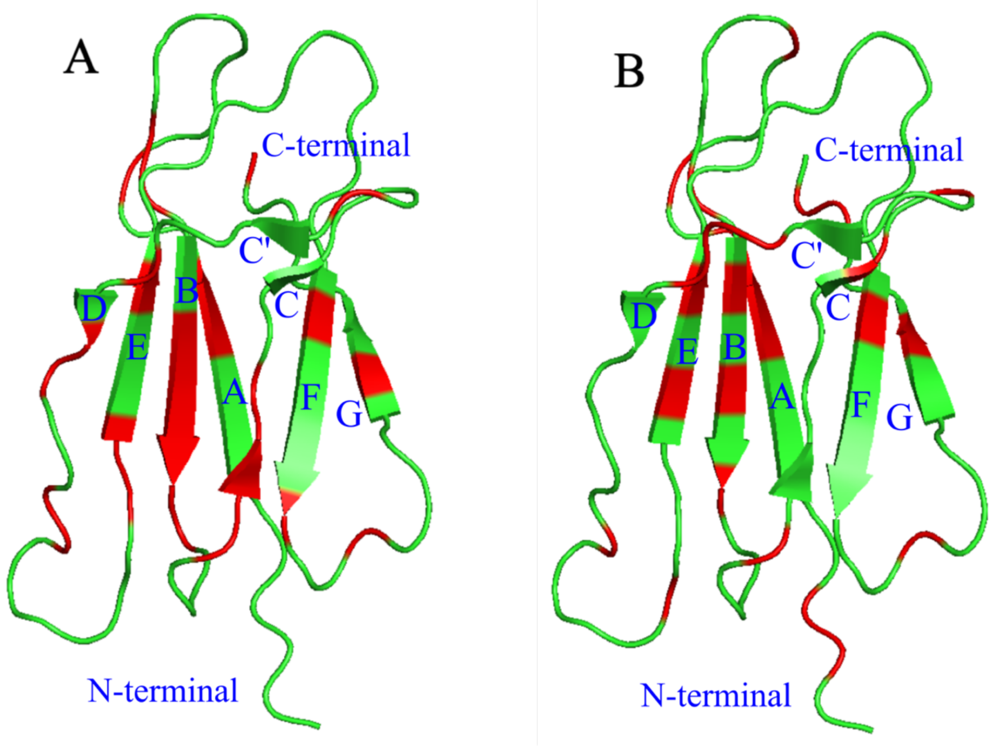

Figure 3.9: (A) Red highlighting indicates the positions of the backbone amides of β2m whose NMR signals exhibit Type II off-equilibrium deviation of normalized attenuations (A_N [*off-eq*] < A_N [*eq*]) at 310 K due to Tempol spin label (Table 3.3). (B) Red highlighting shows the location of the backbone amides of β2m exhibiting a conformational exchange contribution to ^{15}N transverse relaxation, as assessed by relaxation dispersion experiments carried out at 310 K (Table 3.4).

3.1.4 Comparing relaxation dispersion and Tempol perturbation

To validate the interpretation that attributes the reduction of the A_N [*off-eq*] values with respect to A_N [*eq*] to the effect of slow or intermediate exchange contributions on transverse relaxation, CPMG relaxation dispersion measurements[146,147] were carried out on β2m samples with analogous composition as the controls used for Tempol attenuation measurements. The CPMG relaxation dispersion experiment is ideally suited for mapping exchange processes between structural or conformational states or intermediates, even very unevenly populated, that occur over μs-to-ms time scales and affect only transverse relaxation[120,146–149]. The measurements were conducted at both 298 and 310 K and the results are reported in Table 3.4.

Table 3.4: Intermediate-to-slow (μs-to-ms) exchange processes mapped by relaxation dispersion measurements of β2m (360 μM) at different temperatures[a].

Structure region	*298 K*	*310 K*
N-term, strand A	**R3**, I7, **V9**, **Y10**, **S11**	Q2, **R3**, **V9**, **Y10**, **S11**
loop AB	**H13**, E16	***H13***, N17
strand B	***F22*, Y26**	***F22***, N24, ***Y26***, S28
Loop BC	**D34**	***D34***
strand C	I35, *V37*, ***L40***	**L40**
turn CC', strand C', loop C'D	***N42, E47*, V49**	***N42, E47***, K48, **V49**
strand D	E50, L54	F56
Loop DE	**S61**	**S61**
Strand E	L64, **Y67**, E69, F70	L65, ***Y67***
Loop EF		
Strand F	Y78, ***C80***, *N83, H84*	***C80***
Loop FG		*L87*
strand G, C-term	***I92, V93*, R97**	***V93*, R97**, *D98*

[a] The lists collect the residues whose backbone NHs present exchange contributions to T_2 assessed by relaxation dispersion. The positions that appear at both temperatures are reported in bold, whereas italic fonts indicate that the errors of the corresponding parameter from relaxation dispersion curve fitting may be large (often for the estimated chemical shift differences).

The two lists of amide signals exhibiting contributions to T_2 from μs-to-ms exchange processes include also the amides with results affected by errors comparable with the estimated parameters (exchange rates, chemical shift differences, populations). The signals whose exchange parameters exhibited fitting artefacts (unphysical zero errors) were discarded. The fittings and the corresponding parameters relative to the relaxation dispersion estimates for the amides listed in Table 3.4 are reported in Supplementary Material (Figure 3.10, Table 3.5). No major difference emerges from the comparison of the lists at different temperatures of Table 3.4, except for the extension of strand C and strand E involvement at lower temperature. However, at both temperatures, sometime the quality of the fitting documented in Figure 3.10 appears poor, in spite of the small χ^2 values that justify retaining the results. It is the case for the dispersion curves of I7, E69, I92 and V93 at 298 K, and for H13, F22, L40, K48, L87, V93, R97 and D98 at 310 K.

Table 3.5: Parameters for the fitting of the curves reported in Figure 3.10 as obtained from the dedicated routine of Dynamics Center software package (Bruker). The values of χ^2 (Pearson's χ^2 test statistic) and the related probability density function are reported for each fitted data set.

298K						
Name	***R*20 [1/s]**	**Error**	***k_{ex}* [1/s]**	**Error**	**χ^2**	**p-Values**
R3	17.86	0.79	2.46	1.18	1.13E-01	1.72E-13
I7	19.66	0.77	2.55	0.87	4.44E-01	2.10E-09
V9	16.26	0.28	2.13	0.40	3.80E-01	7.35E-10
Y10	17.46	0.40	1.95	0.54	3.66E-02	6.68E-17
S11	17.93	0.28	117	14	4.29E-01	1.68E-09
R12	19.06	0.32	112	16	1.72E-01	3.12E-12
H13	19.15	0.68	1.81	0.99	1.39E-01	7.42E-13
E16	18.23	0.38	2066	11	2.35E-01	2.76E-11
F22	15.55	0.29	2.4	11.6	4.53E-02	4.08E-16
Y26	18.78	0.36	38.0	5.7	8.79E-01	2.02E-07
D34	15.87	0.35	129	30	4.53E-02	2.99E-16
I35	15.12	0.18	1.27	0.31	9.04E-01	3.67E-14
V37	15.05	0.14	22.0	27.4	5.86E-01	1.36E-08
L40	17.44	0.27	46.8	26.9	9.2 E-02	4.15E-14
N42	16.6	0.19	25.8	22.2	1.67E-01	2.57E-12
E47	18.17	0.23	27.4	25.2	3.97E-01	9.83E-10
V49	12.76	0.14	1.32	0.20	8.53E-02	2.43E-14
E50	16.26	0.27	1.60	0.40	3.84E-01	7.84E-10
S52	17.79	0.28	13.6	21.7	2.19E-01	1.68E-11
L54	20.04	0.54	2.15	0.70	4.49E-01	2.30E-09
S61	17.21	0.71	3032	29	3.09E-01	1.78E-10
L64	17.43	0.42	4.94	1.63	4.28E-02	2.01E-16
Y67	17.24	0.23	119	30	4.20E-01	1.44E-09
E69	15.01	0.17	2907	4	4.10E-01	1.22E-09
F70	17.17	0.25	1237	8	4.21E-01	1.49E-09
Y78	16.56	0.23	324	24	3.36E-02	3.72E-17
C80	17.12	0.21	51.0	27.2	1.23E-01	3.20E-13
N83	17.14	0.23	41.2	29.4	1.40E-01	7.69E-13
H84	15.64	0.20	2512	21	1.12E-01	1.58E-13
V85	19.59	0.26	0.70	27	7.05E-01	4.74E-08
I92	16.17	0.21	729	17	6.42E-01	2.53E-08
V93	17.44	0.26	6.4	22.0	4.89E-01	4.06E-09
R97	15.54	0.28	1.68	0.38	8.27E-02	1.97E-14
310K						
Name	***R*20 [1/s]**	**Error**	***k_{ex}* 1/s]**	**Error**	**χ^2**	**p-Values**
Q2	18.26	0.12	1.53	0.17	8.40E-02	2.20E-14
R3	15.3	0.08	123	10	1.44E-01	9.18E-13
V9	12.31	0.09	0.94	0.18	1.82E-01	4.69E-12
Y10	12.53	0.11	0.91	0.24	7.78E-02	1.29E-14
S11	13.22	0.05	29.7	25.7	1.79E-01	4.17E-12
H13	14.9	0.05	4.4	31.5	1.02E-01	8.51E-14

N17	23.52	0.20	45.7	25.1	2.29E-01	2.29E-11
F22	11.31	0.04	16.2	30.0	5.80E-02	1.66E-15
N24	13.23	0.05	24.8	17.0	2.12E-01	1.32E-11
Y26	13.72	0.06	21.4	23.0	4.79E-01	3.55E-09
S28	13.45	0.05	0.80	0.33	2.93E-01	1.25E-10
D34	11.33	0.04	1.91	6.68	5.88E-02	1.83E-15
L40	12.75	0.05	0.59	0.25	7.65E-02	1.15E-14
N42	12.01	0.03	14.7	25.7	1.82E-01	4.76E-12
E47	17.33	0.07	17.0	15.0	4.15E-01	1.34E-09
K48	14.64	0.05	0.57	0.38	6.02E-02	2.15E-15
V49	10.15	0.02	23.6	18.6	1.13E-01	1.70E-13
S52	13.12	0.04	17.2	28.3	2.35E-01	2.72E-11
F56	14.02	0.15	0.87	0.39	5.57E-02	1.25E-15
S61	12.57	0.10	7522	1	2.18E-01	1.62E-11
Y63	24.1	0.15	15.5	18.2	5.48E-01	8.70E-09
L65	15.4	0.08	1.77	0.13	1.72E-01	3.11E-12
Y67	12.42	0.03	28.6	26.5	2.21E-01	1.79E-11
C80	12.5	0.03	17.8	24.1	9.37E-02	4.70E-14
L87	11.42	0.03	17.6	23.4	2.08E-01	1.18E-11
I92	11.78	0.03	0.4	17.1	7.13E-01	5.06E-08
V93	12.19	0.04	21.4	20.1	6.11E-01	1.81E-08
R97	13.36	0.04	0.60	0.24	1.11E-01	1.49E-13
D98	10.29	0.02	35.9	40.6	1.09E-01	1.38E-13

A

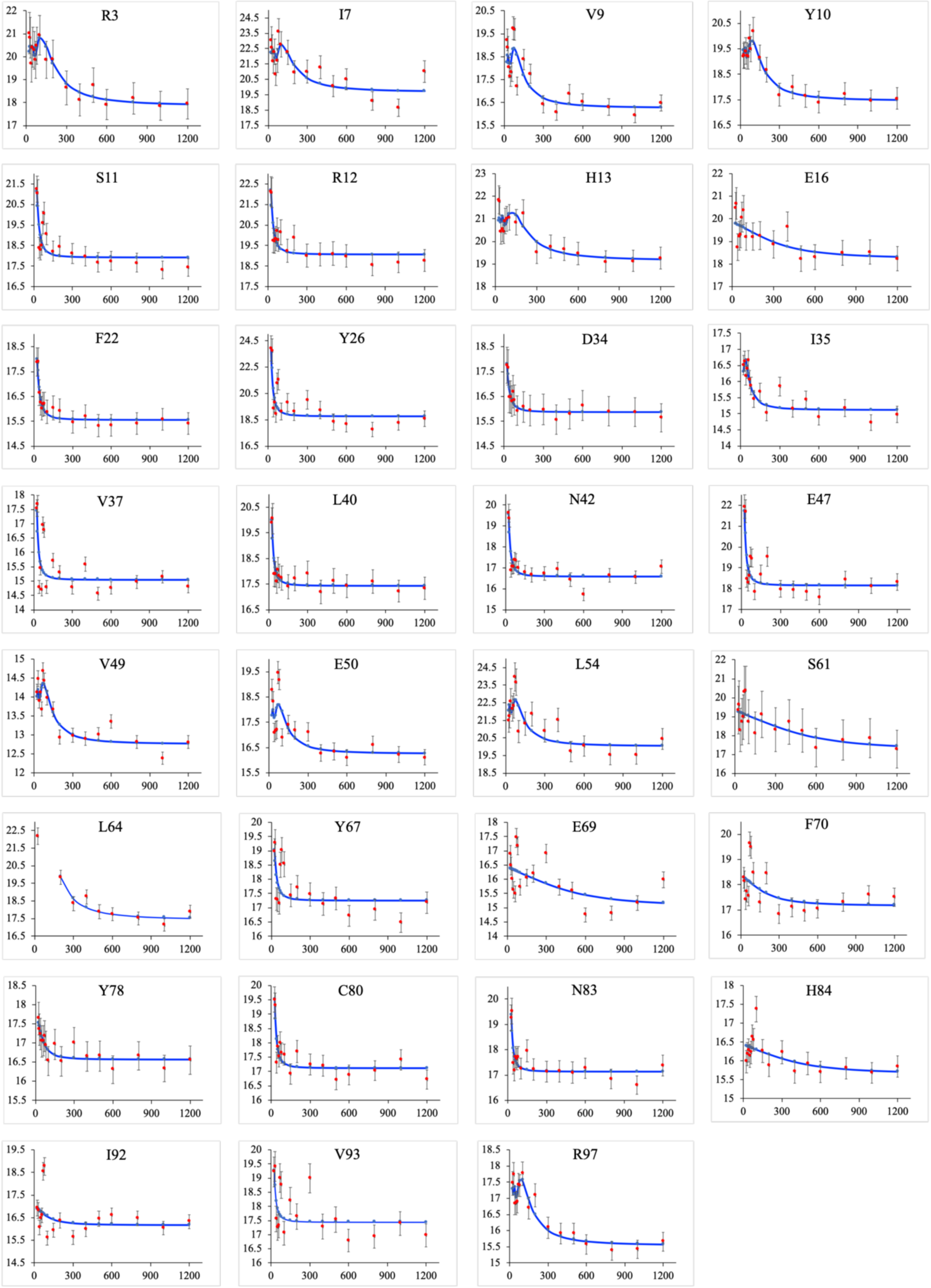
R3
22 21 20 19 18 17
0 300 600 900 1200
I7
24.5 23.5 22.5 21.5 20.5 19.5 18.5 17.5
0 300 600 900 1200
V9
20.5 19.5 18.5 17.5 16.5 15.5
0 300 600 900 1200
Y10
20.5 19.5 18.5 17.5 16.5
0 300 600 900 1200
S11
21.5 20.5 19.5 18.5 17.5 16.5
0 300 600 900 1200
R12
22.5 21.5 20.5 19.5 18.5 17.5
0 300 600 900 1200
H13
23 22 21 20 19 18
0 300 600 900 1200
E16
22 21 20 19 18 17
0 300 600 900 1200
F22
18.5 17.5 16.5 15.5 14.5
0 300 600 900 1200
Y26
24.5 22.5 20.5 18.5 16.5
0 300 600 900 1200
D34
18.5 17.5 16.5 15.5 14.5
0 300 600 900 1200
I35
17.5 17 16.5 16 15.5 15 14.5 14
0 300 600 900 1200
V37
18 17.5 17 16.5 16 15.5 15 14.5 14
0 300 600 900 1200
L40
20.5 19.5 18.5 17.5 16.5
0 300 600 900 1200
N42
20 19 18 17 16 15
0 300 600 900 1200
E47
22 21 20 19 18 17
0 300 600 900 1200
V49
15 14.5 14 13.5 13 12.5 12
0 300 600 900 1200
E50
19.5 18.5 17.5 16.5 15.5
0 300 600 900 1200
L54
24.5 23.5 22.5 21.5 20.5 19.5 18.5
0 300 600 900 1200
S61
22 21 20 19 18 17 16
0 300 600 900 1200
L64
22.5 21.5 20.5 19.5 18.5 17.5 16.5
0 300 600 900 1200
Y67
20 19.5 19 18.5 18 17.5 17 16.5 16
0 300 600 900 1200
E69
18 17.5 17 16.5 16 15.5 15 14.5 14
0 300 600 900 1200
F70
20 19 18 17 16
0 300 600 900 1200
Y78
18.5 18 17.5 17 16.5 16 15.5
0 300 600 900 1200
C80
20 19.5 19 18.5 18 17.5 17 16.5 16
0 300 600 900 1200
N83
20 19 18 17 16
0 300 600 900 1200
H84
18 17.5 17 16.5 16 15.5 15
0 300 600 900 1200
I92
19.5 18.5 17.5 16.5 15.5 14.5
0 300 600 900 1200
V93
20 19.5 19 18.5 18 17.5 17 16.5 16
0 300 600 900 1200
R97
18.5 18 17.5 17 16.5 16 15.5 15
0 300 600 900 1200

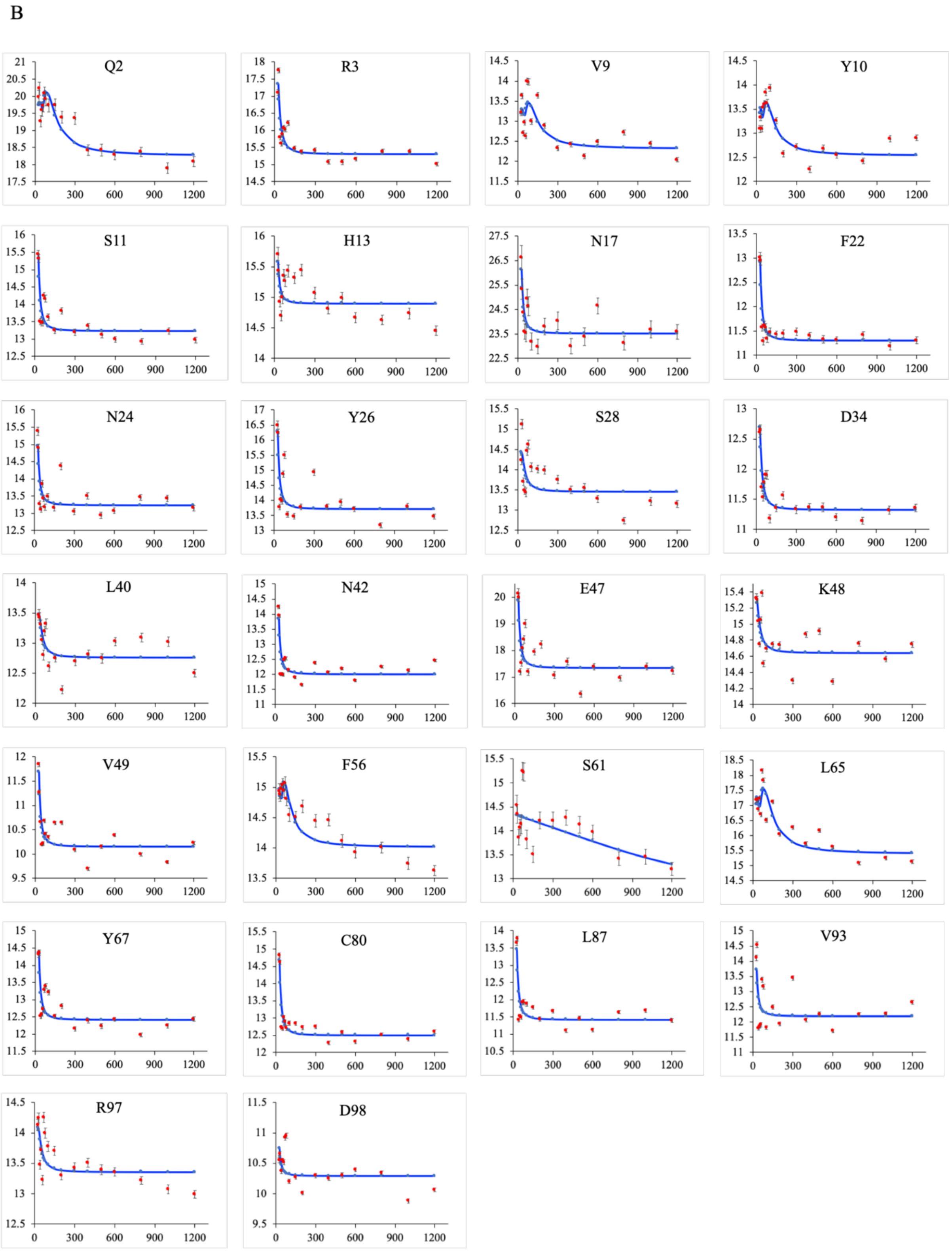

Figure 3.10: Fitting (blue curve) of 360 μM β2m relaxation dispersion data. The plots report the transverse relaxation rate (s^{-1}) as a function of the 180o pulse spacing (s^{-1}). (A) 298 K; (B) 310 K. The experimental data points (red circles) are reported with the corresponding error bars.

Albeit statistically acceptable, these unsatisfactory curves and the accompanying large errors on the fitted parameters (or even their experimental plausibility) reflect the current limits of CPMG relaxation dispersion measurements, quite critical at concentrations below 1 mM at 600 MHz. Although the reliability of the trend for the vast majority of the non-flat dispersions above listed is ensured by the observed $T_{1\rho}$ change with the spin-lock field strength (Table 3.6), the results with critical fitting among those listed in Table 3.4 were also retained based on the evidence from other studies.

Table 3.6: Selected ^{15}N NMR $T_{1\rho}$ values at different spin-lock field strengths of 320 µM β2m measured at 60.82 MHz (15N frequency) and 298 K.

Residue	$T_{1\rho}$ [ms] SL=3.00 kHz	$T_{1\rho}$ [ms] SL=1.67 kHz
Q2	94±5	84±3
I7	91±5	83±3
H13	76±2	64±3
F22	91±3	74±3
Y26	86±4	75±6
G29	95±19	82±23
D34	78±10	65±2
E36	96±7	88±5
L40	85±2	76±2
N42	95±7	90±3
K48	87±3	75±3
S55	74±4	53±5
F56	80±3	59±3
D59	68±1	53±5
S61	90±5	85±10
L64	84±5	65±11
E69	95±8	83±4
C80	86±3	73±5
L87	81±2	79±2
V93	94±9	81±3
K94	90±5	85±8
D96	87±6	84±7
R97	96±5	90±5
D98	119±5	94±5

The amide sites of the residues reported in Table 3.4, in fact, reasonably match those of previous relaxation dispersion studies conducted in solid state, at 283 K on wild type β2m[30], and liquid state, at 288 K on the mutant W60G β2m[150]. The involvement of the N-terminal segment, the strands A, B, D, E and the loops CD and FG appears in our list and in both the previous studies. It should be pointed out, however, that the liquid state study addressed only the intermediate excited state (*I*) of W60G β2m that is observable during the refolding process leading to the native (*N*) species[150]. Measuring during refolding poses limits to the detectability of a number of signals due to excessive broadening. For instance the amides of the BC loop, surely involved in the transition *I*→*N*, are too broad and therefore are not present among the 11 NHs of *I* state that exhibit exchange contributions to transverse relaxation as a consequence of either the conversion into *N* or the *I* dimerization[150]. Conversely, the solid state results include, among the ~40 NHs with non-flat dispersion[30], all the residues of BC loop (except P32 that lacks NH) due to the slowdown of the interconversion between *N* and *I* in the absence of liquid solvent, and 5 sites of Table 3.4 with imperfect fitting (I7, H13, F22, E69, L87). For the other NHs with imperfect fitting, solid state relaxation rates could not be measured in 3 cases (K48, R97 and D98) while for the remaining 2 location (L40, and V93) solid state data present flat dispersion[30]. Interestingly, our results of Table 3.4 include always at least one residue of the BC loop (D34) and only at 310 K the end of strand B (S28), much like the off-equilibrium attenuations of Table 3.3 that include B strand extremity and BC loop residues (G29, S33 and D34 at 298K and S28, G29 and D34 at 310K). In analogy with the interpretation of liquid state results[150], the positions of the intermediate-to-slow exchange processes observed in the present study (Table 3.4) must represent locations involved in the interconversion between native and intermediate species as well as in association (dimerization and higher oligomerization[151]). The data of Table 3.4 are graphically presented in the cartoons of Figures 3.8B (298 K) and 3.9B (310 K) that can be readily compared with the corresponding structures of Figures 3.8A and 3.9A highlighting the positions of the amides showing Type II deviation of A_N [*off-eq*] values, at 298 K and 310 K, respectively. The correspondence is rather satisfactory at both temperatures. In particular, out of the 24 backbone amides showing a decreased A_N [*off-eq*] with respect to A_N [*eq*] at 298 K (Table 3.3), a µs-to-ms exchange process is estimated to accelerate transverse relaxation in 10 cases (Table 3.4), whereas for other 7 NHs, the adjacent residue amide occurs among those mapped by relaxation dispersion analysis. This can be appreciated by comparing the distribution of the red-highlighted regions in the two panels of Figure 3.8. Similarly, at 310 K, out of the 28 NH resonances with Type II deviation of A_N [*off-eq*] values (Table 3.3), 12 exhibit the contribution of intermediate-to-slow exchange on transverse relaxation (Table 3.4), while a similar contribution also shortens the T_2 of amides belonging to the adjacent residues of 9 other NHs of the 310 K pool in Table 3.3. Hence, a rather stringent correlation emerges with the occurrence of µs-to-ms local conformational dynamics for 17 and 21 NHs of β2m, at 298 K and 310 K, respectively, out of 24 and 28 that display the pattern A_N [*off-eq*] < A_N [*eq*] (Table 3.3) at the same temperatures. The comparison of the data of Tables 3.3 and 3.4 shows however that the overlap is only partial, i.e. there are locations occurring in Table 3.4 but missing in Table 3.3, and *vice versa*. The first type of discrepancy can be explained as the consequence of a quite fast recovery induced by the paramagnetic perturbation that requires very short relaxation delays to stand out in the ι_p^k value employed to calculate A_N [*off-eq*]. This can be seen in Figure 3.11, where the data obtained with a relaxation delay of 0.2 s are reported.

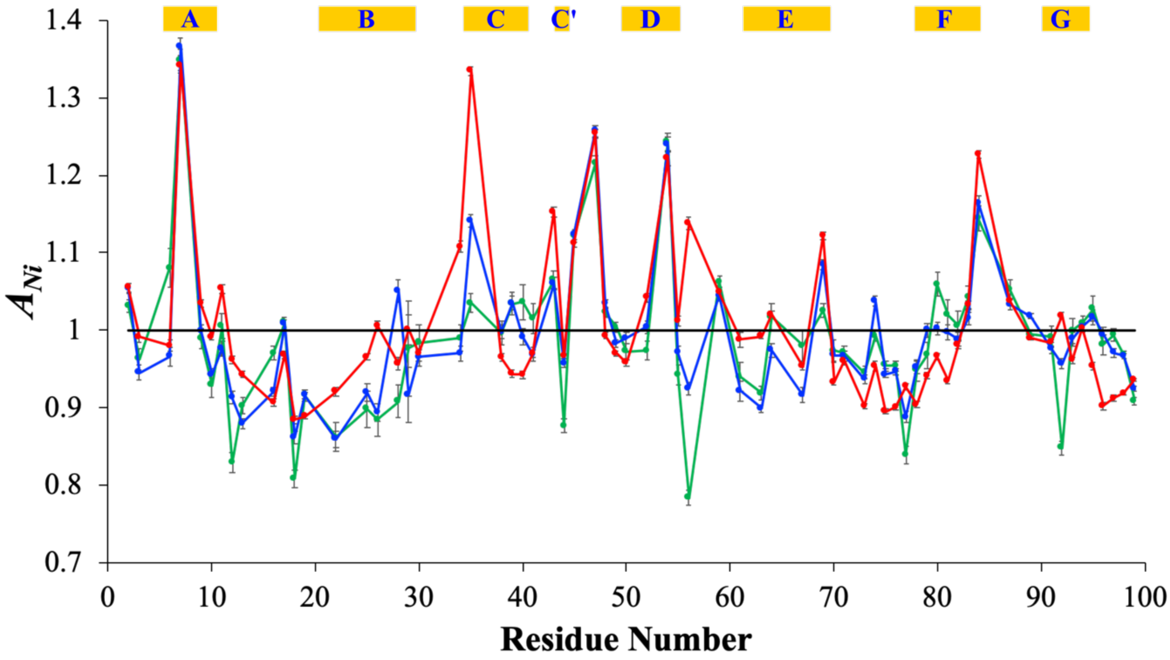

Figure 3.11: Overlay of the A_N values obtained from ^{1}H-^{15}N HSQC spectra of 320 µM β2m in the presence of 1.6 mM Tempol at 298 K, with relaxation delay of 0.2 s (green), 0.5 s (blue) and 4 s (red). The β-strand location and naming along the sequence is reported with yellow strips. The β-strand location and naming along the sequence is reported with yellow strips.

With faster recycling, Q2 and R3 clearly show the A_N [*off-eq*] pattern diagnostic for exchange occurrence, confirmed by relaxation dispersion (R3, Table 3.4) and $T_{1\rho}$ (Q2, Table 3.6) evidence. As mentioned in the Experimental section, however, the relaxation delay value of 0.5 s was selected to preserve a good signal-to-noise ratio. On the other hand, the presence of some locations only in Table 3.3 and not in Table 3.4 can be explained by the low sample concentration that affects more the relaxation dispersion data than the paramagnetic attenuation ones. Overall however, the described approach enables one to link the off-equilibrium paramagnetic attenuation pattern with very valuable information that can be otherwise quantified only through relaxation dispersion experiments. Therefore, it is possible to run preliminary paramagnetic perturbation experiments with non-specific nitroxides such as Tempol to map plausible regions of intermediate-to-slow conformational dynamics or association exchange. The advantage is that measuring signal intensities of HSQC spectra is by far easier and quicker than relaxation dispersion experiments. Reliable intensity quantitation is possible also with diluted samples, whereas a relaxation dispersion study requires relatively concentrated samples and often measurements at different fields to extract confidently the parameters of a demanding fitting[152]. Indeed, already with a 0.36 mM sample of β2m, i.e. close to the solubility limit of the protein, estimating the parameters from relaxation dispersion experiments was quite critical. Moreover relaxation dispersion measurements may become simply not viable with systems undergoing changes within a few hours from preparation, unless the sophisticated real-time Best-TROSY CPMG relaxation dispersion approach[150] is employed, always when sensitivity is sufficient.

3.1.5 Diluted sample control

A 50 µM β2m sample prepared in the same buffer as used with the more concentrated samples was analyzed with the methodology above described, i.e. with and without 250 µM Tempol spin label, under equilibrium and off-equilibrium conditions. The data were collected at 298 K only. Due to the low concentration, relaxation dispersion measurements were not viable with the available instrumentation to extract, confidently and within reasonable acquisition times, reliable information. So, the analysis could only be carried out using the paramagnetic attenuation patterns. Figure 3.12 reports the overlay of the A_N values from the ^{15}N-^{1}H HSQC spectra collected with 0.5 or 4 s relaxation delay. The amplitude spanned by the A_N values at 50 µM is definitely reduced with respect to the data obtained at higher concentration (Figure 3.4). However, the general features of surface accessibility from A_N [*eq*] levels observed at 50 µM confirm essentially the results obtained at higher concentration, with slight exposure gains at N-terminus, C-terminus, C'D, EF and FG loops and slight losses at loop BC and strands C and D (compare Figures 3.12A and 3.4A).

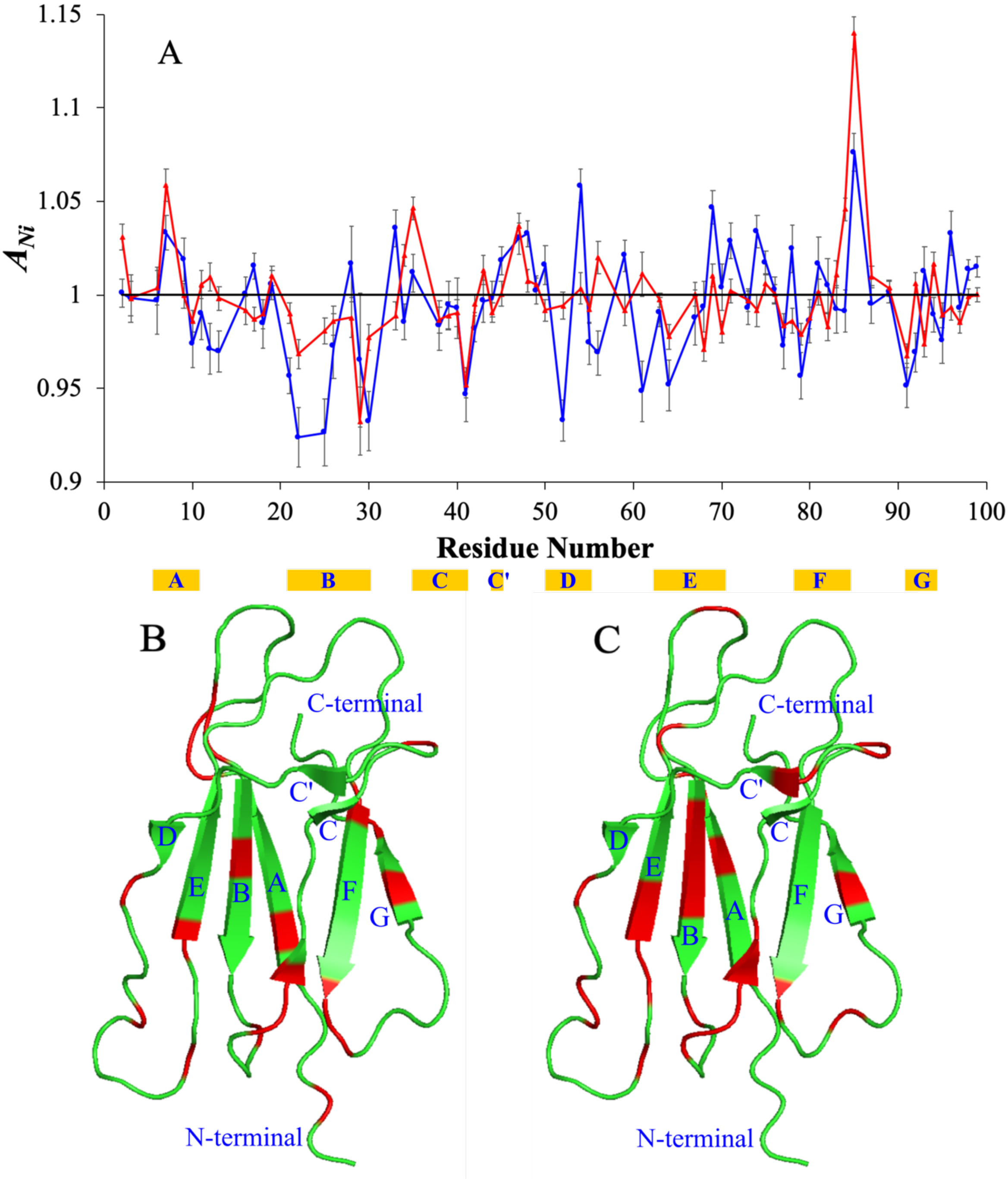

Figure 3.12: (A) Overlay of the A_N values obtained from ^{1}H-^{15}N HSQC spectra of 50 μM β2m in presence of 250 μM Tempol, acquired at 298 K with relaxation delay of 0.5 s (blue) or 4 s (red). In the subsequent panels, β2m cartoons are reported where red highlighting indicates the positions of the backbone amides whose NMR signals exhibit Type II off-equilibrium deviations of normalized attenuations (A_N [*off-eq*] < A_N [*eq*]) at 298 K and concentration of 50 μM (B) or 320 μM (C).

Table 3.7: Tempol perturbation on the NMR spectrum of 50 μM β2m at 298 K. Equilibrium (left) and off-equilibrium (right)[a].

Structure region	**A_N [*eq*] > 1**	**A_N [*off-eq*] < A_N [*eq*]**
N-term, strand A	Q2, **I7**	Q2, I7
loop AB	R12, K19	R12, H13
strand B		N21, F22, **C25**, F30
Loop BC	**D34**	**D34**
strand C	**I35**	**I35**
turn CC', strand C', loop C'D	**G43, E47**, K48, V49	**N42**
strand D	**F56**	**S52, F56**
Loop DE		**S61**
Strand E	**E69**	**L64**
Loop EF	K75	
Strand F	**N83, H84**	A79, **H84**
Loop FG	**V85**, L87	V85
strand G, C-term	K94	**I92**, K94

[a] The residues with backbone NH signals presenting A_N [*eq*] > 1, define exposed positions of the protein, if no specific interaction occurs with the spin label. The residues with backbone NH signals presenting A_N [*off-eq*] < A_N [*eq*], identify positions of the protein with exchange contributions to transverse relaxation. The positions that appear also in the corresponding data obtained with 320 μM β2m (Table 3.1 and Table 3.3) are reported in bold.

Even more significantly, the Type II deviations of A_N [*off-eq*] values at 50 μM reproduce in practice the same pattern as observed at higher concentration, with some different involvement at the N-terminal region. This is pictorially demonstrated by the comparison of panels B and C of Figure 3.12 that portray the cartoons of β2m solution structure highlighting the locations where A_N [*off-eq*] < A_N [*eq*], respectively at 50 μM and 320 μM. The corresponding details for the low concentration sample, in terms of involved residues, are listed in Table 3.7, and can be compared to the 320 μM data at 298 K of Table 3.3 (and Table 3.1 for surface accessibility). Beyond the changes in some sequence segments, the correspondence, at both concentrations, of the regions with decreased A_N [*off-eq*] values, compared to equilibrium levels, suggests the invariance of the local conformational exchange for the investigated conditions, if the pattern A_N [*off-eq*] < A_N [*eq*] is assumed to reveal the occurrence of intermediate-to-slow exchange contributions to transverse relaxation. Since this type of contributions to transverse relaxation may also arise from association processes[150], variations observed at lower protein concentrations, such as those reported for β2m in Table 3.7 with respect to the data of Tables 3.3 and 3.1, may in principle map the association interface.

3.1.6 Lysozyme measurements

In order to check the applicability of the off-equilibrium paramagnetic attenuations to recognize the occurrence of exchange processes affecting transverse relaxation and originating from conformational or structural interconversion, including labile association events, unlabeled hen egg white lysozyme (HEWL) was considered for two reasons. First, previous work[133] had shown that Tempol spin label can be safely and successfully employed with HEWL to map surface exposure as no major interaction takes place between the probe and the protein leading to a stable complex under proper experimental conditions. Second, HEWL is known to form dimers and even trimers, especially at high pH and ionic strength[55,56,59,153], with association essentially governed by electrostatic and polar interactions. Under our experimental conditions (pH = 3.9, 50 mM glycine buffer and 1 mM concentration), the overall charge of HEWL is sufficiently high to limit dimerization[55,56,153] so that only labile adducts or encounter complexes are formed such as those obtained by Ermakova by Brownian dynamics simulations[59]. Proton 2D TOCSY spectra of HEWL were thus recorded without and with 5 mM Tempol, with relaxation delays of 5 s and 0.5 s, and the equilibrium and off-equilibrium A_N values were calculated from the resolved cross-peaks of the fingerprint region, i.e. the intra-residue H^N-H^α connectivities. The paramagnetic attenuation information provided by this type of cross-peaks concerns of course two protein-backbone-bound vicinal hydrogens and is therefore different with respect to the accessibility inferences obtained from the ^{15}N-^{1}H correlations of HSQC spectra. The latter ones reflect essentially only the amide hydrogen characteristics, due to the overwhelming difference of gyromagnetic ratio between the involved nuclei, whereas, for the homonuclear proton cross-peaks, attenuations report cumulatively the exposure of both nuclei, without any scaling other than the individual relaxation rates[114,133,136].

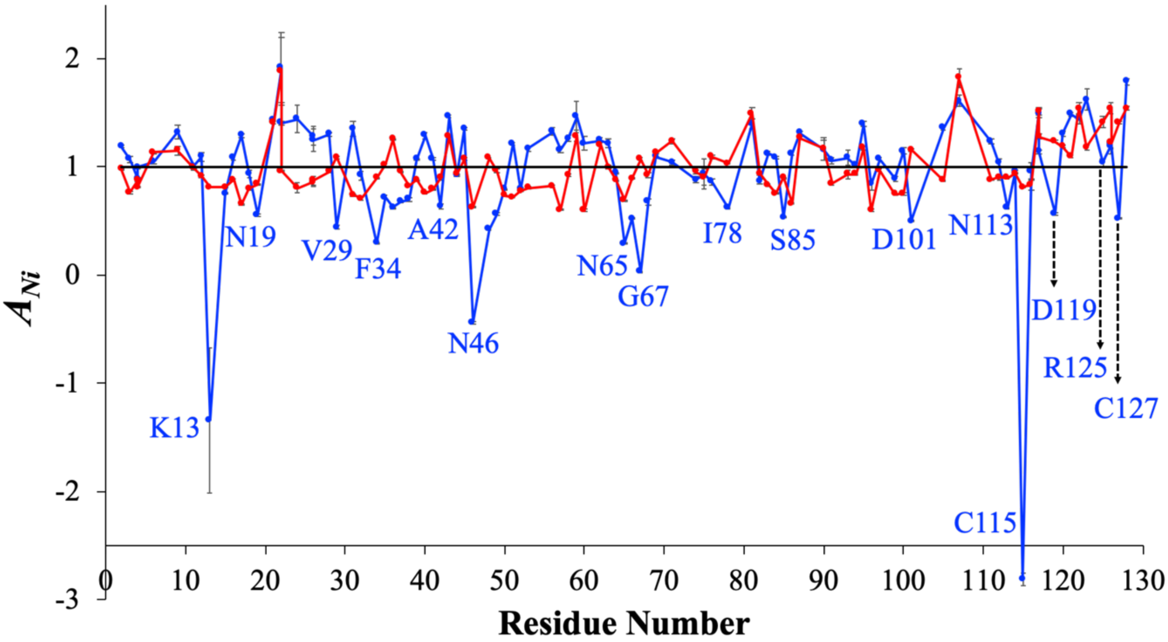

Figure 3.13: Overlay of the A_N values obtained from H^N-H^α cross-peaks of ^{1}H-TOCSY spectra of 1 mM HEWL at 313 K, acquired with relaxation delay of 0.5 s (blue) or 5 s (red), in presence and absence of 5 mM Tempol. To avoid graphical crowding, only the local minima of A_N [*off-eq*] values are marked.

It is worth reminding that our analysis is restricted to backbone nuclei that represent a homogeneous subset in structured proteins from the viewpoint of the overall tumbling rate, devoid of the complications that can be incurred with side chain nuclei, where the paramagnetic perturbation is primarily modulated by the specific local mobility[112,114,133–136]. Hence homonuclear TOCSY H^N-H^α cross-peaks can be interrogated on the intervening relaxation processes by studying equilibrium and off equilibrium attenuations, as here described. The results are plotted in Figure 3.13. We will not discuss the details of the equilibrium attenuations and the Type I deviation of the off-equilibrium ones (A_N [*off-eq*] > A_N [*eq*]), as the assessment of surface accessibility of HEWL and other proteins by Tempol is already described elsewhere[114,133,135,136]. We only focus on the Type II deviations of off-equilibrium attenuations. The pattern A_N [*off-eq*] < A_N [*eq*] is clearly observed in Figure 3.13 in correspondence of 16 downward peaks that are annotated in the plot for sake of clarity. In addition, the same Type II deviation pattern appears at some flanking positions, namely at D66, R68 and in the tracts E35-N37 and D48-G49. All the marked locations in Figure 3.13, except V29, I78 and S85, match the intermolecular interaction sites predicted by Brownian dynamics[59]. From the structural examination of the simulation results in fact, two classes of encounter complexes were recognized entailing intermolecular salt-bridges, H-bonds and polar interactions. Considering the relative orientation of the single protein molecules in the encounter complexes, most of the interactions making up the dimeric interfaces of both classes were estimated to plausibly form among the unit cell monomers of the different crystal structures available for HEWL. For several of these interactions, dynamics simulations could calculate the occurrence probability and the kinetic constant[59]. The residues with the highest contact numbers were K13, K33, E35, D48, D52, R61, R73, D101, R112, K116, D119, R125, R128, but also N19, N27, T43, N44, R45, W62, D66, R68, E121, L129 had significant roles in interfaces. The very high frequency of positively and negatively charged residues, i.e. K, R, D and E, reflects clearly the prevailing character of the interactions. Most significantly with respect to the data of Figure 3.13, five dimerization contact locations (K13, N19, D101, D119 and R125) coincide with low attenuation peaks and three locations (E35, D66 and R68) are found in the peak flanking regions. Considering the peaks at F34, N65 and G67 (Figure 3.13) with respect to E35, D66 and R68 involvement in the dimeric interfaces, it does not appear an additional mere coincidence that five other peaks of Figure 3.13 (A42, N46, N113, C115 and C127) precede or follow one of the interaction site sampled by dynamics (T43, R45, R112, K116, R128). An intermolecular encounter may imply an extended accessibility reduction at the interaction site(s) and simultaneously determine an exchange of chemical environment also at a neighboring site such as the preceding or following residue H^N and/or H^α. The correlation of the affected H^N-H^α pair would therefore report the exchange in terms of enhanced transverse relaxation rate, i.e. Type II deviation of A_N [*off-eq*] value. This mechanism may well apply also to the peaks at V29, I78 and S85 reporting the further apart interactions at N27, N74 and D87, respectively. Overall then, out of 16 peaks with reduced A_N [*off-eq*] compared to A_N [*eq*] shown by HEWL attenuation data in Figure 3.13, 13 can be accounted by transverse relaxation rate increases due to association exchange at locations that are either directly involved or adjacent to directly involved sites of the dimerization interfaces. For the remaining 3 peaks of Figure 3.13, an exchange involving positions 2 or 3 residues far apart from the dimerization sites can be invoked. Therefore, the Type II deviations of A_N [*off-eq*] values in HEWL proton TOCSY data reveal a strict correlation with the exchange events at the dimerization interfaces through the additional contribution to transverse relaxation introduced by the same exchange events. Consistently, the predicted kinetic constants for several HEWL dimerization sites[59] fell in the range $2 - 92\times10^6$ $M^{-1}s^{-1}$, i.e. intermolecular interactions occurring on the μs time scale that are capable of affecting transverse relaxation. In addition to Brownian dynamics simulation, the attenuation data of Figure 3.13 also agree with the results of a ^{15}N relaxation study of 4 mM

HEWL carried out at 308 K and pH 3.8[44]. For all the locations exhibiting A_N [*off-eq*] minima in Figure 3.13, exchange contributions to transverse relaxation were measured at the same or adjacent position, except for N19, I78, D101 and R125 H^N-H^α, that however could be reporting the processes that occur at neighboring residues, i.e. G22, S81, M105 and R128 where the slow exchange signature on the relaxation rates was ascertained[44].

3.1.7 Concluding remarks

The use of extrinsic spin labels in protein NMR studies has long been shown to be related to surface accessibility. This information is valuable especially when accessibility patterns are comparatively considered with respect to different experimental conditions. Here we have drawn the attention on the effects of fast recycling on protein NMR spectra perturbed by Tempol, a water-soluble nitroxide lacking specific interactions with the tested proteins. The corresponding paramagnetic perturbation profiles obtained from the signal intensities of backbone nuclei have shown an interesting correlation with the occurrence of exchange processes due to conformational or interaction/association dynamics with μs–ms time scale, besides confirming the surface accessibility assessment. Thus, the information from paramagnetic perturbation of NMR spectra, collected in the absence of specific interactions of the paramagnetic probe and far from magnetization equilibrium conditions, becomes very valuable and may represent a powerful and convenient preliminary control to map structural or functional dynamics in the typically small proteins amenable to high resolution NMR characterization. Transverse relaxation dispersion measurements can be subsequently carried out to investigate the quantitative aspects of the exchange when sensitivity and acquisition times are not an issue.

3.2 Insights into a protein-nanoparticle system by paramagnetic perturbation NMR spectroscopy

Using extrinsic spin labels such as nitroxides to extract structural information requires testing the reliability of their non-specific probe behavior[114,133,135,136]. ESR spectra of Tempol in the absence and presence of β2m had previously shown that only statistical encounters occur between the free radical and the protein, as inferred from the invariance of linewidths and amplitudes of the superimposed spectra[154]. For the ternary system protein+AuNPs+Tempol, the ESR trace superposition for the three controls (Tempol, Tempol+AuNPs and Tempol+β2m) and the ternary system shows substantial coincidence with some small amplitude deviations (Figure 3.14).

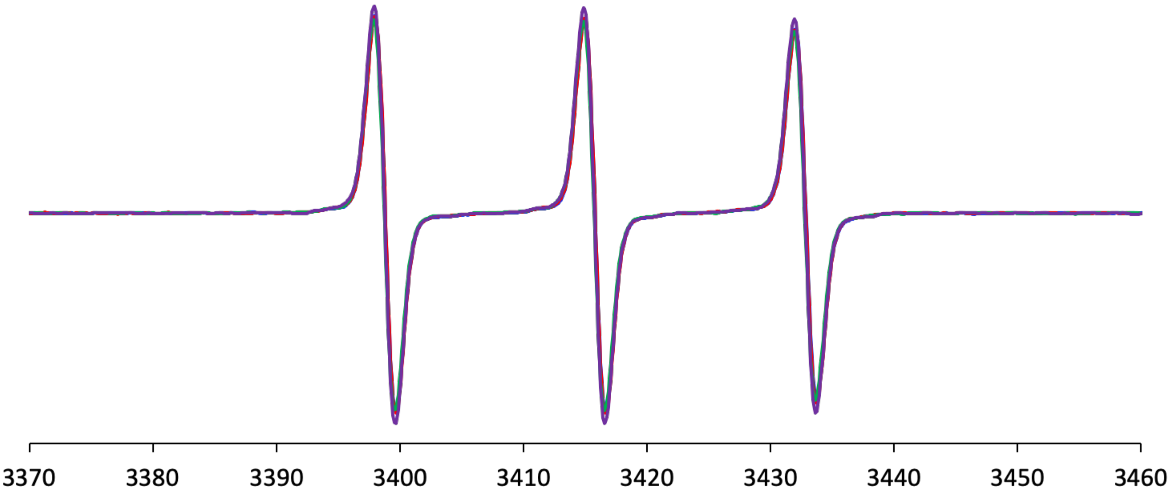

Figure 3.14. Superposition of the ESR spectra of 0.8 mM Tempol (blue), 0.8 mM Tempol + 8 µM β2m (red), 0.8 mM Tempol + 60 nM AuNPs (green) and 0.8 mM Tempol + 8 µM β2m + 60 nM AuNPs (purple). All solutions were prepared in 20 mM Hepes at pH 7. For the samples without AuNPs, 1.5 mM sodium citrate (already present in the AuNPs preparations) was added to the solvent. The spectra were recorded at 298 K. The barely detected amplitude differences are consistent with rotational correlation times with differences within the experimental error (see Table 3.8).

The degree of meaningfulness of these deviations was assessed by calculating the rotational correlation time (τ_c) of the nitroxide in the different tested conditions, according to Eqs. 30 and 31 (see Materials and Methods). Table 3.8 lists the corresponding values. Under any tested condition, the Tempol τ_c value remains around an average of 31.6 ps (the standard deviation is 1.3 ps) which indicates that, within the experimental error, no detectable effect arises from β2m, or AuNPs, or both on the tumbling rate of the free radical. On the other hand, that average τ_c value is consistent with those reported for 2 mM Tempo (91.9 ps) and Tempone (14.9 ps) in water at 300 K[155]. Therefore, the occurrence of Tempol interactions other than the statistical collision in the binary and ternary systems here considered should be ruled out.

Table 3.8: Rotational correlation time ($\tau_c/10^{-11}$ s) of Tempol at the indicated concentrations and different solution compositions obtained from ESR measurements at 298 K.

Composition	***Tempol***	***Tempol+AuNPs***	***Tempol*+ β2m**	***Tempol+AuNPs*+ β2m**
[Tempol]		[AuNP]=60nM	[β2m]=8μM	[AuNP]=60nM; [β2m]=8μM
1.6mM	3.3 ± 0.2	3.1± 0.2	3.4 ± 0.2	3.3 ± 0.2
0.8mM	3.2 ± 0.2	3.0 ± 0.3	3.2 ± 0.3	2.9 ± 0.2
0.4mM	3.1 ± 0.3	3.2 ± 0.3	3.1± 0.3	3.1± 0.4

Figure 3.15 shows the pattern of the normalized attenuation (A_N) values observed with 8 μM β2m and 0.8 mM Tempol with respect to the same protein solution without the nitroxide. The graph depicts in red the backbone amide signal A_N values extracted from data collected under magnetization equilibrium conditions (A_N[eq]), and in blue the analogous A_N values extracted from data collected under magnetization off-equilibrium conditions (A_N[off-eq]), respectively obtained from pairs of ^{15}N-^{1}H HSQC spectra with relaxation delays of 5 s and 0.5 s. According to our previous interpretation[114,133,154], A_N[eq] values larger or smaller than unity indicate amide signals attenuated above or below the average attenuation, respectively, and therefore identify molecular locations more or less accessible to the nitroxide probe, depending on the specific surface exposure. The interpretation of the A_N[off-eq] values is related, instead, to their relationship with the corresponding A_N[eq] figures[154]. In particular, the pattern A_N[off-eq] > A_N[eq] identifies amide positions with either locally hindered accessibility on the molecular surface or true structurally buried positions. As such, this pattern, that was named Type I deviation of A_N[off-eq], is typically, though not exclusively, associated with A_N[eq] < 1, i.e. locations with accessibility lower than average[154]. In fact when Type I deviation occurs at exposed locations, the corresponding A_N[eq] value is only slightly larger than unity. On the other hand, the pattern A_N[off-eq] < A_N[eq], named Type II deviation of A_N[off-eq], identifies those amide positions whose recovery is faster than the average off-equilibrium signal recovery, thereby proving less attenuated than that average. In the absence of specific interactions of the spin probe with the protein and/or structural transitions of the latter induced by the former, as verifiable by the invariance of the amide

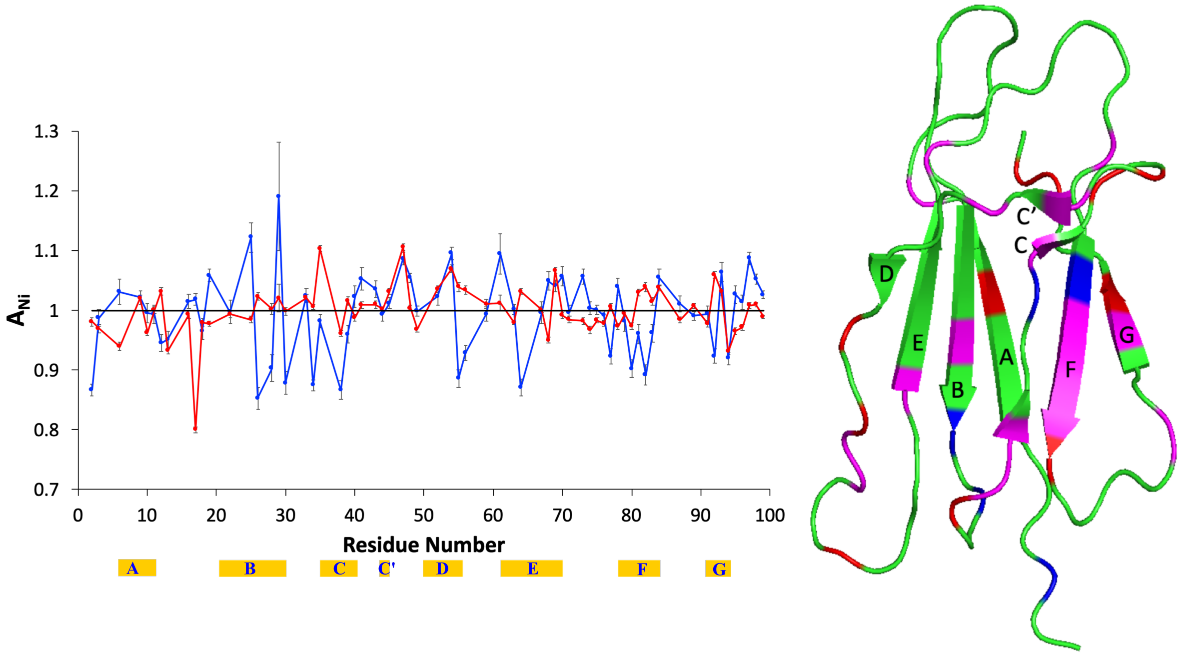

Figure 3.15: Overlay of the A_N values obtained from ^{1}H-^{15}N HSQC spectra of 8 μM β2m in presence of 0.8 mM Tempol, with relaxation delay of 0.5 s (blue) or 5 s (red). The β-strand location and naming along the sequence is reported with yellow strips. The cartoon on the right highlights the positions of the accessible amides (red), i.e. exhibiting A_N[eq] > 1, and the amides with Type II deviation of A_N[off-eq] (blue), i.e. displaying A_N[off-eq] < A_N[eq]. The magenta color denotes sites where both A_N[eq] > 1 and Type II deviation occur simultaneously. Here and elsewhere the reproduced structure is the NMR solution structure of β2m[13] (PDB code 1JNJ). The secondary structure elements of β2m are indicated according to the crystallographic naming scheme (PDB code 3HLA). Structures are always drawn with PyMOL (Schrödinger, Inc.).

signal chemical shifts (Figure 3.16), Type II deviation of A_N[off-eq] can be associated to local chemical or conformational exchange occurring on a ms-to-μs time scale that introduces additional relaxation contribution affecting both T_{1p} and T_{2p}[154]. The pattern of Figure 3.15 is different with respect to the corresponding one previously observed in diluted conditions, precisely at β2m concentration of 50 μM probed with 250 μM Tempol, Figure 3.12A,[154]. Apart from the larger error affecting the previous data, there are two important differences to point out. First, the former Tempol/protein ratio was 5:1, whereas here we consider a ratio of 100:1.

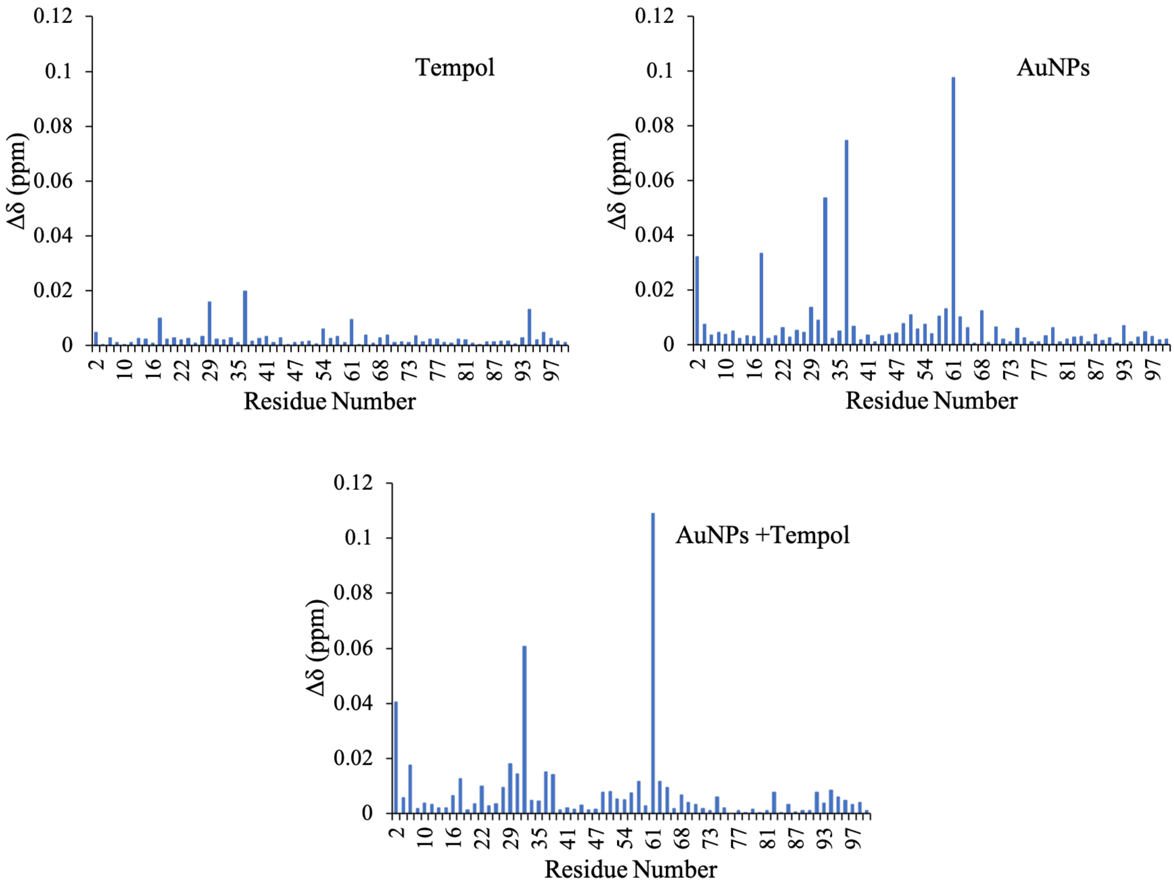

Figure 3.16: Chemical shift perturbation (CSP) of β2m backbone amide signals induced by Tempol (0.8 mM, protein/Tempol = 0.01) or AuNPs (60 nM, protein/AuNPs = 133) or AuNPs + Tempol (at the same concentrations and concentration ratios).
To properly account for both ^{1}H ($\Delta\delta_H$) and ^{15}N ($\Delta\delta_N$) frequency changes, the chemical shift variations ($\Delta\delta$) of the protein amide peaks from ^{15}N-^{1}H HSQC spectra in the presence of nitroxide or/and AuNPs were analyzed in terms of cumulated CSP.
Only CSP values above 0.02 ppm are considered meaningful (the limit should be increased to 0.05 ppm if the acquisition resolution is considered). This is the case of Q2, N17, S33, D38 and S61, in the presence of AuNPs, and Q2, S33 and S61 with AuNPs and Tempol. For the sample with Tempol only, all CSP are below the resolution significance.

These ratios and the absolute concentrations affect directly the collision probability[134]. We reasoned that a high Tempol/protein ratio is required to balance a low absolute concentration of β2m and measure the paramagnetic perturbation. This is confirmed by the slight increase above the unity of the average relative intensity, RI_{av}, (for RI definition see Materials and Methods) under off-equilibrium conditions[154] (Figure 3.17).

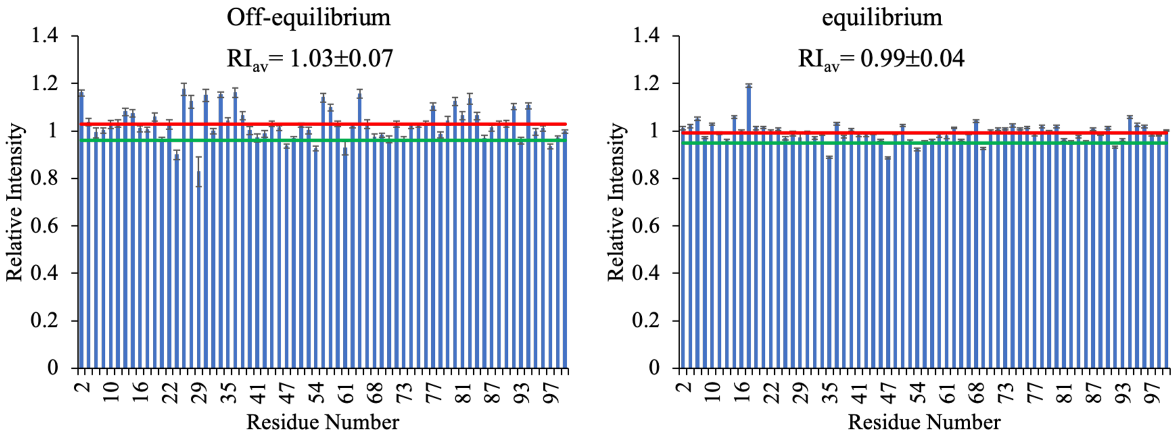

Figure 3.17: Relative intensities (RI) of β2m amide signals measured for the mixture of 8 μM protein and 0.8 mM Tempol. The RI values are the ratios on the peak heights in the presence and absence of the nitroxide. The experimental data are collected under magnetization equilibrium and off-equilibrium conditions
The average RI value and the standard deviation (RI_{av} ± SD) are given above the histograms and graphically indicated by red and green horizontal lines, respectively. It is worth noting that the equilibrium and off-equilibrium RI_{av} values are below and above 1, respectively, which is the signature of sufficient collision probability, i.e. sufficient concentrations and protein/nitroxide ratio.

Second, at 8 μM concentration, the extent of β2m dimerization and higher oligomerization should be further reduced compared to 50 μM[151,156,157]. Hence it could be possible to observe features related to the protein association interface. Table 3.9 lists the details of the pattern observed in Figure 3.15 compared to the earlier results at 50 μM, Figure 3.12A and Table 3.7[154]. The most relevant differences concern the higher exposure in the 8 μM solution of strands C, D, F and G and the intensification in local conformational or chemical exchange at strands C and F, with a simultaneous loss of accessibility at strand A and loop AB. Besides the relevance for the involvement in the association interface, these features are also important to delineate a starting point and thus appreciate interactions and structural effects the presence of AuNPs may induce.

The same paramagnetic perturbation analysis as done with isolated β2m can be performed for the system protein+AuNPs, because a statistical collision model can still be adopted, according to the ESR-based determinations of the Tempol τ_c values under different experimental conditions. Moreover, AuNPs are known to essentially preserve the chemical shifts, and therefore the structure, of β2m and D76N β2m[32,34,158], although at concentrations and protein/NP ratios as low as 4-8 μM and 100-200, small chemical shift deviations have been detected for both variants[32,158].

Table 3.9: Paramagnetic perturbation induced by 0.8 mM Tempol on the amide NMR signals of 8 µM β2m. Equilibrium (column 2) and off-equilibrium (columns 3 and 4) data are compared to the corresponding data obtained at 50 µM β2m and 1:5 Tempol:protein ratio (Table 3.7) [16] and reported below in italic fonts.

	$A_N > 1$	***Type I*** **A_N [*off-eq*] > A_N [*eq*]**	***Type II*** **A_N [*off-eq*] < A_N [*eq*]**
Structure region			
N-term, strand A	V9 *Q2, I7*	K6, Y10	Q2 *Q2, I7*
loop AB	*R12, K19*	H13, E16, N17, K19 *N17*	R12 *R12, H13*
strand B	Y26	C25, G29 *S28*	Y26, S28, F30 *N21, F22, C25, F30*
loop BC	S33, D34 *D34*	*S33*	D34 *D34*
strand C	I35, L39, K41 *I35*	L40, K41	I35, D38, L39 *I35*
turn CC’, strand C’, loop C’D	G43, R45, E47 *G43, E47, K48, V49*	G43, K48, V49 *R45, K48*	R45, E47 *N42*
strand D	S52, L54, S55, F56 *F56*	L54 *E50, L54*	S55, F56 *S52, F56*
loop DE	D59	S61 *D59*	*S61*
strand E	L64, E69 *E69*	Y63, T68, F70 *E69, F70*	L64, E69 *L64*
loop EF	E77 *K75*	T73, E74, K75, D76 *T71, E74*	E77
strand F	R81, V82, N83, H84 *N83, H84*	T78 *T78*	C80, R81, V82, N83 *A79, H84*
loop FG	Q89 *V85, L87*	L87	Q89 *V85*
strand G, C-term	I92, V93, R97, D98 *K94*	V93, W95, D96, R97, D98, M99 *V93, D96, D98, M99*	I92 *I92, K94*

Most of these deviations were observed with synthetic AuNPs with average diameter of 7.5±1 nm and therefore some difference can be expected on decreasing the NP diameter to 5 nm. With the commercial AuNPs here employed, minor chemical shift perturbations[159] are measured at Q2, N17, S33, D38 and S61 NHs of β2m, which in two cases (N17, D38) reduce below the resolution significance in the presence of Tempol (Figure 3.16). Given the substantial invariance of the fingerprint pattern in the ^{15}N-^{1}H HSQC spectra and the limited amounts of the frequency changes, the last mentioned

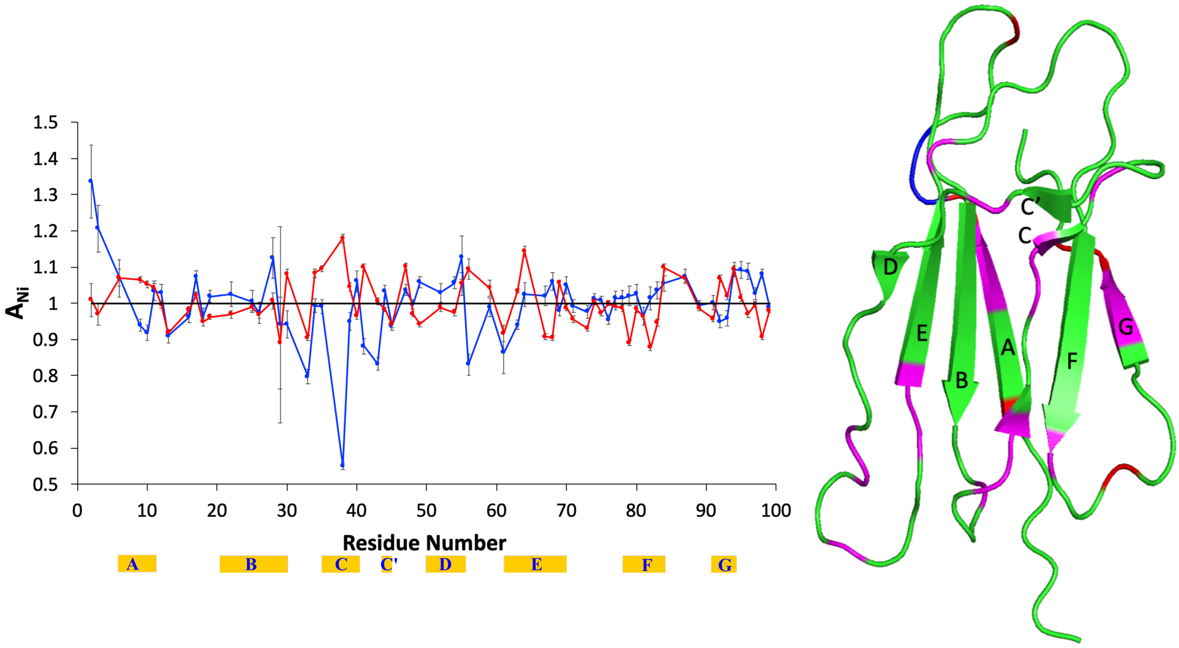

Figure 3.18: Overlay of the A_N values obtained from ^{1}H-^{15}N HSQC spectra of 8 µM β2m + 60 nM AuNPs in the presence of 0.8 mM Tempol, with relaxation delay of 0.5 s (blue) or 5 s (red). The β-strand location and naming along the sequence is reported with yellow strips. The cartoon on the right highlights the positions of the accessible amides (red), i.e. exhibiting A_N[eq] > 1, and the amides with Type II deviation of A_N[off-eq] (blue), i.e. displaying A_N[off-eq] < A_N[eq]. The magenta color denotes sites where both A_N[eq] > 1 and Type II deviation occur simultaneously. The secondary structure elements of β2m are indicated according to the crystallographic naming scheme (PDB code 3HLA).

deviations do not impair the assumption of statistical character for the nitroxide probing. All the previous evidence indicates, however, that AuNPs unevenly affect the intensity of the ^{15}N-^{1}H HSQC peaks of β2m and variants thereof[32–35,37,158]. Although this effect is precious to interpret the molecular details of the protein interaction with nanoparticles, it may prove detrimental when evaluating the paramagnetic attenuation contributed by the nitroxide probe, under magnetization equilibrium or off-equilibrium conditions. A preliminary control of the ^{15}N longitudinal relaxation rates is useful to estimate the entities of the effects brought about by AuNPs and Tempol on β2m signals (Figure 3.19). Indeed, the average T_1 value of 8 µM β2m decreases by the same extent, i.e. 4%, with AuNPs or Tempol, whereas the addition of the nitroxide to β2m in AuNPs suspension shortens the average T_1 only by 0.7%. This means that the Tempol paramagnetic attenuation probing the statistical sampling differences would be extensively masked by the general and specific dipolar attenuation AuNPs inflict to β2m signals, if the A_N values were computed with respect to the isolated protein intensities.

Table 3.10: Paramagnetic perturbation induced by 0.8 mM Tempol on the amide NMR signals of 8 µM β2m with 60 nM AuNPs. The equilibrium (column 2) and off-equilibrium (columns 3 and 4) data are reported in bold. The corresponding data obtained without AuNPs (Table 3.9) are reproduced below in plain fonts.

	A_N > 1	***Type I*** **A_N [*off-eq*] > A_N [*eq*]**	***Type II*** **A_N [*off-eq*] < A_N [*eq*]**
Structure region			
N-term, strand A	**K6, V9, Y10, S11** V9	**Q2, R3** K6, Y10	**V9, Y10** Q2
loop AB	**N17**	**N17, K19** H13, E16, N17, K19	**R12, H13** R12
strand B	**F30** Y26	**F22, S28** C25, G29	**F30** Y26, S28, F30
loop BC	**D34** S33, D34		**S33, D34** D34
strand C	**I35, D38, L39, K41** I35, L39, K41	**L40** L40, K41	**I35, D38, L39, K41** I35, D38, L39
turn CC', strand C', loop C'D	**E47** G43, R45, E47	**E44, K48, V49** G43, K48, V49	**E47** R45, E47
strand D	**S55, F56** S52, L54, S55, F56	**S52, L54** L54	**S55, F56** S55, F56
loop DE	**D59** D59	S61	**D59**
strand E	**Y63, L64, E69** L64, E69	**Y67, T68, F70** Y63, T68, F70	**Y63,L64, E69** L64, E69
loop EF	E77	**T71, T73, K75** T73, E74, K75, D76	E77
strand F	**H84** R81, V82, N83, H84	**A79, C80, V82, N83** T78	**H84** C80, R81, V82, N83
loop FG	**L87** Q89	L87	Q89
strand G, C-term	**I92, V93, K94, W95** I92, V93, R97, D98	**K91, W95, D96, R97, D98** V93, W95, D96, R97, D98, M99	**I92, V93** I92

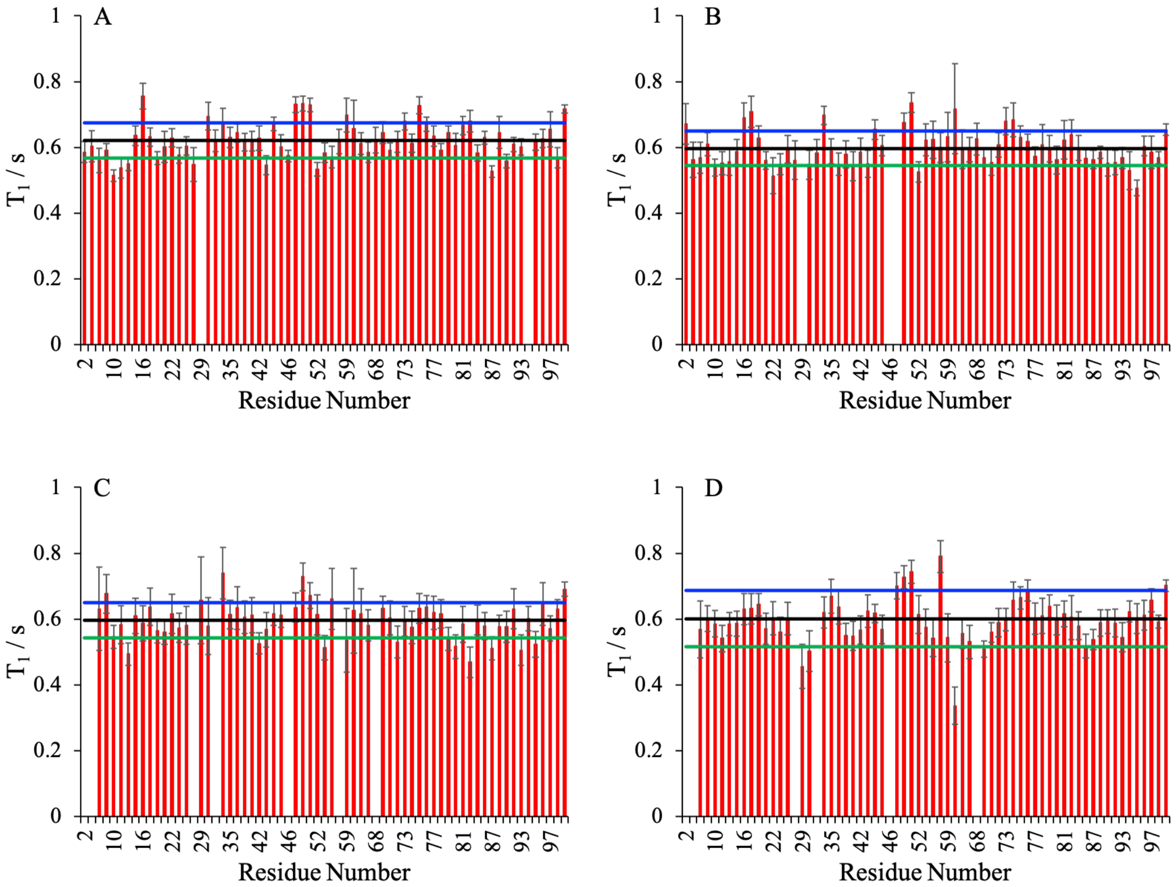

Figure 3.19: ^{15}N longitudinal relaxation times (T_1) of resolved backbone amide signals of β2m. The average T_1 value and the displacements by ± SD (standard deviation) are represented as black, blue and green horizontal lines. A) 8 µM β2m, average T_1 = 0.621±0.054 s. B) 8 µM β2m + 0.8 mM Tempol, average T_1 = 0.597±0.052 s. C) 8 µM β2m + 60 nM AuNPs, average T_1 = 0.596±0.054 s. D) 8 µM β2m + 0.8 mM Tempol + 60 nM AuNPs, average T_1 = 0.592±0.063 s.

In conclusion, proper control intensities should be obtained from the protein sample in the presence of AuNPs rather than from the protein alone. Figure 3.18 shows the attenuation pattern of the backbone amide signals observed with 8 µM β2m and 60nM AuNPs due to 0.8 mM Tempol. According to the preliminary T_1 control measurements, the A_N values are calculated with respect to the control solution, i.e. the sample with the same composition without the nitroxide. Compared to the A_N profile of the isolated protein (Figure 3.15), evident differences emerge in the A_N plot of Figure 3.18 concerning exposed or poorly accessible regions, as well as locations undergoing chemical or conformational exchange. In particular, AuNPs hinder accessibility at the N-terminal, end of strand B, loop CC' and subsequent strand C', start of strand D, strand F and C-terminal of β2m, while increasing strand A exposure. The details of these differences can be appreciated from Table 3.10 that lists the equilibrium and off-equilibrium attenuation data with and without AuNPs, thereby enabling a direct comparison.

The results above described must be analyzed from two viewpoints. On one side, the nitroxide-based screening on the free protein helps to gather elements on the association processes β2m undergoes in solution. These elements may reveal features related to the fibrillogenic propensity of β2m. On the other side, the same paramagnetic probing of the protein in the AuNPs suspension provides the elements that enable outlining the β2m interaction with those nanoparticles. Joining these two lines of evidence is particularly tempting because it is thus possible to focus the mechanism of fibrillogenesis inhibition experimentally observed with AuNPs and the β2m variant D76N[34].

As pointed out in the previous section, the most relevant differences highlighted by equilibrium and off-equilibrium nitroxide collisional labelling when comparing the 8 μM and the 50 μM β2m solutions concern the higher exposure in the former of strands C, D, F and G and the intensification in local conformational or chemical exchange at strands C and F, with a simultaneous loss of accessibility at strand A and loop AB (Table 3.9). This result is consistent with the previous inference and evidence addressing respectively the intermolecular interface in ΔN6 β2m, the variant devoid of the N-terminal hexapeptide fibrils[156], and the H-D exchanged β2m fibrils dissolved in DMSO[160]. It is worth noting that for strands C and F the increased accessibility is paralleled by the onset, at the same positions, of exchange events (A_N[off-eq] Type II deviations, Table 3.9) that must witness the remnant of the intermolecular interaction propensity at those locations.

The statistical sampling of Tempol shows that the presence of AuNPs exposes strand A and limits accessibility at the very N-terminal segment, turn CC' and strand C', start of strand D, strand F and C-terminal region of β2m. Again, the gain or loss of accessibility at strands A, C' and F, and turn CC' are accompanied, at the same locations, by gain or loss of Type II deviation of A_N[off-eq]. Except for the N-terminal fragment (Q2, R3), however the interaction pattern obtained by paramagnetic perturbation does not seem to match the previously reported picture based on relative intensity losses affecting essentially the end of strands B and D, and loops BC and DE[32]. The differences in β2m concentrations (8 vs. 26 μM) and protein/AuNPs ratios (100 vs. 200) between present and previous experiments could certainly play a role in determining some deviations. However relative intensity changes and paramagnetic perturbation monitor different aspects of β2m interaction with AuNPs and thus the mismatch may be only apparent. In fact, much like the previously reported low relative intensity of Q2 and R3 induced by AuNPs translates into Type I deviation of A_N[off-eq] , i.e. hindered accessibility to nitroxide probe, when assayed by paramagnetic perturbation, a similar effect is seen also for S28 (strand B) in Table 3.9. More frequently, instead, the β2m residues reported to lower the relative intensities due to AuNP interaction[32], exhibit Type II deviation of A_N[off-eq], i.e. local exchange, with nitroxide probing in the presence of AuNPs, most often coupled to accessibility above average (A_N[eq] > 1).

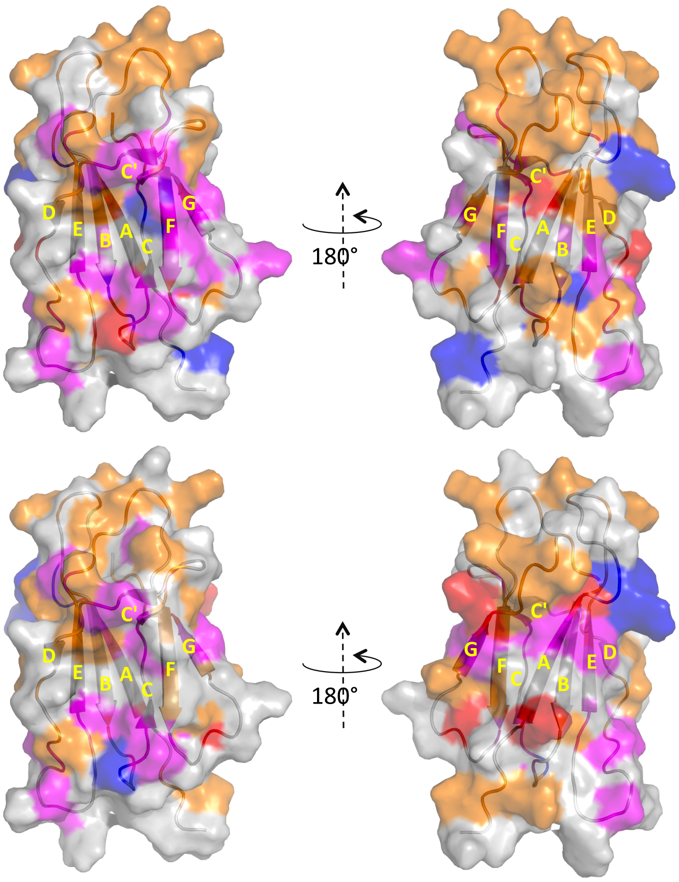

Figure 3.20: Cartoon representation of β2m surface sampled by Tempol in the absence (upper pair) and presence (lower pair) of AuNPs. The positions of the accessible backbone amides, i.e. exhibiting A_N[eq] > 1, are marked in red. The locations of the amides with Type I or Type II deviation of A_N[off-eq], i.e. displaying A_N[off-eq] > A_N[eq] or A_N[off-eq] < A_N[eq], are highlighted in orange or blue, respectively. The magenta color denotes sites where both A_N[eq] > 1 and Type II deviation occur simultaneously. The very few positions where A_N[eq] > 1 and Type I deviation coincide were left in orange. The secondary structure elements of β2m are indicated according to the crystallographic naming scheme (PDB code 3HLA).

This is the case with the end of strands B and D, and with the involved locations at BC and DE loops (Table 3.9). Therefore, the picture emerging from the interpretation of the results obtained by equilibrium and off-equilibrium paramagnetic mapping does not conflict with the previous evidence, but rather provides a more detailed and enriched characterization of the interaction between β2m and AuNPs. This appears quite clearly by inspection of Figure 3.20 where the surface of the protein according to the equilibrium and off-equilibrium attenuation pattern induced by Tempol in the absence (upper structures) and presence (lower structures) of AuNPs is highlighted.

Hindered accessibility is marked by orange surfaces that change their distribution on moving from the isolated protein to the presence of AuNPs. In either conditions, those surfaces could be associated to regions that become screened by the relevant interaction, namely the residual protein-protein or the protein-nanoparticle one. The occurrence of exchange processes at the blue and magenta locations can be considered the consequence of an interaction which takes place over the ms-to-μs time scale and may represent a further interface with different dynamic properties with respect to the hindered accessibility surface, provided the occurrence of local conformational exchange process is ruled out[154]. Finally, the highly accessible positions that are identified in red, indicate the surface that is not involved in any protein-protein nor protein-nanoparticle contact. Based on the discussed evidence for β2m alone[156,160] and with AuNPs[32,33], the results listed in Tables 3.9 and 3.10 and depicted in Figure 3.20 suggest that the AuNP interference leading to inhibition of fibrillogenesis[34,158] could occur via interaction of the nanoparticles with the N-terminal and strands D and F of β2m, in addition to other contacts at turn CC' and strand C'. The hypothesis is that these interactions prevent the protein-protein contacts at the same locations that are necessary for fibrillogenic aggregation.

The results here described demonstrate that the paramagnetic perturbation methodology can be successfully applied to study protein-nanoparticle interactions. In addition to the surface accessibility mapping, extrinsic paramagnetic probes can provide valuable information on hindered accessibility and exchange processes by means of off-equilibrium attenuation analysis. This methodology represents an additional tool that enriches the NMR relaxation approach to the characterization of protein interaction with the nanoparticle surface. The delineation of the contact interface between protein monomers and between protein and nanoparticles is important not only for the comprehension of the mechanisms of protein aggregation and the elaboration of contrast strategies that bear particular relevance in amyloidogenic systems, but also for the characterization of that ensemble of labile contacts that is involved in the build-up of the so-called soft corona, i.e., the coating layer of weakly bound protein molecules with short residence times that can affect the nanoparticle targeting.

3.3 Self-association study of β2-Microglobulin mutant D76N by paramagnetic perturbation NMR spectroscopy

The effect of dilution of D76N in the solvent 66.5 mM phosphate buffer, 95 mM NaCl at the pH 7 has been investigated in the presence and absence of paramagnetic probe, Tempol, by paramagnetic NMR to map the protein surface accessibility, hindered accessibility, and exchange process.

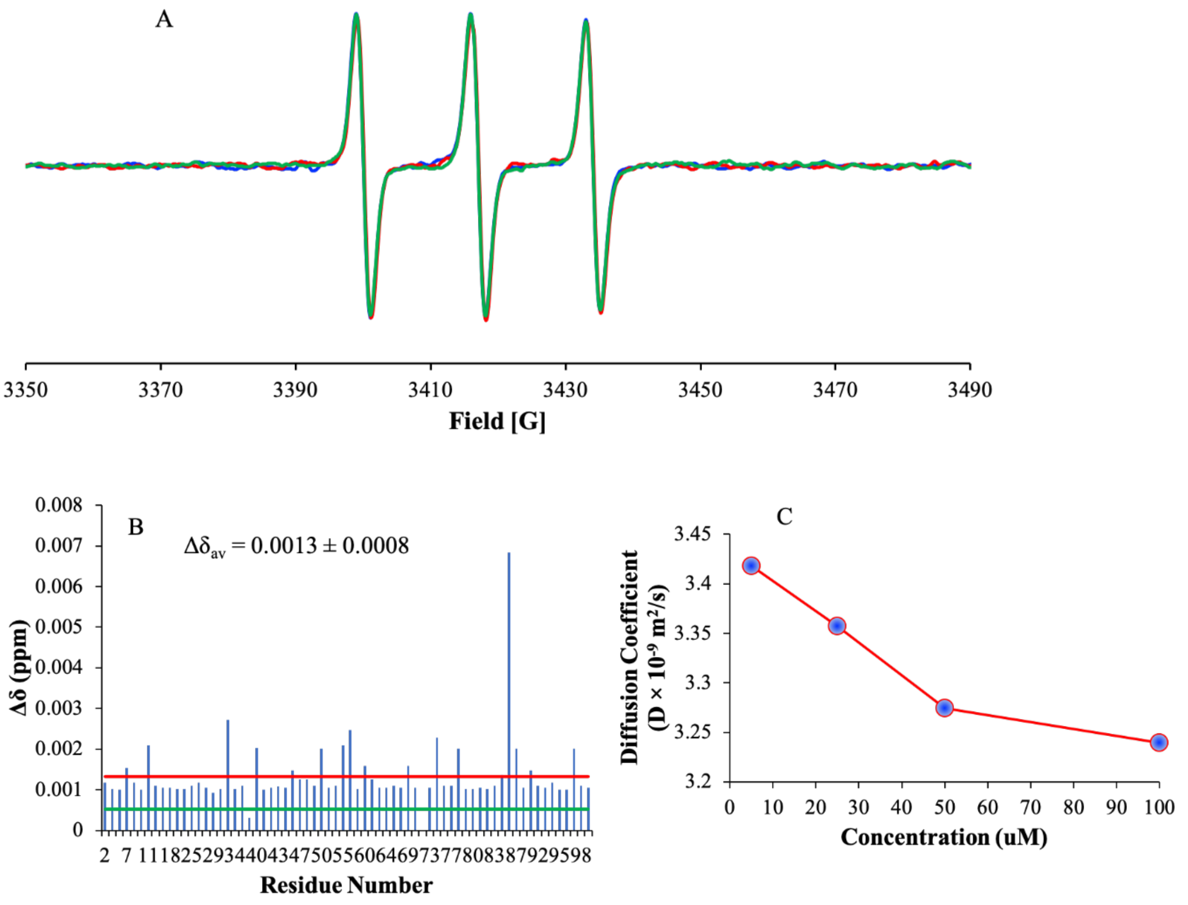

Figure 3.21: (A) Overlay of ESR spectra of Tempol (red), D76N+Tempol at 1:1 (blue), and D76N+ Tempol at 1:5 (green). (B) Bar plot of amide chemical shift perturbation (Δδ), two horizontal lines indicates that the average change in chemical shift value (red) and the displacement of one standard deviation (blue). (C) Plot of translational diffusion coefficient of D76N as a function of its concentration.

The ESR measurements of Tempol have been carried out to gain preliminary information of protein and paramagnetic probe interaction using same experimental conditions. There is no significant change in line widths of ESR Tempol data in the presence and absence of D76N as shown in Figure 3.21A, which is consistent with our previous work on β2m[154]. After the addition of Tempol to D76N, there is no significant change in NMR chemical shift (Figure 3.21B). All chemical shift changes are within the experimental uncertainty calculated from spectral digitalization that is ±9.8×10^{-3} ppm. This confirms that there is no specific interaction between the D76N and Tempol[137,154].

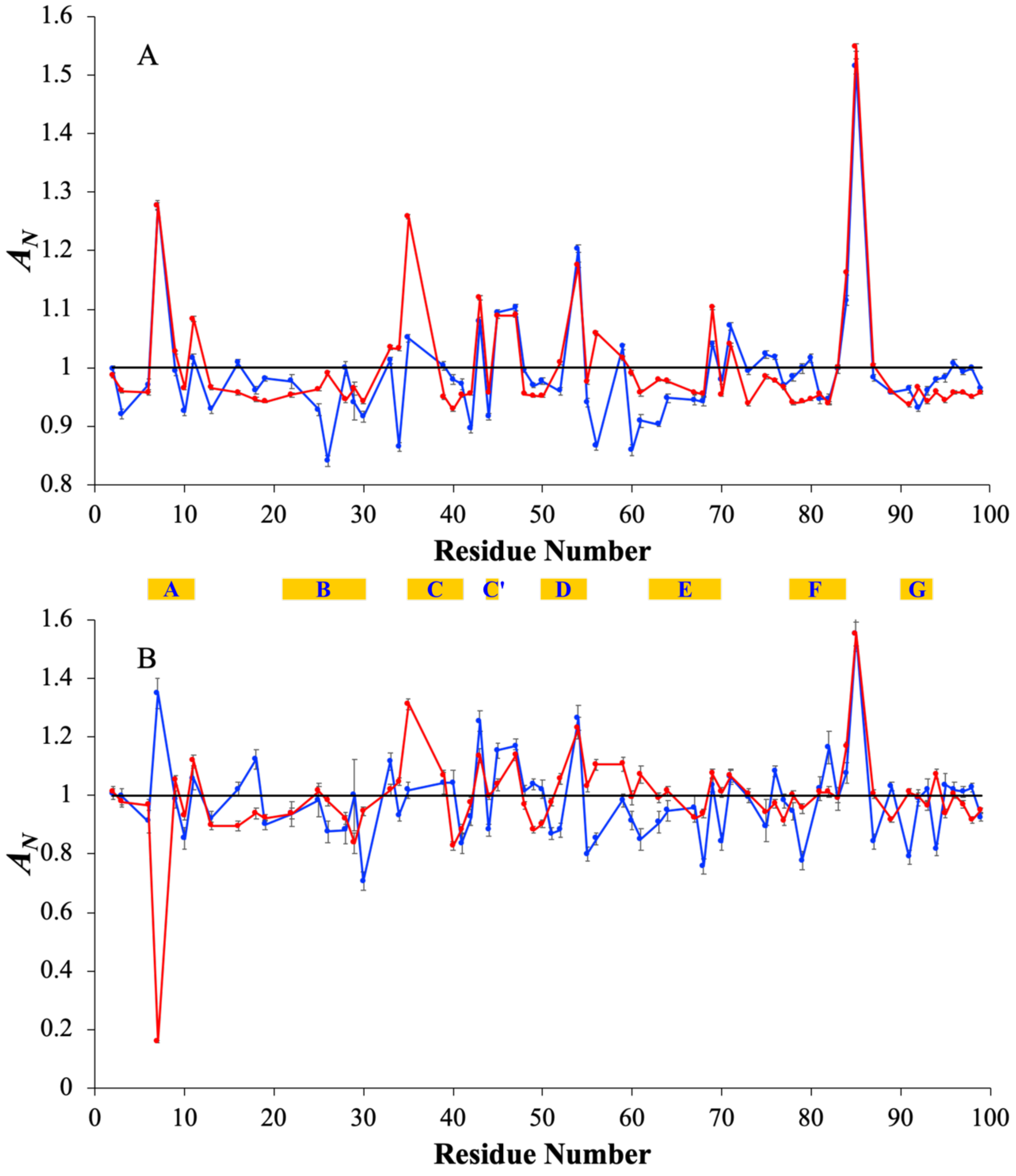

Figure 3.22: Overlay plot of the A_N values obtained from ^{1}H-^{15}N HSQC spectra of (A) 220 μM and (B) 4 μM D76N in the presence of 1.6 mM Tempol, at 298K with relaxation delay of 0.5 s (blue) and 4 s (red). The yellow strip indicates the naming of the β-strands.

The translational diffusion coefficient of D76N, measured by using Diffusion ordered spectroscopy[161] (DOSY) and plotted as a function of the protein concentration (Figure 3.21C) shows that higher order oligomers form upon increasing concentration from 4 μM to 220 μM. Self-association studies of D76N in the presence and absence of Tempol was carried out using 220 μM and 4 μM, concentration solution

Figure 3.22 shows that the pattern of normalized attenuation (A_N) values calculated from 220 μM D76N in the presence of 1.6 mM Tempol (A) and 4 μM D76N in the presence of 1.6 mM Tempol. In either case, attenuations are calculated with respect to the corresposnding D76N protein solutions in the absence of Tempol. The backbone amide signal A_N values are calculated from the data collected under off-equilibrium magnetization conditions (A_N[off-eq]) and equilibrium magnetization conditions (A_N[eq]) and showed in blue and red lines, respectively. According to our previous interpretation[114,133,154], the A_N values are divided into three parts i.e. A_N[eq] >1, Type I (A_N[off-eq] > A_N[eq]) and Type II (A_N[off-eq] < A_N[eq]). A_N[eq] >1 corresponds to attenuation above the average signal attenuation, i.e. 1, and this helps to identify the molecular locations which are exposed or accessible to the Tempol.

Table 3.11: Tempol perturbation on the NMR data of 220 μM D76N at 298K. The residues which are not common compared to 4 μM are reported in bold.

Structure region	**AN>1**	**Type I**	**Type II**
N-term, strand A	**I7**, V9, S11	**Q2**	**R3**, V9, Y10, S11
loop AB		E16, G18, **K19**	**H13**
strand B		**F22**, **S28**	**C25**, Y26, F30
loop BC	**S33**, D34		**S33**, D34
strand C	I35	**L39**, L40, **K41**	I35
turn CC', strand C', loops C'D	G43, R45, E47	**E47**, K48, V49	N42, **G43**, E44
strand D	S52, L54, F56	E50, **L54**	S52, S55, F56
loop DE	D59	**D59**	W60, S61
strand E	E69	**F70**	Y63, L64, E69
loop EF	T71	**T71**, **T73**, **K75**, N76	
strand F	H84	**Y78**, **A79**, **C80**	H84
loop FG	V85, **L87**		**V85**, L87
strand G, C-term		**K91**, V93, **K94**, W95, **D96**, R97, D98, **M99**	I92

Type I deviation corresponding to A_N[off-eq] > A_N[eq], identifies the amide positions with either structurally buried or locally hindered accessibility on the molecular surface and Type II deviations corresponding to A_N[off-eq] < A_N[eq], identifies the residues which are involved in conformational or chemical exchange occurring on a μs-to-ms time scale[154]. The A_N pattern in Figure 3.22A and Figure 3.22B are different due to extent of formation of dimers and higher ordered oligomers[151,156,157] at the two different protein concentrations.

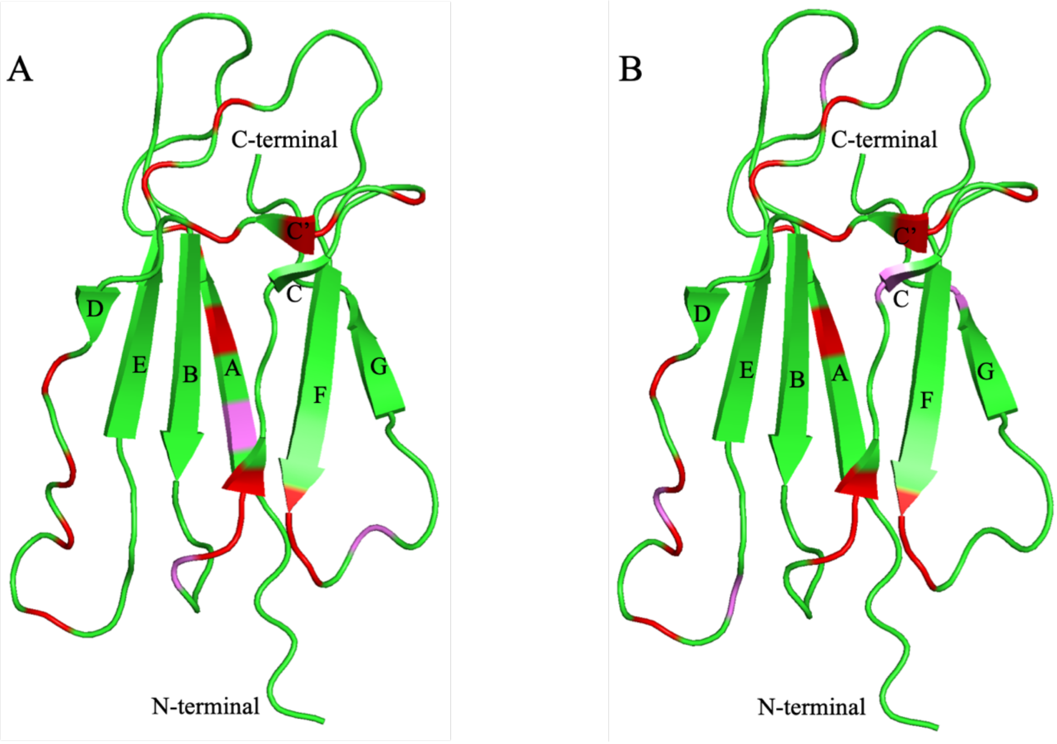

Figure 3.23: Location of the exposed backbone amides of D76N i.e. exhibiting A_N[eq] > 1, (A) 220 µM and (B) 4 µM. The red color denotes sites which are common at both concentrations and violet color denotes sites that are not in common at both concentrations.

The A_N results are listed in Table 3.11 and Table 3.12, are obtained from Figure 3.22A and 3.22B respectively. The residues which are not common at both conditions are reported as bold and highlighted in violet in the all cartoon representations. The sampling of Tempol to 220 µM and 4 µM shows that changes in the surface exposure to Tempol (Figure 3.23), which can be ascribed to association of the protein at higher concentration. The residues E16, L39, S55, S61, K94 are exposed at 4 µM but buried or covered by oligomerization at 220 µM.

Table 3.12. Tempol perturbation on the NMR data of 4 μM D76N at 298K. The residues which are not common compared to 220 μM are reported in bold.

Structure region	**AN>1**	**Type I**	**Type II**
N-term, strand A	V9, S11	**I7**	V9, Y10, S11
loop AB	**E16**	E16, G18	
strand B		**G29**	Y26, F30
loop BC	D34	**S33**	D34
strand C	I35, **L39**	L40	I35
turn CC', strand C', loops C'D	G43, R45, E47	**G43**, **R45**, K48, V49	N42, E44
strand D	S52, L54, **S55**, F56	E50	**H51**, S52, S55, F56
loop DE	D59, **S61**		**D59**, W60, S61
strand E	E69		Y63, L64, **T68**, **F70**
loop EF	T71	N76, **E77**	
strand F	H84	**V82**	**Y78**, **A79**, H84
loop FG	V85	**Q89**	L87
strand G, C-term	**K94**	V93, W95, R97, D98	**K91**, **K94**, **M99**

The pattern of Type I deviation (A_N[off-eq] > A_N[eq]) highlights the backbone amides which are structurally buried and therefore inherently scarcely affected by Tempol. This leads to reduction of recovery of amide signals when short relaxation delays are employed. The residues which are exhibiting Type I deviations are highlighted in Figure 3.24. This figure clearly shows that the C-terminal side loops (broken blue ovals) are structurally buried at high concentration. The comparison between panels 3.24A and 3.24B shows a decrease number of the backbone amides exhibiting Type I effect in Figure 3.24B, which further explains that the increase in oligomerization by increasing the concentration makes more stable C-terminal side loops.

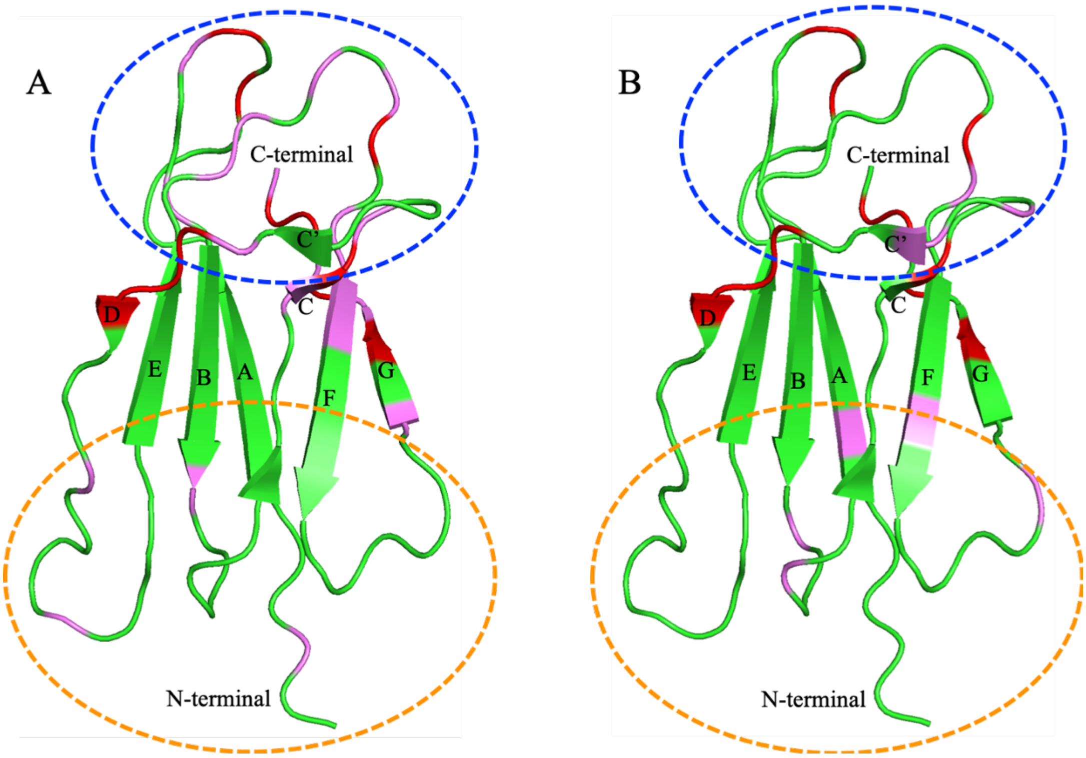

Figure 3.24: Location of the backbone amides of D76N whose NMR signals exhibit Type I deviations at (A) 220 µM and (B) 4 µM. The red color denotes sites which are common at both concentration and violet those that are not common. The loops on the same side as the C terminus of the molecule are named C-terminal-side loops (broken blue ovals) and the loops on the opposite side are called N-terminal-side loops (broken orange ovals)

The mutation point (D76) is located at the C- terminal side of the protein molecule. The effect of this mutation was assumed to be transmitted to the N-terminal side of the molecule[162]. Type II deviations from the normalized attenuation may support this. Figure3.25 highlights in panels A and B the residues which are undergoing exchange, either chemical or conformational. The important point is that many backbone amides of the C-terminal-side loops are not accessible to the paramagnetic probe (Figure 3.24A) but, surprisingly, the majority of the residues from N-terminal-side loops exhibits Type II effect, i.e. is involved in exchange. The number of residues of N-terminal loops involved in exchange process is already conspicuous at low concentration and further increases at higher concentration. From this we can conclude that in the D76N mutant, C-terminal-side loop region is more rigid than the N-terminal-side loops region.

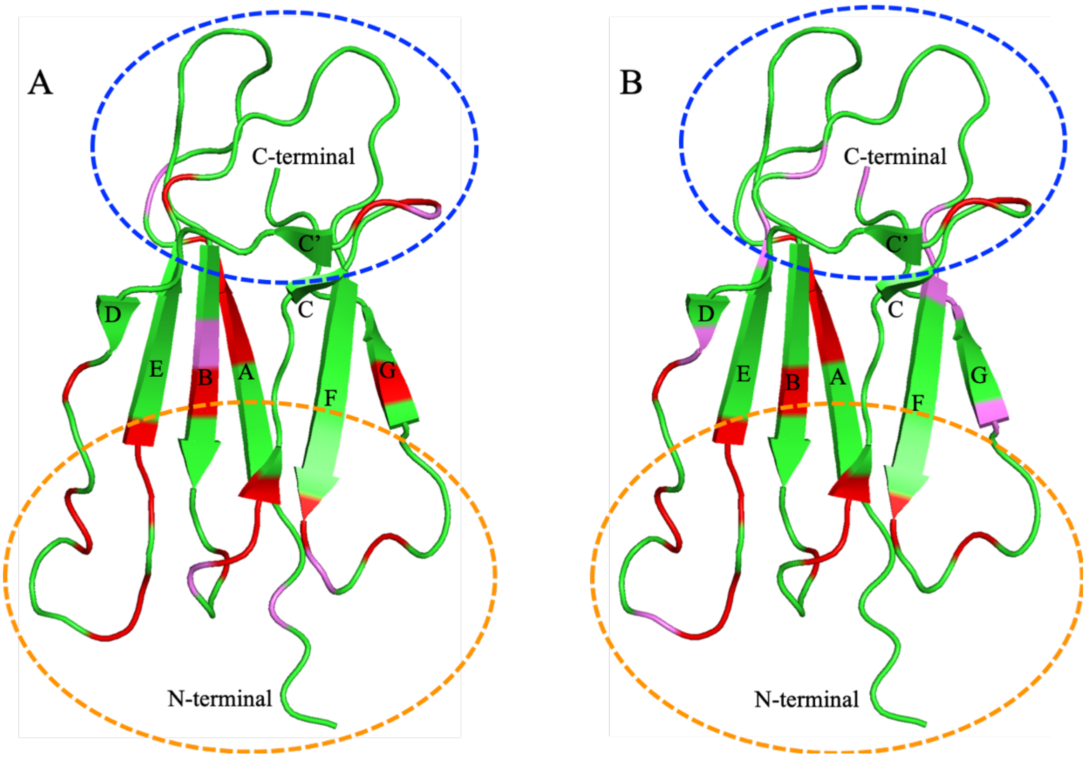

Figure 3.25: Location of the backbone amides of D76N whose NMR signals exhibit Type II deviations (A) 220 µM and (B) 4 µM. The red color denotes sites which are common in both concentration and violet are not common. Loops on the same side of the C terminus of the D76N molecule are called C-terminal-side loops (broken blue ovals) and opposite side are called N-terminal-side loops (broken orange ovals)

The residues showing Type II deviations that are not in common at 220 µM (Figure 3.25A) and 4 µM (Figure 3.25B, highlighted in violet) give an important information. Because of dilution from high to low concentration and the conceivable reduction of association, the chemical exchange brought about by association can be identified. It is unclear whether at 4 µM D76N is monomer or dimer. However, when we compare the Type II deviations of Figure 3.25, the residues R3, H13, C25, S33, G43, V85 do no longer show Type II deviations at low concertation possibly because of involvement in association of D76N, whereas, the residues H51, D59, T68, F70, Y78, A79, K91, K94, M99 appear at low concentration possibly because of involvement in conformational exchange as shown in Figure 3.26.

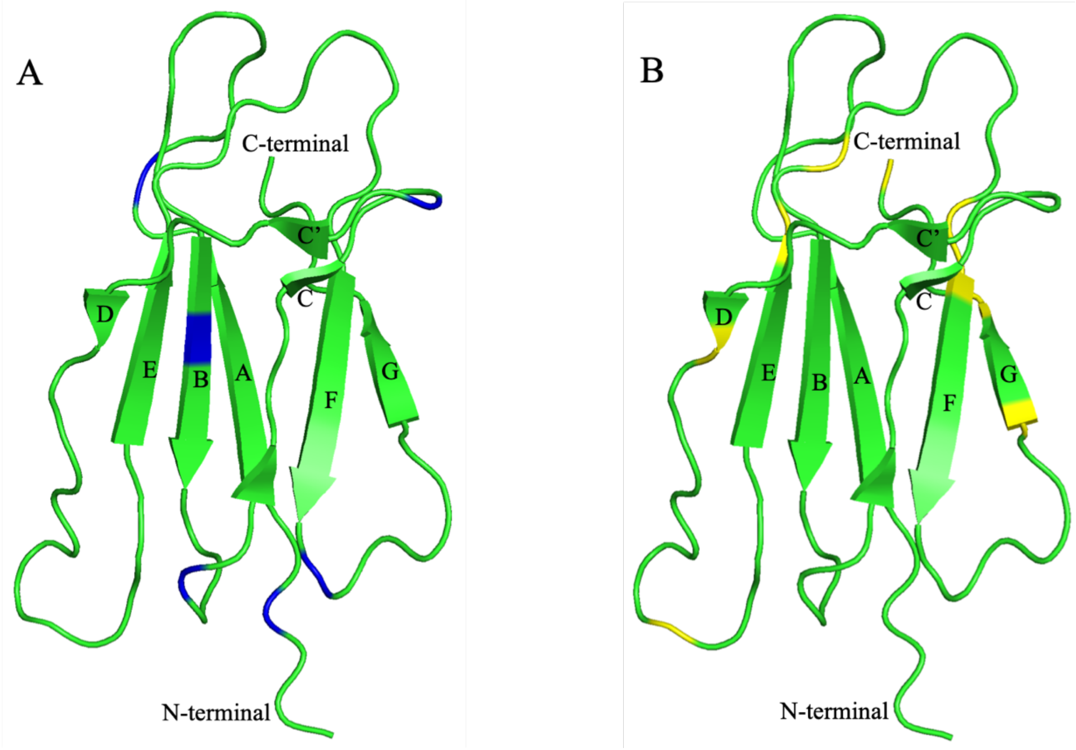

Figure 3.26: Comparison of location of the backbone amides of D76N whose NMR signals exhibit Type II deviations. (A) the Type II residues disappearing at low concentration in blue and (B) the Type II residues appearing at low concentration in yellow.

The results here described demonstrate that the paramagnetic perturbation methodology can be successfully applied to study distinguish conformational and chemical exchange process from successive dilution. By doing successive dilution of the protein sample one can suppress the exchange brought about by an association and this will help to identify the residues which are involved in association. In addition to the surface accessibility mapping, extrinsic paramagnetic probes can provide valuable information on hindered accessibility and exchange processes by means of off-equilibrium attenuation analysis.

3.4 Final Considerations

In this thesis a new method has been described to identify the degree of exposure of protein locations based on the paramagnetic perturbation of the protein NMR spectrum.

Whilst a clear attenuation of the NMR signals, induced by a paramagnetic probe, definitely identifies accessible regions on a protein surface, limited attenuations may be consistent with either buried locations or surface regions with hindered accessibility that can, in fact, be recognized through the proposed method. In addition, the same method also enables one to recognize positions of the protein undergoing conformational or chemical exchange on a time scale ranging in the ms-to μs interval.

The technique was applied to investigate the association equilibria of a paradigmatic amyloidogenic motif, its interactions with nanoparticles and the dimerization interface of an enzyme. The methodology can be used however for many other types of high-resolution NMR investigations. For instance, protein folding or unfolding can be characterized in terms of structural evolution throughout the process to identify intermediates. Transient adducts along an interaction pathway can be characterized. The locations of conformational flexibility along with their determinants can be identified in either isolated proteins or in protein-ligand complexes where the ligand can be a small molecule, another protein or an oligonucleotide. Further work is already going on along these directions.

4. MATERIALS AND METHODS

4.1 Chemicals

Sodium Citrate, ^2H_2O, Tempol (4-hydroxy-2,2,6,6-tetramethyl-piperidine-l-oxyl) and Hepes (N-(2-Hydroxyethyl)piperazine-N′-(2-ethanesulfonic acid) were all from Sigma Aldrich (St. Louis, MO, USA). From the same source were also the citrate-stabilized Au nanoparticles, here referred to as AuNPs. The average AuNP diameter was 5 nm and the supplied suspension concentration was 91 nM.

4.2 Exploring exchange processes in proteins by paramagnetic perturbation of NMR spectra

4.2.1 Sample preparation

The ^{15}N-uniformly labelled wild-type human β2m was expressed with an additional methionine at the N-terminus (Met-0) and purified as previously reported[156]. The β2m protein samples were prepared in H_2O/D_2O 95/5, 66.5 mM phosphate buffer, 95 mM NaCl, pH 7. Protein concentrations were 360 μM, 320 μM and 50μM as determined by UV absorption at 280 nm. A few microliters of 190 mM and 25 mM solutions of Tempol (4-hydroxy-2,2,6,6-tetramethyl-piperidine-l-oxyl, Sigma) were added to the NMR tube containing 0.500 mL of β2m to reach a Tempol/protein concentration ratio of 5, according to a previous experimental optimization[133]. Hen egg white lysozyme (HEWL) was purchased from Sigma and used after recrystallization at pH 3.5 and lyophilization. A mother solution of 1 mM HEWL was prepared in H_2O/D_2O 95/5 and 50 mM glycine-d6 (Cambridge Isotope) buffer at pH 3.9. A few microliters of a concentrated Tempol solution were added to 0.500 mL aliquots of mother solution to reach 5 mM corresponding to a fivefold Tempol concentration with respect to protein.

4.2.2 Spectroscopy

Most of the NMR experiments (^{1}H 1D, 2D TOCSY, ^{15}N-^{1}H HSQC) were performed at 11.7 T (^{1}H resonance at 500.13 MHz) on a Bruker Avance spectrometer equipped with triple resonance and triple axis gradient probe. CPMG relaxation dispersion experiments were collected at 14.0 T (^{1}H resonance at 600.13 MHz) on a Bruker Avance III NMR system equipped with triple resonance cryoprobe. All the spectra of β$_2$m were acquired at 298 K or 310 K. The two-dimensional ^{15}N-^{1}H HSQC experiments[163], carried out via double INEPT transfer, sensitivity-improved Echo/Antiecho-TPPI pure phase detection in F1, gradient coherence selection and flip-back pulse for solvent suppression[164–166], were acquired over spectral widths of 33.5 ppm and 14 ppm in F1 and F2 dimensions, respectively, with 128 time-domain points in t1, 32–64 scans × 2048 points in t2 and always 64 dummy scans to achieve steady state. Different relaxation delays were set, namely 0.5 and 4 s at 298K and 0.5 and 5 s at 310K. The lower bounds were selected to avoid depressing too much the overall sampled signal intensity. The observed trends are in fact accentuated by setting smaller relaxation delay values (Figure 3.11), but a tradeoff between highlighting relaxation-delay-dependent differences and experimental sensitivity is necessary. The upper bounds were selected after preliminary tests to ensure sampling of equilibrium magnetization signals at either temperatures. The longitudinal relaxation rates, determining equilibrium recovery, depend in fact on the rotational tumbling rates that change with temperature. All NMR data were processed with TOPSPIN version 4.0.2. Prior to Fourier transformation, linear prediction in t1 (up to 160 points) and zero filling were applied to yield final data set of 2K × 1K points. For relaxation dispersion[146] experiments, data were recorded with the sequence described by Tollinger et al.[147] at 18 different effective fields (0, 25, 30, 40, 50, 60, 70, 80, 100, 150, 200, 300, 400, 500, 600, 800, 1000, 1200 Hz) and the analysis of the results was performed by means of the Bruker Dynamics Center 2.5.3 software. The routine employed by Dynamics Center models the experimental data with the best fitting out of three different functions (reported in Table 3.5), depending on whether the dispersion curve is flat (independent on the effective field), or modulated by slow or intermediate exchange rate. The error on the fit parameters (exchange rates, frequency difference between the exchanging sites and populations) is estimated by the Dynamics Center routine via Montecarlo simulations to a 95% confidence. The relevant fitting data are reported in Table 3.5 (and plotted in Figure 3.10). 2D TOCSY[167] spectra of HEWL samples were acquired at 313 K, with solvent suppression achieved by Wartegate-based excitation sculpting[168,169], 0.5 to 5 sec relaxation delay, isotropic mixing time (t_m) of 20 ms, t1 quadrature detection by TPPI[170]. The spin-lock mixing was obtained with MLEV17[171] pulse train at $\gamma B_2/2\pi \sim 10$ kHz. All acquisitions were performed over a spectral width of 15 ppm in both dimensions with matrix array size of 2048 points in t2 and 400 points in t1, and 32–64 scans.

$T_{1\rho}$ measurements were performed with the sequence of Daye and Wagner[172] using spin-lock field strengths (SL) of 3.00 and 1.67 kHz and 20 spin-lock intervals ranging between 0 and 160 ms, with 3 repetitions at short, medium and large intervals for error estimation. The HSQC detection was performed with quadrature in F1 obtained by Echo/Antiecho-TPPI, gradient coherence selection and flip-back pulse for solvent suppression[165,166,173]. In all measurements, an interscan relaxation delay of 3 s was allowed. The number of scans for each collected relaxation interval was 32. The experiments were acquired in the pseudo3d mode and processed with the Bruker Dynamics Center software. Offset corrections[174] were applied.

Control ESR spectra were collected with a Bruker EMXnano spectrometer on 10 μM Tempol dissolved in aqueous buffer (70 mM phosphate, 100 mM NaCl, pH = 7), either alone or with β_2m, at 1:1 or 5:1 protein:Tempol ratio. Capillaries filled with 50 μL of each solution were placed in standard 4 mm tubes and submitted to acquisition (20 scans). The ESR operating parameter were: frequency = 9.6 GHz; microwave power = 0.316 mW; modulation amplitude = 1 Gauss; modulation frequency =100 kHz; center field = 3429.8 Gauss; sweep width = 200 Gauss; time constant = 1.28 ms. The data were processed using the Bruker software package Xenon.

4.2.3 Attenuation calculation

Amide cross-peak intensities in ^{15}N-^{1}H HSQC spectra of β2m in the absence (I_d) and in the presence (I_p) of Tempol were measured by SPARKY 3.133 software (T.D. Goddard and D.G. Kneller, University of California). Preliminary controls ensured that using cross-peak heights gives in practice the same results as obtained with the corresponding cross-peak volumes.

Although, in principle, measuring peak intensities by heights or by volumes is expected to give different results, the reduced digital resolution of 2D spectra and the difficulty of boxing accurately the individual signals for volume estimation introduce variable errors that in fact lead to an empirical equivalence of peak heights and volumes. Normalized paramagnetic attenuation, A_N, was calculated according to Eq. 23[114]

$$A_N^k = \left(2 - \frac{I_p^k}{I_d^k}\right) \tag{23}$$

where the running index *k* refers to the kth residue amide cross-peak and the $\iota_{p,d}^{k}$ values are the corresponding auto-scaled intensities of the peaks in the presence (subscript *p*) and absence (subscript *d*) of the nitroxide, defined as

$$\iota_{p,d}^{k} = \frac{I_{p,d}^{k}}{\frac{1}{n}\sum_{k=1}^{n} I_{p,d}^{k}} \tag{24}$$

with *n* representing the total number of measured peaks. From the above equation, it is seen that the scaling factor is simply the mean value over the *n* molecular locations for which the corresponding peak intensity can be estimated ($I_{p,d}^{av}$). By definition, the mean value of the individual auto-scaled intensities is unitary:

$$\frac{1}{n}\sum_{k=1}^{n} \iota_{p,d}^{k} = 1 \tag{25}$$

Therefore, values of A_N above or below unity indicate larger or smaller attenuations, respectively, with respect to the average absolute signal attenuation. In the following, for brevity, the normalized attenuation defined by Eq. (23) will be referred to as attenuation when no ambiguity may arise. From the definitions of Eqs. 23-25, the error on the individual A_N values can be calculated noting that

$$\frac{\iota_{p}^{k}}{\iota_{d}^{k}} = \frac{I_{p}^{k}}{I_{d}^{k}} \cdot \frac{I_{d}^{av}}{I_{p}^{av}} \tag{26}$$

where the first ratio of the right term is the relative intensity (*RI*) of the kth residue signal, i.e. the signal intensity ratio in the presence and absence of nitroxide. Based on the error propagation theory, an expression for the individual A_N error can be written as:

$$\Delta A_{N}^{k} = A_{N}^{k} \times \sqrt{\left[\frac{\Delta I_{p}^{k}}{I_{p}^{k}}\right]^{2} + \left[\frac{\Delta I_{d}^{k}}{I_{d}^{k}}\right]^{2} + \left[\frac{\frac{1}{n^{2}}\Sigma\left(\Delta I_{p}^{k}\right)^{2}}{\left(I_{p}^{av}\right)^{2}}\right] + \left[\frac{\frac{1}{n^{2}}\Sigma\left(\Delta I_{d}^{k}\right)^{2}}{\left(I_{d}^{av}\right)^{2}}\right]} \tag{27}$$

The first two terms under the square root sign represent the error on *RI* and appear in the analogous error propagation expression for this parameter where the error on the individual intensity value ($\Delta I_{p,d}^{k}$) is calculated by dividing each experimental intensity value by the specific signal-to-noise ratio as determined from the considered NMR spectrum. The other two remaining terms under the square root of Eq. (27) represent the propagation of the error on the intensity means. Expressing the error on the means in terms of intensity standard deviations, i.e. using $(\sigma^{I_{p,d}}/\sqrt{n})$ terms, appears inappropriate because NMR signal intensities and paramagnetic attenuation thereof can not be considered to distribute according to a Gaussian statistics.

4.2.4 Enhanced recovery of magnetization

The experiments were acquired at 600 MHz and 298 K with 1% H2O in D2O samples at varying Tempol concentrations (0, 10, 100 mM), by collecting 16 scans preceded by 64 dummy scans with a relaxation delay (D1) of 0.2 s. A magnetic field gradient along the z-direction was applied with a 100 μs pulse of differing strengths, i.e. 0-1% with respect to the maximum of 67 Gauss/cm. To demonstrate the Tempol-induced enhancement of the signal acquired with short relaxation delay, the sequence included a small field gradient between the pulse and the acquisition. The gradient should represent the dephasing contributed by slow or intermediate exchange processes. Expectedly, if the experiment is done comparing pure HOD and Tempol-doped HOD as a function of the gradient strength, a larger recovery should be obtained from doped HOD because of the effect of R_{1p}. The effect should increase on increasing the gradient. The results confirm the expectations.

4.2.5 Molecular dynamics simulation

The coordinates of β2m were obtained from the structure of human class I major histocompatibility complex (PDB code: 3HLA)[12]. The protonation states of titratable groups were assigned using the Bluues server available at the URL http://protein.bio.unipd.it/bluues/[175,176]. For TEMPOL the structure was built using, as a starting template, the structure of the spin label reported by Sezer et al.[177], then adapting the parameters from CHARMM forcefield with the charges assigned using the algorithm of Gasteiger and Marsili[178]. Molecular dynamics simulations were carried out with the program NAMD 2.9[179] using the Generalized Born Surface Area (GBSA) implicit solvent model[180] employing the Onufriev-Bashford-Case (OBC) model[181]. A high concentration box with 26 TEMPOL molecules arranged on a cubic grid surrounding a protein molecule was simulated imposing elastic spherical boundary conditions[182]. Four 5 ns simulations were conducted at

298 K and 310 K. Reference explicit solvent simulations were performed for 110 ns at 298 K and 310 K essentially as previously described[183]. Analysis was performed on the last 100 ns. The depth of amide protons was obtained as the generalized Born radius computed according to the GBR6 model[12,184]. The molecular surface was generated using the program MSMS[185] and the GBR6 was computed using the program Bluues[12]. For all the exposed locations listed in Table 3.1 of main text, the corresponding amide hydrogens possess average distances from the surface between 0.18 and 0.49 nm. A qualitative correlation also emerges between the extent of attenuation and the depth figure, i.e. the larger the depth, the lower the attenuation.

4.2.6 Fitting of relaxation dispersion data

The routine employed by Dynamics Center models the experimental data with the best fitting out of three different functions, depending on whether the dispersion curve is flat (independent on the effective field), or modulated by slow or fast exchange rate. In the slow exchange limit, the fitting function is[147]:

$$R_2(\tau_{CP}) = R_2^0 + k_{ex} - k_{ex}\frac{\sin(\Delta_\omega \tau_{CP})}{\Delta_\omega \tau_{CP}} \tag{28}$$

where $R_2(\tau_{CP})$ is the transverse relaxation rate determined as a function of time between the CPMG 180° pulses, τ_{CP}, R_2^0 is the transverse relaxation rate without exchange contribution, k_{ex} is the exchange rate constant, Δ_ω is the chemical shift difference between the two exchanging states. The other function used by Dynamics Center to fit relaxation dispersion data refers to the fast exchange limit[152]:

$$R_2(\tau_{CP}) = R_2^0 + \frac{\Phi_{ex}}{k_{ex}}\left[1 - \frac{2\tanh\left(\frac{k_{ex}\tau_{CP}}{2}\right)}{k_{ex}\tau_{CP}}\right]; \Phi_{ex} = p_A p_B \Delta_\omega^2 \tag{29}$$

where p_A and p_B are the fractional populations of the two exchanging states

4.3 Insights into a protein-nanoparticle system by paramagnetic perturbation NMR spectroscopy

4.3.1 Sample preparation

The uniformly ^{15}N-labelled wild-type human β2m was expressed with an additional methionine at the N-terminus (Met-0) and purified as previously reported[156]. The protein samples in the absence of AuNPs were prepared in H_2O/D_2O 95/5, 1.5 mM sodium citrate, 20 mM Hepes buffer, pH 7. The protein concentration was 8.0 μM, as determined by UV absorption at 280 nm. For solutions with AuNPs, proper amounts of D_2O and concentrated Hepes and β2m solutions were added to the mother NP suspension containing already citrate to reproduce the above-mentioned composition. Following dilution, the final AuNP concentration was 60 nM. A few microliters of concentrated Tempol solution were added when necessary to the NMR tube containing 0.550 mL of β2m, with or without AuNPs, to reach the desired Tempol/protein concentration ratio. For NMR samples, Tempol concentration was always 0.8 mM. For ESR samples, solutions at variable Tempol concentrations were prepared, i.e. 0.4 mM, 0.8 mM and 1.6 mM, in aqueous buffer (20 mM HEPES, 1.5 mM sodium citrate, pH = 7), either alone or in the presence of 8 μM β2m, or 60 nM AuNP, or 8 μM β2m + 60 nM AuNP.

4.3.2 Spectroscopy

All the spectra were acquired at 298 K. The NMR experiments were collected at 14.0 T (^{1}H at 600.19 MHz, ^{15}N at 60.82 MHz) on a Bruker Avance III NMR system equipped with triple resonance cryoprobe. Two-dimensional ^{15}N-^{1}H HSQC experiments[164] carried out using sensitivity-improved Echo/Antiecho-TPPI pure phase detection in F1, gradient coherence selection and flip-back pulse for solvent suppression[71,165,166], were acquired over spectral widths of 40 ppm and 14 ppm in F1 and F2 dimensions, respectively, with 64 time-domain points in t1, 256 or 512 scans × 2048 points in t2 and 64 dummy scans to achieve steady state. After reproducibility check, relaxation delays were set to 0.5 and 5 s, respectively for off- and on-equilibrium conditions of magnetization recovery, following the guidelines previously reported[154]. The ^{15}N longitudinal relaxation times were measured using the sequence proposed by Kay and colleagues[186] with the modifications for sensitivity enhancement and flip-back pulse for solvent suppression[71,165,166]. The spectra with 8 different relaxation intervals were acquired (10, 30, 60, 100, 140, 200, 400, 1200 ms). All NMR data were processed with TOPSPIN version 4.0.2. Prior to Fourier transformation, linear prediction in t1 (up to 128

points) and zero filling were applied to yield final data set of 2K × 1K points. For longitudinal relaxation analysis the Bruker Dynamics Center 2.5.3 routine was used.
ESR spectroscopy experiments were collected with a Bruker EMXnano spectrometer operating in the X band. Capillaries filled with 50 μL of sample solution were placed in standard 4 mm tubes and submitted to acquisition (1 scan). The ESR operating parameter were: frequency = 9.6 GHz; microwave power = 0.316 mW; modulation amplitude = 1 Gauss; modulation frequency =100 kHz; center field = 3429.8 Gauss; sweep width = 200 Gauss; time constant = 1.28 ms. The data were processed using the Bruker software package Xenon.

4.3.3 Spectroscopic data treatment

Normalized attenuation, A_N, was calculated according to Eq. 23 and the error on the individual A_N values can be calculated by using the Eq. 27.

The ESR spectra were employed to extract the rotational correlation time (τ_c) of Tempol, in absence or presence of β$_2$m or/and AuNPs. Based on the method of Knowles and colleagues[187] and Kivelson's theoretical analysis[188], the τ_c values were estimated from:

$$\tau_c = 6.5 \times 10^{-10} \Delta B_0 \left[\left(\frac{h_0}{h_{-1}}\right)^{\frac{1}{2}} - 1\right] \tag{30}$$

where ΔB_0 is the linewidth of the of the central line of the nitroxide ESR signal (a triplet because of the hyperfine coupling with the ^{14}N nuclear spin), and $h_{0/-1}$ are the amplitudes of the central and upfield lines. The corresponding error was calculated from Eq. 31 by error propagation of the experimental uncertainties on linewidth ($\Delta\Delta B_0$) and amplitudes ($\Delta h_{0/-1}$), according to:

$$\Delta\tau_c = 6.5 \times 10^{-10} \left\{\left[\left(\frac{h_0}{h_{-1}}\right)^{\frac{1}{2}} - 1\right] \Delta\Delta B_0 + \frac{\Delta B_0}{2(h_{-1})^{\frac{1}{2}}(h_0)^{\frac{1}{2}}} \Delta h_0 + \frac{\Delta B_0 (h_0)^{\frac{1}{2}}}{2(h_{-1})^{\frac{3}{2}}} \Delta h_{-1}\right\} \tag{31}$$

4.4 Self-association study of β2-Microglobuline mutant D76N by paramagnetic perturbation NMR spectroscopy

^{15}N-uniformly labelled D76N β$_2$M was expressed with and additional methionine at the N-terminus (Met-0) and purified from transformed E. coli[25]. The D76N β$_2$M stock sample were prepared in H2O/D2O 95/5, 66.5 mM phosphate buffer, 95 mM NaCl, pH 7 and protein concentration was measured by UV absorption spectroscopy at 280 nm. 4- hydroxy-2,2,6,6-tetramethyl-piperidine-l-oxyl (Tempol) was purchased from Sigma-Aldrich.

4.4.1 ESR Spectroscopy

ESR spectroscopy experiments were collected with a Bruker EMXnano spectrometer at different Tempol concentrations 1.6mM prepared in aqueous buffer (66.5 mM phosphate buffer, 95 mM NaCl, pH 7), either alone or in the presence of 220 μM D76N β$_2$m mixture. Capillaries filled with 50 μL of each solution were placed in standard 4 mm tubes and submitted to acquisition (1 scans). The ESR operating parameter were: frequency = 9.6 GHz; microwave power = 0.316 mW; modulation amplitude = 1 Gauss; modulation frequency =100 kHz; center field = 3429.8 Gauss; sweep width = 200 Gauss; time constant = 1.28 ms. The data were processed using the Bruker software package Xenon.

4.4.2 NMR Spectroscopy

NMR samples were prepared by diluting the stock D76N β$_2$M solution to get final concentration 220 μM and 4 μM by 66.5 mM phosphate buffer, 95 mM NaCl, pH 7. NMR spectra were collected at 14.0 T (^{1}H resonance at 600.13 MHz) on the Bruker Avance III spectrometer equipped with triple resonance and triple axis gradient cryoprobe. 2D ^{15}N-^{1}H HSQC[163], carried out via double INEPT transfer, sensitivity- improved Echo/Antiecho-TPPI pure phase detection in F1, gradient coherence selection and flip-back pulse for solvent suppression, spectra were recorded over spectral widths of 40 ppm (^{15}N, t_1) and 16 ppm (^{1}H, t_2), and digitized over 64 and 2048 points, respectively. For each t_1 dimension point, 512 scans were accumulated and always 64 dummy scans to achieve steady state. Different relaxation delays were used to acquire the data, 0.5s and 4s at 298K as mentioned in our previous work[154].

All NMR data were processed with TOPSPIN version 4.0.2. Prior to Fourier transformation, linear prediction in t1 (up to 160 points) and zero filling were applied to yield final data set of 2K x 1K points.

Diffusion coefficients were measured by using pseudo 2D ^{1}H DSTEBPP (Double Stimulated Echo BiPolar Pulse) experiment[161]. Protein concentrations were 4 μM, 25 μM, 50 μM, and 100 μM in 66.5 mM phosphate buffer, 95 mM NaCl, pH 7. The gradient strength along z-axis was varied with a squared ramp from 10 to 90 % of its maximum value (~ 60 G/ cm) and digitized over 40 along t_1 dimension and 2048 along t_2 dimension. 512 scans per gradient increment were collected. Water suppression was done by pair of WATERGATE[168] elements in the excitation-sculpting mode[169] attached to DSTEBPP. Bruker software Dynamic Centre is used to extract the diffusion coefficient.

4.4.3 Attenuation calculation

Normalized attenuation, A_N, was calculated according to Eq. 23 and the error on the individual A_N values can be calculated by using the Eq. 27

5. REFERENCES

1 N. H. Joh, A. Oberai, D. Yang, J. P. Whitelegge and J. U. Bowie, Similar energetic contributions of packing in the core of membrane and water-soluble proteins, *J. Am. Chem. Soc.*, 2009, **131**, 10846–10847.

2 D. Mallamace, E. Fazio, F. Mallamace and C. Corsaro, *Int. J. Mol. Sci.*, 2018, 19.

3 L. Lins and R. Brasseur, The hydrophobic effect in protein folding, *FASEB J.*, 1995, **9**, 535–540.

4 F. U. Hartl and M. Hayer-Hartl, *Nat. Struct. Mol. Biol.*, 2009, 16, 574–581.

5 J. N. Onuchic, Z. Luthey-Schulten and P. G. Wolynes, Theory of Protein Folding: The Energy Landscape Perspective, *Annu. Rev. Phys. Chem.*, 1997, **48**, 545–600.

6 M. Biancalana and S. Koide, *Biochim. Biophys. Acta - Proteins Proteomics*, 2010, 1804, 1405–1412.

7 T. K. Karamanos, A. P. Kalverda, G. S. Thompson and S. E. Radford, *Prog. Nucl. Magn. Reson. Spectrosc.*, 2015, 88–89, 86–104.

8 B. A. Cunningham, J. L. Wang, I. Berggård and P. A. Peterson, The Complete Amino Acid Sequence of β2-Microglobulin, *Biochemistry*, 1973, **12**, 4811–4822.

9 D. Güssow, R. Rein, I. Ginjaar, F. Hochstenbach, G. Seemann, A. Kottman and H. L. Ploegh, The human beta 2-microglobulin gene. Primary structure and definition of the transcriptional unit., *J. Immunol.*, 1987, **139**, 3132 LP – 3138.

10 F. Gejyo, T. Yamada, S. Odani, Y. Nakagawa, M. Arakawa, T. Kunitomo, H. Kataoka, M. Suzuki, Y. Hirasawa, T. Shirahama, A. S. Cohen and K. Schmid, A new form of amyloid protein associated with chronic hemodialysis was identified as β2-microglobulin, *Biochem. Biophys. Res. Commun.*, 1985, **129**, 701–706.

11 J. Floege, A. Bartsch, M. Schulze, S. Shaldon, K. M. Koch and L. C. Smeby, Clearance and synthesis rates of β2-microglobulin in patients undergoing hemodialysis and in normal subjects, *J. Lab. Clin. Med.*, 1991, **118**, 153–165.

12 P. J. Bjorkman, M. A. Saper, B. Samraoui, W. S. Bennett, J. L. Strominger and D. C. Wiley, Structure of the human class I histocompatibility antigen, HLA-A2, *Nature*, 1987, **329**, 506–512.

13 G. Verdone, A. Corazza, P. Viglino, F. Pettirossi, S. Giorgetti, P. Mangione, A. Andreola, M. Stoppini, V. Bellotti and G. Esposito, The solution structure of human β2-microglobulin reveals the prodromes of its amyloid transition, *Protein Sci.*, 2002, **11**,

487–499.

14 M. A. Saper, P. J. Bjorkman and D. C. Wiley, Refined structure of the human histocompatibility antigen HLA-A2 at 2.6 Å resolution, *J. Mol. Biol.*, 1991, **219**, 277–319.

15 C. H. Trinh, D. P. Smith, A. P. Kalverda, S. E. V. Phillips and S. E. Radford, Crystal structure of monomeric human β2-microglobulin reveals clues to its amyloidogenic properties, *Proc. Natl. Acad. Sci. U. S. A.*, 2002, **99**, 9771–9776.

16 G. Esposito, S. Ricagno, A. Corazza, E. Rennella, D. Gümral, M. C. Mimmi, E. Betto, C. E. M. Pucillo, F. Fogolari, P. Viglino, S. Raimondi, S. Giorgetti, B. Bolognesi, G. Merlini, M. Stoppini, M. Bolognesi and V. Bellotti, The Controlling Roles of Trp60 and Trp95 in β2-Microglobulin Function, Folding and Amyloid Aggregation Properties, *J. Mol. Biol.*, 2008, **378**, 887–897.

17 H. Naiki, N. Hashimoto, S. Suzuki, H. Kimura, K. Nakakuki and F. Gejyo, Establishment of a kinetic model of dialysis-related amyloid fibril extension in vitro, *Amyloid*, 1997, **4**, 223–232.

18 T. Eichner and S. E. Radford, A Generic Mechanism of β2-Microglobulin Amyloid Assembly at Neutral pH Involving a Specific Proline Switch, *J. Mol. Biol.*, 2009, **386**, 1312–1326.

19 F. Chiti, P. Mangione, A. Andreola, S. Giorgetti, M. Stefani, C. M. Dobson, V. Bellotti and N. Taddei, Detection of two partially structured species in the folding process of the amyloidogenic protein β2-microglobulin, *J. Mol. Biol.*, 2001, **307**, 379–391.

20 G. Esposito, A. Corazza and V. Bellotti, *Protein Aggregation and Fibrillogenesis in Cerebral and Systemic Amyloid Disease*, Subcellular Biochemistry, 2012, vol. 65.

21 H. Smith, N. Guthertz, E. Cawood, R. Maya-Martinez, A. Breeze and S. Radford, The role of the IT-state in D76N β2-microglobulin amyloid assembly: a crucial intermediate or an innocuous bystander?, *J. Biol. Chem.*, 2020, **295**, jbc.RA120.014901.

22 J. Villanueva, M. Hoshino, H. Katou, J. Kardos, K. Hasegawa, H. Naiki and Y. Goto, Increase in the conformational flexibility of β2-microglobulin upon copper binding: A possible role for copper in dialysis-related amyloidosis, *Protein Sci.*, 2004, **13**, 797–809.

23 H. Katou, T. Kanno, M. Hoshino, Y. Hagihara, H. Tanaka, T. Kawai, K. Hasegawa, H. Naiki and Y. Goto, The role of disulfide bond in the amyloidogenic state of β2-microglobulin studied by heteronuclear NMR, *Protein Sci.*, 2002, **11**, 2218–2229.

24 K. Sakurai, A. Maeno, Y. H. Lee and K. Akasaka, Conformational Properties Relevant to the Amyloidogenicity of β2 -Microglobulin Analyzed Using Pressure- and Salt-

Dependent Chemical Shift Data, *J. Phys. Chem. B*, 2019, **123**, 836–844.

25 S. Valleix, J. D. Gillmore, F. Bridoux, P. P. Mangione, A. Dogan, B. Nedelec, M. Boimard, G. Touchard, J.-M. Goujon, C. Lacombe, P. Lozeron, D. Adams, C. Lacroix, T. Maisonobe, V. Planté-Bordeneuve, J. A. Vrana, J. D. Theis, S. Giorgetti, R. Porcari, S. Ricagno, M. Bolognesi, M. Stoppini, M. Delpech, M. B. Pepys, P. N. Hawkins and V. Bellotti, Hereditary Systemic Amyloidosis Due to Asp76Asn Variant β2-Microglobulin, *N. Engl. J. Med.*, 2012, **366**, 2276–2283.

26 P. P. Mangione, G. Esposito, A. Relini, S. Raimondi, R. Porcari, S. Giorgetti, A. Corazza, F. Fogolari, A. Penco, Y. Goto, Y. H. Lee, H. Yagi, C. Cecconi, M. M. Naqvi, J. D. Gillmore, P. N. Hawkins, F. Chiti, R. Rolandi, G. W. Taylor, M. B. Pepys, M. Stoppini and V. Bellotti, Structure, folding dynamics, and amyloidogenesis of D76N β2-microglobulin: roles of shear flow, hydrophobic surfaces, and α-crystallin, *J. Biol. Chem.*, 2013, **288**, 30917–30930.

27 S. H. Chong, J. Hong, S. Lim, S. Cho, J. Lee and S. Ham, Structural and Thermodynamic Characteristics of Amyloidogenic Intermediates of β-2-Microglobulin, *Sci. Rep.*, 2015, **5**, 1–9.

28 R. J. S. Loureiro, D. Vila-Viçosa, M. Machuqueiro, E. I. Shakhnovich and P. F. N. Faísca, A tale of two tails: The importance of unstructured termini in the aggregation pathway of β2-microglobulin, *Proteins Struct. Funct. Bioinforma.*, 2017, **85**, 2045–2057.

29 C. Camilloni, B. M. Sala, P. Sormanni, R. Porcari, A. Corazza, M. De Rosa, S. Zanini, A. Barbiroli, G. Esposito, M. Bolognesi, V. Bellotti, M. Vendruscolo and S. Ricagno, Rational design of mutations that change the aggregation rate of a protein while maintaining its native structure and stability, *Sci. Rep.*, 2016, **6**, 1–11.

30 T. Le Marchand, M. De Rosa, N. Salvi, B. M. Sala, L. B. Andreas, E. Barbet-Massin, P. Sormanni, A. Barbiroli, R. Porcari, C. Sousa Mota, D. De Sanctis, M. Bolognesi, L. Emsley, V. Bellotti, M. Blackledge, C. Camilloni, G. Pintacuda and S. Ricagno, Conformational dynamics in crystals reveal the molecular bases for D76N beta-2 microglobulin aggregation propensity, *Nat. Commun.*, 2018, **9**, 1–11.

31 G. Esposito, A. Corazza, P. Viglino, G. Verdone, F. Pettirossi, F. Fogolari, A. Makek, S. Giorgetti, P. Mangione, M. Stoppini and V. Bellotti, Solution structure of β2-microglobulin and insights into fibrillogenesis, *Biochim. Biophys. Acta - Proteins Proteomics*, 2005, **1753**, 76–84.

32 G. Brancolini, A. Corazza, M. Vuano, F. Fogolari, M. C. Mimmi, V. Bellotti, M.

Stoppini, S. Corni and G. Esposito, Probing the influence of citrate-capped gold nanoparticles on an amyloidogenic protein, *ACS Nano*, 2015, **9**, 2600–2613.

33 G. Brancolini, M. C. Maschio, C. Cantarutti, A. Corazza, F. Fogolari, V. Bellotti, S. Corni and G. Esposito, Citrate stabilized gold nanoparticles interfere with amyloid fibril formation: D76N and ΔN6 β2-microglobulin variants, *Nanoscale*, 2018, **10**, 4793–4806.

34 C. Cantarutti, S. Raimondi, G. Brancolini, A. Corazza, S. Giorgetti, M. Ballico, S. Zanini, G. Palmisano, P. Bertoncin, L. Marchese, P. Patrizia Mangione, V. Bellotti, S. Corni, F. Fogolari and G. Esposito, Citrate-stabilized gold nanoparticles hinder fibrillogenesis of a pathological variant of β2-microglobulin, *Nanoscale*, 2017, **9**, 3941–3951.

35 C. Cantarutti, P. Bertoncin, A. Corazza, S. Giorgetti, P. Mangione, V. Bellotti, F. Fogolari and G. Esposito, Short-Chain Alkanethiol Coating for Small-Size Gold Nanoparticles Supporting Protein Stability, *Magnetochemistry*, 2017, **3**, 40.

36 S. Linse, C. Cabaleiro-Lago, W. F. Xue, I. Lynch, S. Lindman, E. Thulin, S. E. Radford and K. A. Dawson, Nucleation of protein fibrillation by nanoparticles, *Proc. Natl. Acad. Sci. U. S. A.*, 2007, **104**, 8691–8696.

37 C. Cantarutti, P. Bertoncin, P. Posocco, Y. Hunashal, S. Giorgetti, V. Bellotti, F. Fogolari and G. Esposito, The interaction of β2-microglobulin with gold nanoparticles: Impact of coating, charge and size, *J. Mater. Chem. B*, 2018, **6**, 5964–5974.

38 L. Callewaert and C. W. Michiels, *J. Biosci.*, 2010, 35, 127–160.

39 L. G and K. J, *Bioactive egg compounds*, Springer Berlin Heidelberg, 1st edn., 2007.

40 R. Mishra, K. Sörgjerd, S. Nyström, A. Nordigården, Y. C. Yu and P. Hammarström, Lysozyme Amyloidogenesis Is Accelerated by Specific Nicking and Fragmentation but Decelerated by Intact Protein Binding and Conversion, *J. Mol. Biol.*, 2007, **366**, 1029–1044.

41 P. Jollès and J. Jollès, *Mol. Cell. Biochem.*, 1984, 63, 165–189.

42 L. N. Johnson, J. Cheetham, P. J. McLaughlin, K. R. Acharya, D. Barford and D. C. Phillips, *Curr. Top. Microbiol. Immunol.*, 1988, 139, 81–134.

43 C. M. Dobson, P. A. Evans and S. E. Radford, Understanding how proteins fold: the lysozyme story so far, *Trends Biochem. Sci.*, 1994, **19**, 31–37.

44 M. Buck, J. Boyd, C. Redfield, D. A. MacKenzie, D. J. Jeenes, D. B. Archer and C. M. Dobson, Structural Determinants of Protein Dynamics: Analysis of 15N NMR Relaxation Measurements for Main-Chain and Side-Chain Nuclei of Hen Egg White Lysozyme, *Biochemistry*, 1995, **34**, 4041–4055.

45 L. J. Smith, A. E. Mark, C. M. Dobson and W. F. van Gunsteren, Comparison of MD Simulations and NMR Experiments for Hen Lysozyme. Analysis of Local Fluctuations, Cooperative Motions, and Global Changes, *Biochemistry*, 1995, **34**, 10918–10931.

46 C. C. F. Blake, D. F. Koenig, G. A. Mair, A. C. T. North, D. C. Phillips and V. R. Sarma, Structure of hen egg-white lysozyme: A three-dimensional Fourier synthesis at 2 Å resolution, *Nature*, 1965, **206**, 757–761.

47 L. J. Smith, M. J. Sutcliffe, C. Redfield and C. M. Dobson, Structure of hen lysozyme in solution, *J. Mol. Biol.*, 1993, **229**, 930–944.

48 H. Schwalbe, S. B. Grimshaw, A. Spencer, M. Buck, J. Boyd, C. M. Dobson, C. Redfield and L. J. Smith, A refined solution structure of hen lysozyme determined using residual dipolar coupling data, *Protein Sci.*, 2001, **10**, 677–688.

49 W. Kabsch and C. Sander, Dictionary of protein secondary structure: Pattern recognition of hydrogen-bonded and geometrical features, *Biopolymers*, 1983, **22**, 2577–2637.

50 L. A. Morozova-Roche, J. Zurdo, A. Spencer, W. Noppe, V. Receveur, D. B. Archer, M. Joniau and C. M. Dobson, Amyloid fibril formation and seeding by wild-type human lysozyme and its disease-related mutational variants, *J. Struct. Biol.*, 2000, **130**, 339–351.

51 S. Goda, K. Takano, K. Yutani, Y. Yamagata, R. Nagata, H. Akutsu, S. Maki and K. Namba, Amyloid protofilament formation of hen egg lysozyme in highly concentrated ethanol solution, *Protein Sci.*, 2000, **9**, 369–375.

52 U. Stocker, K. Spiegel and W. F. Van Gunsteren, On the similarity of properties in solution or in the crystalline state: A molecular dynamics study of hen lysozyme, *J. Biomol. NMR*, 2000, **18**, 1–12.

53 S. Ravichandran, J. D. Madura and J. Talbot, A Brownian dynamics study of the initial stages of hen egg-white lysozyme adsorption at a solid interface, *J. Phys. Chem. B*, 2001, **105**, 3610–3613.

54 F. Carlsson, M. Malmsten and P. Linse, Monte Carlo simulations of lysozyme self-association in aqueous solution, *J. Phys. Chem. B*, 2001, **105**, 12189–12195.

55 M. Gottschalk and B. Halle, Self-association of lysozyme as seen by magnetic relaxation dispersion, *J. Phys. Chem. B*, 2003, **107**, 7914–7922.

56 W. S. Price, F. Tsuchiya and Y. Arata, Time dependence of aggregation in crystallizing lysozyme solutions probed using NMR self-diffusion measurements, *Biophys. J.*, 2001, **80**, 1585–1590.

57 M. Muschol and F. Rosenberger, Interactions in undersaturated and supersaturated

lysozyme solutions: Static and dynamic light scattering results, *J. Chem. Phys.*, 1995, **103**, 10424–10432.

58 D. E. Kuehner, C. Heyer, C. Rämsch, U. M. Fornefeld, H. W. Blanch and J. M. Prausnitz, Interactions of lysozyme in concentrated electrolyte solutions from dynamic light-scattering measurements, *Biophys. J.*, 1997, **73**, 3211–3224.

59 E. Ermakova, Lysozyme dimerization: brownian dynamics simulation, *J. Mol. Model.*, 2005, **12**, 34–41.

60 J. D. Bryngelson, J. N. Onuchic, N. D. Socci and P. G. Wolynes, Funnels, pathways, and the energy landscape of protein folding: A synthesis, *Proteins Struct. Funct. Bioinforma.*, 1995, **21**, 167–195.

61 J. D. Bryngelson and P. G. Wolynes, Spin glasses and the statistical mechanics of protein folding., *Proc. Natl. Acad. Sci. U. S. A.*, 1987, **84**, 7524–7528.

62 G. M. Clore and A. M. Gronenborn, New methods of structure refinement for macromolecular structure determination by NMR, *Proc. Natl. Acad. Sci. U. S. A.*, 1998, **95**, 5891–5898.

63 N. Tjandra, J. Marquardt and G. M. Clore, Direct Refinement against Proton-Proton Dipolar Couplings in NMR Structure Determination of Macromolecules, *J. Magn. Reson.*, 2000, **142**, 393–396.

64 G. Marius Clore and J. Iwahara, Theory, practice, and applications of paramagnetic relaxation enhancement for the characterization of transient low-population states of biological macromolecules and their complexes, *Chem. Rev.*, 2009, **109**, 4108–4139.

65 I. Bertini, C. Luchinat and M. Piccioli, in *Methods in Enzymology*, Academic Press Inc., 2001, vol. 339, pp. 314–340.

66 P. H. J. Keizers and M. Ubbink, Paramagnetic tagging for protein structure and dynamics analysis, *Prog. Nucl. Magn. Reson. Spectrosc.*, 2011, **58**, 88–96.

67 G. Otting, Protein NMR Using Paramagnetic Ions, *Annu. Rev. Biophys.*, 2010, **39**, 387–405.

68 K. Pervushin, R. Riek, G. Wider and K. Wüthrich, Attenuated T2 relaxation by mutual cancellation of dipole-dipole coupling and chemical shift anisotropy indicates an avenue to NMR structures of very large biological macromolecules in solution, *Proc. Natl. Acad. Sci. U. S. A.*, 1997, **94**, 12366–12371.

69 G. M. Clore, P. C. Driscoll, A. M. Gronenborn and P. T. Wingfield, Analysis of the Backbone Dynamics of Interleukin-1β Using Two-Dimensional Inverse Detected Heteronuclear 15N-1H NMR Spectroscopy, *Biochemistry*, 1990, **29**, 7387–7401.

70 R. Ishima and D. A. Torchia, *Nat. Struct. Biol.*, 2000, 7, 740–743.

71 L. E. Kay, D. A. Torchia and A. Bax, Backbone Dynamics of Proteins As Studied by 15N Inverse Detected Heteronuclear NMR Spectroscopy: Application to Staphylococcal Nuclease, *Biochemistry*, 1989, **28**, 8972–8979.

72 J. W. Peng and G. Wagner, Investigation of protein motions via relaxation measurements, *Methods Enzymol.*, 1994, **239**, 563–596.

73 J. Xia, N. J. Deng and R. M. Levy, NMR relaxation in proteins with fast internal motions and slow conformational exchange: Model-free framework and markov state simulations, *J. Phys. Chem. B*, 2013, **117**, 6625–6634.

74 N. A. Farrow, O. Zhang, A. Szabo, D. A. Torchia and L. E. Kay, Spectral density function mapping using 15N relaxation data exclusively, *J. Biomol. NMR*, 1995, **6**, 153–162.

75 J. W. Peng and G. Wagner, Frequency Spectrum of NH Bonds in Eglin c from Spectral Density Mapping at Multiple Fields, *Biochemistry*, 1995, **34**, 16733–16752.

76 J. F. Lefèvre, K. T. Dayie, J. W. Peng and G. Wagner, Internal mobility in the partially folded DNA binding and dimerization domains of GAL4: NMR analysis of the N-H spectral density functions, *Biochemistry*, 1996, **35**, 2674–2686.

77 T. I. Igumenova, K. K. Frederick and A. J. Wand, *Chem. Rev.*, 2006, 106, 1672–1699.

78 A. M. Ruschak and L. E. Kay, *J. Biomol. NMR*, 2010, 46, 75–87.

79 H. Y. Carr and E. M. Purcell, Effects of diffusion on free precession in nuclear magnetic resonance experiments, *Phys. Rev.*, 1954, **94**, 630–638.

80 S. Meiboom and D. Gill, Modified spin-echo method for measuring nuclear relaxation times, *Rev. Sci. Instrum.*, 1958, **29**, 688–691.

81 D. M. Korzhnev and L. E. Kay, *Acc. Chem. Res.*, 2008, 41, 442–451.

82 A. Mittermaier and L. E. Kay, *Science (80-.).*, 2006, 312, 224–228.

83 A. G. Palmer, C. D. Kroenke and J. P. Loria, in *Methods in Enzymology*, Academic Press Inc., 2001, vol. 339, pp. 204–238.

84 B. D. Nageswara Rao, Nuclear magnetic resonance line-shape analysis and determination of exchange rates, *Methods Enzymol.*, 1989, **176**, 279–311.

85 O. F. Lange, N. A. Lakomek, C. Farès, G. F. Schröder, K. F. A. Walter, S. Becker, J. Meiler, H. Grubmüller, C. Griesinger and B. L. De Groot, Recognition dynamics up to microseconds revealed from an RDC-derived ubiquitin ensemble in solution, *Science (80-.).*, 2008, **320**, 1471–1475.

86 M. M. G. Krishna, L. Hoang, Y. Lin and S. W. Englander, Hydrogen exchange methods

to study protein folding, *Methods*, 2004, **34**, 51–64.

87 Y. Bai, *Chem. Rev.*, 2006, 106, 1757–1768.

88 N. L. Fawzi, J. Ying, D. A. Torchia and G. M. Clore, Kinetics of amyloid β monomer-to-oligomer exchange by NMR relaxation, *J. Am. Chem. Soc.*, 2010, **132**, 9948–9951.

89 P. Vallurupalli, G. Bouvignies and L. E. Kay, Studying ‘invisible’ excited protein states in slow exchange with a major state conformation, *J. Am. Chem. Soc.*, 2012, **134**, 8148–8161.

90 G. Wider, D. Neri and K. Wüthrich, Studies of slow conformational equilibria in macromolecules by exchange of heteronuclear longitudinal 2-spin-order in a 2D difference correlation experiment, *J. Biomol. NMR*, 1991, **1**, 93–98.

91 D. Sahu, G. M. Clore and J. Iwahara, TROSY-based z-exchange spectroscopy: Application to the determination of the activation energy for intermolecular protein translocation between specific sites on different DNA molecules, *J. Am. Chem. Soc.*, 2007, **129**, 13232–13237.

92 N. A. Farrow, O. Zhang, J. D. Forman-Kay and L. E. Kay, A heteronuclear correlation experiment for simultaneous determination of 15N longitudinal decay and chemical exchange rates of systems in slow equilibrium, *J. Biomol. NMR*, 1994, **4**, 727–734.

93 P. Schanda and B. Brutscher, Very fast two-dimensional NMR spectroscopy for real-time investigation of dynamic events in proteins on the time scale of seconds, *J. Am. Chem. Soc.*, 2005, **127**, 8014–8015.

94 N. J. Anthis and G. M. Clore, The length of the calmodulin linker determines the extent of transient interdomain association and target affinity, *J. Am. Chem. Soc.*, 2013, **135**, 9648–9651.

95 N. J. Anthis, M. Doucleff and G. M. Marius Clore, Transient, sparsely populated compact states of apo and calcium-loaded calmodulin probed by paramagnetic relaxation enhancement: Interplay of conformational selection and induced fit, *J. Am. Chem. Soc.*, 2011, **133**, 18966–18974.

96 Q. Bashir, A. N. Volkov, G. M. Ullmann and M. Ubbink, Visualization of the encounter ensemble of the transient electron transfer complex of cytochrome c and cytochrome c peroxidase, *J. Am. Chem. Soc.*, 2010, **132**, 241–247.

97 I. Bertini, C. Luchinat, M. Nagulapalli, G. Parigi and E. Ravera, Paramagnetic relaxation enhancement for the characterization of the conformational heterogeneity in two-domain proteins, *Phys. Chem. Chem. Phys.*, 2012, **14**, 9149–9156.

98 N. L. Fawzi, M. Doucleff, J. Y. Suh and G. M. Clore, Mechanistic details of a protein-

protein association pathway revealed by paramagnetic relaxation enhancement titration measurements, *Proc. Natl. Acad. Sci. U. S. A.*, 2010, **107**, 1379–1384.

99 I. Solomon, Relaxation processes in a system of two spins, *Phys. Rev.*, 1955, **99**, 559–565.

100 N. Bloembergen and L. O. Morgan, Proton relaxation times in paramagnetic solutions. Effects of electron spin relaxation, *J. Chem. Phys.*, 1961, **34**, 842–850.

101 A. Bernini, V. Venditti, O. Spiga and N. Niccolai, *Prog. Nucl. Magn. Reson. Spectrosc.*, 2009, 54, 278–289.

102 I. Bertini, C. Luchinat, G. Parigi and R. Pierattelli, *ChemBioChem*, 2005, 6, 1536–1549.

103 J. Iwahara, C. D. Schwieters and G. M. Clore, Ensemble Approach for NMR Structure Refinement against 1H Paramagnetic Relaxation Enhancement Data Arising from a Flexible Paramagnetic Group Attached to a Macromolecule, *J. Am. Chem. Soc.*, 2004, **126**, 5879–5896.

104 G. Pintacuda, A. Kaikkonen and G. Otting, Modulation of the distance dependence of paramagnetic relaxation enhancements by CSA×DSA cross-correlation, *J. Magn. Reson.*, 2004, **171**, 233–243.

105 M. Gueron, Nuclear relaxation in macromolecules by paramagnetic ions: a novel mechanism, *J. Magn. Reson.*, 1975, **19**, 58–66.

106 J. Iwahara, C. Tang and G. Marius Clore, Practical aspects of 1H transverse paramagnetic relaxation enhancement measurements on macromolecules, *J. Magn. Reson.*, 2007, **184**, 185–195.

107 L. P. Hwang and J. H. Freed, Dynamic effects of pair correlation functions on spin relaxation by translational diffusion in liquids, *J. Chem. Phys.*, 1975, **63**, 4017–4025.

108 I. Solomon and N. Bloembergen, Nuclear magnetic interactions in the HF molecule, *J. Chem. Phys.*, 1956, **25**, 261–266.

109 B. Liang, J. H. Bushweller and L. K. Tamm, Site-directed parallel spin-labeling and paramagnetic relaxation enhancement in structure determination of membrane proteins by solution NMR spectroscopy, *J. Am. Chem. Soc.*, 2006, **128**, 4389–4397.

110 S. Wang, R. A. Munro, S. Y. Kim, K. H. Jung, L. S. Brown and V. Ladizhansky, Paramagnetic relaxation enhancement reveals oligomerization interface of a membrane protein, *J. Am. Chem. Soc.*, 2012, **134**, 16995–16998.

111 K. D. Kopple, A. M. Petros and L. Mueller, NMR Identification of Protein Surfaces Using Paramagnetic Probes, *Biochemistry*, 1990, **29**, 10041–10048.

112 N. Niccolai, G. Valensin, C. Rossi and W. A. Gibbons, The Stereochemistry and

Dynamics of Natural Products and Biopolymers from Proton Relaxation Spectroscopy: Spin-Label Delineation of Inner and Outer Protons of Gramicidin S Including Hydrogen Bonds, *J. Am. Chem. Soc.*, 1982, **104**, 1534–1537.

113 N. Niccolai, C. Rossi, G. Valensin, P. Mascagni and W. A. Gibbons, An investigation of the mechanisms of nitroxide-induced proton relaxation enhancements in biopolymers, *J. Phys. Chem.*, 1984, **88**, 5689–5692.

114 H. Molinari, G. Esposito, L. Ragona, M. Pegna, N. Niccolai, R. M. Brunne, A. M. Lesk and L. Zetta, Probing protein structure by solvent perturbation of NMR spectra: The surface accessibility of bovine pancreatic trypsin inhibitor, *Biophys. J.*, 1997, **73**, 382–396.

115 D. D. Boehr, D. McElheny, H. J. Dyson and P. E. Wrightt, The dynamic energy landscape of dihydrofolate reductase catalysis, *Science (80-.).*, 2006, **313**, 1638–1642.

116 G. Bhabha, J. Lee, D. C. Ekiert, J. Gam, I. A. Wilson, H. J. Dyson, S. J. Benkovic and P. E. Wright, A dynamic knockout reveals that conformational fluctuations influence the chemical step of enzyme catalysis, *Science (80-.).*, 2011, **332**, 234–238.

117 K. Sugase, H. J. Dyson and P. E. Wright, Mechanism of coupled folding and binding of an intrinsically disordered protein, *Nature*, 2007, **447**, 1021–1025.

118 E. Walinda, D. Morimoto and K. Sugase, *Methods*, 2018, 148, 28–38.

119 J. P. Carver and R. E. Richards, A general two-site solution for the chemical exchange produced dependence of T2 upon the carr-Purcell pulse separation, *J. Magn. Reson.*, 1972, **6**, 89–105.

120 A. G. Palmer, C. D. Kroenke and J. P. Loria, in *Methods in Enzymology*, Academic Press Inc., 2001, vol. 339, pp. 204–238.

121 R. Ishima and D. A. Torchia, Estimating the time scale of chemical exchange of proteins from measurements of transverse relaxation rates in solution, *J. Biomol. NMR*, 1999, **14**, 369–372.

122 D. G. Davis, M. E. Perlman and R. E. London, Direct Measurements of the Dissociation-Rate Constant for Inhibitor-Enzyme Complexes via the T1ρ and T2 (CPMG) Methods, *J. Magn. Reson. Ser. B*, 1994, **104**, 266–275.

123 C. Deverell, R. E. Morgan and J. H. Strange, Studies of chemical exchange by nuclear magnetic relaxation in the rotating frame, *Mol. Phys.*, 1970, **18**, 553–559.

124 S. Meiboom, Nuclear magnetic resonance study of the proton transfer in water, *J. Chem. Phys.*, 1961, **34**, 375–388.

125 A. G. Palmer, Chemical exchange in biomacromolecules: Past, present, and future, *J.*

Magn. Reson., 2014, **241**, 3–17.

126 D. Ban, A. D. Gossert, K. Giller, S. Becker, C. Griesinger and D. Lee, Exceeding the limit of dynamics studies on biomolecules using high spin-lock field strengths with a cryogenically cooled probehead, *J. Magn. Reson.*, 2012, **221**, 1–4.

127 A. L. Hansen, E. N. Nikolova, A. Casiano-Negroni and H. M. Al-Hashimi, Extending the range of microsecond-to-millisecond chemical exchange Detected in labeled and unlabeled nucleic acids by selective carbon R1 (rho) NMR spectroscopy, *J. Am. Chem. Soc.*, 2009, **131**, 3818–3819.

128 P. Lundström and M. Akke, Microsecond Protein Dynamics Measured by 13Cα Rotating-Frame Spin Relaxation, *ChemBioChem*, 2005, **6**, 1685–1692.

129 B. J. Grant, A. A. Gorfe and J. A. McCammon, *Curr. Opin. Struct. Biol.*, 2010, 20, 142–147.

130 G. Bhabha, D. C. Ekiert, M. Jennewein, C. M. Zmasek, L. M. Tuttle, G. Kroon, H. J. Dyson, A. Godzik, I. A. Wilson and P. E. Wright, Divergent evolution of protein conformational dynamics in dihydrofolate reductase, *Nat. Struct. Mol. Biol.*, 2013, **20**, 1243–1249.

131 J. S. Fraser, M. W. Clarkson, S. C. Degnan, R. Erion, D. Kern and T. Alber, Hidden alternative structures of proline isomerase essential for catalysis, *Nature*, 2009, **462**, 669–673.

132 A. G. Palmer and F. Massi, *Chem. Rev.*, 2006, 106, 1700–1719.

133 G. Esposito, A. M. Lesk, H. Molinari, A. Motta, N. Niccolai and A. Pastore, Probing protein structure by solvent perturbation of nuclear magnetic resonance spectra, *J. Mol. Biol.*, 1992, **224**, 659–670.

134 N. Neri, B. Alessandra, R. Mauro, M. Scarselli, N. Paolo, E. Gennaro, M. Paolo, M. Andrea and M. Henríette, NMR delineation of inner and outer protons from paramagnetic relaxation perturbations in 1 D and 2D spectra of peptides, *J. Chem. Soc. Perkin Trans. 2*, 1991, 1453–1457.

135 M. Scarselli, A. Bernini, C. Segoni, H. Molinari, G. Esposito, A. M. Lesk, F. Laschi, P. Temussi and N. Niccolai, Tendamistat surface accessibility to the TEMPOL paramagnetic probe, *J. Biomol. NMR*, 1999, **15**, 125–133.

136 N. Niccolai, A. Ciutti, O. Spiga, M. Scarselli, A. Bernini, L. Bracci, D. Di Maro, C. Dalvit, H. Molinari, G. Esposito and P. A. Temussi, NMR Studies of Protein Surface Accessibility, *J. Biol. Chem.*, 2001, **276**, 42455–42461.

137 P. S. Hubbard, Theory of electron-nucleus Overhauser effects in liquids containing free

radicals, *Proc. R. Soc. London. Ser. A. Math. Phys. Sci.*, 1966, **291**, 537–555.

138 R. A. Dwek, *Nuclear Magnetic Resonance in Biochemistry: Applications to Enzyme Systems*, Oxford University Press, 1973.

139 R. W. Wien, J. D. Morrisett and H. M. McConnell, Spin-Label-Induced Nuclear Relaxation. Distances between Bound Saccharides, Histidine-15, and Tryptophan-123 on Lysozyme in Solution, *Biochemistry*, 1972, **11**, 3707–3716.

140 G. M. Clore, C. Tang and J. Iwahara, Elucidating transient macromolecular interactions using paramagnetic relaxation enhancement, *Curr. Opin. Struct. Biol.*, 2007, **17**, 603–616.

141 G. Esposito, A. Zanobi, E. Giglio, N. V. Pavel and I. D. Campbell, Intermolecular interactions in sodium deoxycholate micelles: An NMR study involving a spin-labeled cholestane, *J. Phys. Chem.*, 1987, **91**, 83–89.

142 T. Madl, W. Bermel and K. Zangger, Use of relaxation enhancements in a paramagnetic environment for the structure determination of proteins using NMR spectroscopy, *angew chem int ed engl*, 2009, **48**, 8259–8262.

143 M. De Rosa, A. Barbiroli, S. Giorgetti, P. P. Mangione, M. Bolognesi and S. Ricagno, Decoding the structural bases of D76N β2-microglobulin high amyloidogenicity through crystallography and asn-scan mutagenesis, *PLoS One*, 2015, **10**, 1–15.

144 D. Ami, S. Ricagno, M. Bolognesi, V. Bellotti, S. M. Doglia and A. Natalello, Structure, stability, and aggregation of β-2 microglobulin mutants: Insights from a Fourier transform infrared study in solution and in the crystalline state, *Biophys. J.*, 2012, **102**, 1676–1684.

145 C. Nitsche and G. Otting, *Prog. Nucl. Magn. Reson. Spectrosc.*, 2017, 98–99, 20–49.

146 F. A. A. Mulder, N. R. Skrynnikov, B. Hon, F. W. Dahlquist and L. E. Kay, Measurement of slow (μs-ms) time scale dynamics in protein side chains by 15N relaxation dispersion NMR spectroscopy: Application to Asn and Gln residues in a cavity mutant of T4 lysozyme, *J. Am. Chem. Soc.*, 2001, **123**, 967–975.

147 M. Tollinger, N. R. Skrynnikov, F. A. A. Mulder, J. D. Forman-Kay and L. E. Kay, Slow dynamics in folded and unfolded states of an SH3 domain, *J. Am. Chem. Soc.*, 2001, **123**, 11341–11352.

148 D. F. Hansen, P. Vallurupalli and L. E. Kay, Using relaxation dispersion NMR spectroscopy to determine structures of excited, invisible protein states, *J. Biomol. NMR*, 2008, **41**, 113–120.

149 P. Neudecker, P. Lundström and L. E. Kay, Relaxation dispersion NMR spectroscopy

as a tool for detailed studies of protein folding, *Biophys. J.*, 2009, **96**, 2045–2054.

150 R. Franco, S. Gil-Caballero, I. Ayala, A. Favier and B. Brutscher, Probing Conformational Exchange Dynamics in a Short-Lived Protein Folding Intermediate by Real-Time Relaxation–Dispersion NMR, *J. Am. Chem. Soc.*, 2017, **139**, 1065–1068.

151 G. Esposito, M. Garvey, V. Alverdi, F. Pettirossi, A. Corazza, F. Fogolari, M. Polano, P. P. Mangione, S. Giorgetti, M. Stoppini, A. Rekas, V. Bellotti, A. J. R. Heck and J. A. Carver, Monitoring the interaction between β2-microglobulin and the molecular chaperone αB-crystallin by NMR and mass spectrometry: αB-crystallin dissociates β2-microglobulin oligomers, *J. Biol. Chem.*, 2013, **288**, 17844–17858.

152 E. L. Kovrigin, J. G. Kempf, M. J. Grey and J. P. Loria, Faithful estimation of dynamics parameters from CPMG relaxation dispersion measurements, *J. Magn. Reson.*, 2006, **180**, 93–104.

153 O. G. Hampe, C. V. Tondo and A. Hasson-Voloch, A biophysical model of lysozyme self-association, *Biophys. J.*, 1982, **40**, 77–82.

154 Y. Hunashal, C. Cantarutti, S. Giorgetti, L. Marchese, H. Molinari, N. Niccolai, F. Fogolari and G. Esposito, Exploring exchange processes in proteins by paramagnetic perturbation of NMR spectra, *Phys. Chem. Chem. Phys.*, 2020, **22**, 6247–6259.

155 A. M. F. Benial, M. K. Dhas and A. Jawahar, Rotational Correlation Time Studies on Nitroxyl Radicals Using 300 MHz ESR Spectrometer in High Viscous Liquid, *Appl. Magn. Reson.*, 2011, **40**, 311–319.

156 G. Esposito, R. Michelutti, G. Verdone, P. Viglino, H. Hernandez, C. V. Robinson, A. Amoresano, F. D. Piaz, M. Monti, P. Pucci, P. Mangione, M. Stoppini, G. Merlini, G. Ferri and V. Bellotti, Removal of the N-terminal hexapeptide from human β2-microglobulin facilitates protein aggregation and fibril formation, *Protein Sci.*, 2000, **9**, 831–845.

157 S. Giorgetti, S. Raimondi, K. Pagano, A. Relini, M. Bucciantini, A. Corazza, F. Fogolari, L. Codutti, M. Salmona, P. Mangione, L. Colombo, A. De Luigi, R. Porcari, A. Gliozzi, M. Stefani, G. Esposito, V. Bellotti and M. Stoppini, Effect of tetracyclines on the dynamics of formation and destructuration of β2-microglobulin amyloid fibrils, *J. Biol. Chem.*, 2011, **286**, 2121–2131.

158 C. Cantarutti, G. Raj, F. Fogolari, S. Giorgetti, A. Corazza, V. Bellotti, P. Naumov and G. Esposito, Interference of citrate-stabilized gold nanoparticles with β2-microglobulin oligomeric association, *Chem. Commun.*, 2018, **54**, 5422–5425.

159 M. P. Williamson, *Prog. Nucl. Magn. Reson. Spectrosc.*, 2013, 73, 1–16.

160 M. Hoshino, H. Katou, Y. Hagihara, K. Hasegawa, H. Naiki and Y. Goto, Mapping the core of the β2-microglobulin amyloid fibril by H/D exchange, *Nat. Struct. Biol.*, 2002, **9**, 332–336.

161 K. F. Morris and C. S. Johnson, Diffusion-Ordered Two-Dimensional Nuclear Magnetic Resonance Spectroscopy, *J. Am. Chem. Soc.*, 1992, **114**, 3139–3141.

162 K. Sakurai, R. Tomiyama, T. Shiraki and Y. Yonezawa, Loosening of side-chain packing associated with perturbations in peripheral dynamics induced by the D76N mutation of β2-microglobulin revealed by pressure-NMR and molecular dynamic simulations, *Biomolecules*, , DOI:10.3390/biom9090491.

163 G. Bodenhausen and D. J. Ruben, Natural abundance nitrogen-15 NMR by enhanced heteronuclear spectroscopy, *Chem. Phys. Lett.*, 1980, **69**, 185–189.

164 A. G. Palmer, J. Cavanagh, R. A. Byrd and M. Rance, Sensitivity improvement in three-dimensional heteronuclear correlation NMR spectroscopy, *J. Magn. Reson.*, 1992, **96**, 416–424.

165 J. Schleucher, M. Schwendinger, M. Sattler, P. Schmidt, O. Schedletzky, S. J. Glaser, O. W. Sørensen and C. Griesinger, A general enhancement scheme in heteronuclear multidimensional NMR employing pulsed field gradients, *J. Biomol. NMR*, 1994, **4**, 301–306.

166 S. Grzesiek and A. Bax, The Importance of Not Saturating H2O in Protein NMR. Application to Sensitivity Enhancement and NOE Measurements, *J. Am. Chem. Soc.*, 1993, **115**, 12593–12594.

167 L. Braunschweiler and R. R. Ernst, Coherence transfer by isotropic mixing: Application to proton correlation spectroscopy, *J. Magn. Reson.*, 1983, **53**, 521–528.

168 M. Piotto, V. Saudek and V. Sklenar, Gradient-tailored excitation for single quantum NMR spectroscopy of aqueous solutions, *J.Biomol.NMR*, 1992, **2**, 661–666.

169 T. L. Hwang and A. J. Shaka, Water Suppression That Works. Excitation Sculpting Using Arbitrary Wave-Forms and Pulsed-Field Gradients, *J. Magn. Reson. - Ser. A*, 1995, **112**, 275–279.

170 D. Marion and K. Wüthrich, Reprint of "Application of phase sensitive two-dimensional correlated spectroscopy (COSY) for measurements of 1H–1H spin–spin coupling constants in proteins", *Biochem. Biophys. Res. Commun.*, 1983, **113**, 967–974.

171 A. D. Bax and G. D. Donald, MLEV-17-based two-dimensional homonuclear magnetization transfer spectroscopy, *J. Magn. Reson.*, 1969, **65**, 355-360.

172 K. T. Dayie and G. Wagner, Relaxation-Rate Measurements for 15N-1H Groups with

Pulsed-Field Gradients and Preservation of Coherence Pathways, *J. Magn. Reson. Ser. A*, 1994, **111**, 121–126.

173 A. G. Palmer, J. Cavanagh, P. E. Wright and M. Rance, Sensitivity improvement in proton-detected two-dimensional heteronuclear correlation NMR spectroscopy, *J. Magn. Reson.*, 1991, **93**, 151–170.

174 A. G. Palmer and H. Koss, in *Methods in Enzymology*, Academic Press Inc., 2019, vol. 615, pp. 177–236.

175 F. Fogolari, A. Corazza, V. Yarra, A. Jalaru, P. Viglino and G. Esposito, Bluues: A program for the analysis of the electrostatic properties of proteins based on generalized Born radii, *BMC Bioinformatics*, 2012, **13**, S18.

176 I. Walsh, G. Minervini, A. Corazza, G. Esposito, S. C. E. Tosatto and F. Fogolari, Bluues server: Electrostatic properties of wild-type and mutated protein structures, *Bioinformatics*, 2012, **28**, 2189–2190.

177 D. Sezer, J. H. Freed and B. Roux, Parametrization, molecular dynamics simulation, and calculation of electron spin resonance spectra of a nitroxide spin label on a polyalanine α-helix, *J. Phys. Chem. B*, 2008, **112**, 5755–5767.

178 J. Gasteiger and M. Marsili, Iterative partial equalization of orbital electronegativity-a rapid access to atomic charges, *Tetrahedron*, 1980, **36**, 3219–3228.

179 L. Kalé, R. Skeel, M. Bhandarkar, R. Brunner, A. Gursoy, N. Krawetz, J. Phillips, A. Shinozaki, K. Varadarajan and K. Schulten, NAMD2: Greater Scalability for Parallel Molecular Dynamics, *J. Comput. Phys.*, 1999, **151**, 283–312.

180 D. Bashford and D. A. Case, Generalized born models of macromolecular solvation effects, *Annu. Rev. Phys. Chem.*, 2000, **51**, 129–152.

181 A. Onufriev, D. Bashford and D. A. Case, Exploring Protein Native States and Large-Scale Conformational Changes with a Modified Generalized Born Model, *Proteins Struct. Funct. Genet.*, 2004, **55**, 383–394.

182 F. Fogolari, A. Corazza, S. Toppo, S. C. E. Tosatto, P. Viglino, F. Ursini and G. Esposito, Studying interactions by molecular dynamics simulations at high concentration, *J. Biomed. Biotechnol.*, 2012, **2012**, 1–9.

183 C. J. Dongmo Foumthuim, A. Corazza, G. Esposito and F. Fogolari, Molecular dynamics simulations of β2-microglobulin interaction with hydrophobic surfaces, *Mol. Biosyst.*, 2017, **13**, 2625–2637.

184 T. Grycuk, Deficiency of the Coulomb-field approximation in the generalized Born model: An improved formula for born radii evaluation, *J. Chem. Phys.*, 2003, **119**, 4817–

4826.

185 M. F. Sanner, A. J. Olson and J. C. Spehner, Reduced surface: An efficient way to compute molecular surfaces, *Biopolymers*, 1996, **38**, 305–320.

186 P. F. Knowles, D. Marsh and H. W. E. Rattle, *Magnetic resonance of biomolecules: An introduction to the theory and practice of NMR and ESR in biological systems*, Wiley, London, 1976.

187 D. Kivelson, Theory of ESR linewidths of free radicals, *J. Chem. Phys.*, 1960, **33**, 1094–1106.

188 S. Kumar, I. Yadav, V. K. Aswal and J. Kohlbrecher, Structure and Interaction of Nanoparticle-Protein Complexes, *Langmuir*, 2018, **34**, 5679–5695.

6. PUBLICATIONS

Full papers related to the thesis

[1] Y. Hunashal, C. Cantarutti, S. Giorgetti, L. Marchese, H. Molinari, N. Niccolai, F. Fogolari, G. Esposito, Exploring exchange processes in proteins by paramagnetic perturbation of NMR spectra, *Physical Chemistry Chemical Physics*, 2020, **22**, 6247-6259

[2] Y. Hunashal, C. Cantarutti, S. Giorgetti, L. Marchese, F. Fogolari, G. Esposito, Insights into a protein-nanoparticle system by paramagnetic perturbation NMR Spectroscopy, *Molecules*, 2020, **25**, 5187

[3] Y. Hunashal, S. Giorgetti, G. Esposito, Self-association study of β2-Microglobuline mutant D76N by paramagnetic perturbation NMR spectroscopy.

In preparation

Other full papers

[1] C. Cantarutti, P. Bertoncin, P. Posocco, Y. Hunashal, S. Giorgetti, V. Bellotti, F. Fogolari, G. Esposito, The interaction of β2-microglobulin with gold nanoparticles: impact of coating, charge and size, *Journal of Materials Chemistry B*, 2018, **6**, 5964-5974

[2] T. Guterman, N. L. Ing, S. Fleischer, P. Rehak, V. Basavalingappa, Y. Hunashal, R. Dongre, S. Raghothama, P. Král, T. Dvir, A. I. Hochbaum, E. Gazit, Electrical Conductivity, Selective Adhesion, and Biocompatibility in Bacteria-Inspired Peptide-Metal Self-Supporting Nanocomposites, *Advanced materials*, 2019, **31**, 1807285

[3] A. Dolle, VB. Nagati, Y. Hunashal, K. Krishnamurthy, AK. Pasupulati, S. Raghothama, K. Hanumae Gowd, Disulfide engineering on temporin-SHf: Stabilizing the bioactive conformation of an ultra-short antimicrobial peptide, *Chemical biology & drug design*, 2019, **94**, 1634-1646

[4] C. Cantarutti, F. Fogolari, Y. Hunashal, V. Ferrara, A. Caragnano, AP. Beltrami, U. Livi, S. Sponga, G. Esposito, Assessing the Effect of Preservation in Heart Transplant Protocol: Cold Ischemia Versus Normothermic Perfusion, *Biomarkers and Applications,* 2019, **3**, 139

[5] S. Y. Khatavi, K. Kantharaju, Y. Hunashal, S. Ragothama, Rice husk SiO_2 (NPs) supported-BO_3H_3: a highly active, solvent-free and recyclable catalyst to dihydropyrimidin-2(1*H*)ones-(thiones) and coumarin-3-carboxylic acid synthesis, *Current Science*, 2019, **117**, 1828

[6] M. Ayyash, B. Abu-Jdayil, P. Itsaranuwat, E. Galiwango, C. Tamiello-Rosa, H. Abdullah, G. Esposito, Y. Hunashal, R. S. Obaid, F. Hamed, Characterization, bioactivities, and rheological properties of exopolysaccharide produced by novel probiotic *Lactobacillus plantarum* C70 isolated from camel milk, *International journal of biological macromolecules*, 2020, **144**, 938-946

[7] M. Ayyash, B. Abu-Jdayil, P. Itsaranuwat, N. Almazrouei, E. Galiwango, G. Esposito, Y. Hunashal, F. Hamed, Z. Najjar, Exopolysaccharide produced by the potential probiotic *Lactococcus garvieae* C47: Structural characteristics, rheological properties, bioactivities and impact on fermented camel milk, *Food Chemistry*, 2020, **333**, 127418.

[8] L. Palanikumar, L. Karpauskaite, S. Hassan, M. Alam, M. Al-Sayegh, I. Chehade, D. Maity, L. Ali, Z. Falls, R. Samudrala, M. Kalmouni, Y. Hunashal, T. Houhou, S. Karapetyan, R. Pasricha, G. Esposito, A. J. Afzal, S. Kumar, A. D. Hamilton, M. Magzoub, Protein mimetic amyloid inhibitor potently abrogates cancer-associated mutant p53 aggregation and restores tumor suppressor function, *bioRxiv*, doi: 10.1101/2020.08.10.243154

[9] T. Prakasam, Y. Hunashal, C. Cantarutti, S. Giorgetti, G. Faravelli, V. Mondani, S. K. Sharma, R. Jagannathan, G. Palmisano, V. Bellotti, F. Fogolari, J-C Olsen, A. Trabolsi, G. Esposito, Metal-organic non-trivial structures inhibit amyloidogenesis.

In preparation

7. ACKNOWLEDGMENT

This research work was carried out at *Department of Biomedical Science and Biotechnology, University of Udine, Italy,* from 1st November 2017 to 15th September 2018 and at *the New York University in Abu Dhabi, Abu Dhabi (UAE),* from October 2018 to October 2020, under the supervision of ***Prof. Dr. Gennaro Esposito***. This thesis would not have been possible without the help of many people. I sincerely acknowledge them.

First, I would like to express my deep gratitude to my Ph.D. supervisor, ***Prof. Dr. Gennaro Esposito.*** His encouragement and guidance were the driving forces of my success. His scientific discussions and motivation were the essential ingredients for my research work. Under his shelter, I enjoyed moving around various places to learn new things and also to present my research work in conferences. I delighted my scientific freedom under his tutelage. His trust and concern on me fueled my interests. He is an inspiring person who influenced me with his dedication, devotion and determination towards research work.

I am grateful to ***Prof. Federico Fogolari*** for the computational work for my experimental results.

I thank NYUAD for providing excellent working ambience, state-of-art NMR facilities and Core Technology platform to carry out my research

I would like to say thanks to my all family members, especially my mother **"*Lakkavva*"** and father **"*Lakkappa*"**, who have been steadfast and supportive. My brother ***"Anand"*** and sisters ***"Savita and Sunita"*** who continued their support and encouragement in achieving this.

The other part of my life is my friends, thanks to ***HariKrishna***, ***Eros***, ***Gerard***, ***Gina***, ***Anita***, ***Ashraf***, ***Himanshi*** who are always with me in Udine and helped me when I needed them. A special thanks to my dear friends ***Ashwini***, ***Dundappa*** and ***Praveen***. Next, I would like to say thanks to my lab mate ***Cristina***, for her company of friendly atmosphere in the lab.

I take this opportunity to thank **former guides from India, *Dr. S. Ragothama* (NMRRC) and *Prof. P. Balaram* (MBU), Indian Institute of Science, Bengaluru,** without them, my scientific career would have been a non-entity.